INVESTIGATION OF BIOMOLECULAR INTERACTIONS AT THE SURFACE OF LIPID BILAYERS USING SECOND HARMONIC GENERATION SPECTROSCOPY, LENS-LESS IMAGING AND CORRELATION SPECTROSCOPY

by

Krystal Lynne Sly

A dissertation submitted to the faculty of
The University of Utah
in partial fulfillment of the requirements for the degree of

Doctor of Philosophy

Department of Chemistry

The University of Utah

December 2014

The University of Utah Graduate School

STATEMENT OF DISSERTATION APPROVAL

The dissertation of **Krystal Lynne Sly**

has been approved by the following supervisory committee members:

John C. Conboy	, Chair	**August 21, 2014** Date Approved
Joel M. Harris	, Member	**August 21, 2014** Date Approved
Jennifer Heemstra	, Member	**August 21, 2014** Date Approved
Marc D. Porter	, Member	**August 21, 2014** Date Approved
Vladimir Hlady	, Member	**August 21, 2014** Date Approved

and by **Cynthia J. Burrows**, Chair/Dean of

the Department/College/School of **Chemistry**

and by David B. Kieda, Dean of The Graduate School.

ABSTRACT

This dissertation focuses on the study of surface biomolecular interactions using second harmonic generation (SHG) spectroscopy, surface SHG imaging (SSHGI), and SH correlation spectroscopy (SHCS). The binding kinetics and energetics of four biotin-bound proteins, avidin, streptavidin, neutrAvidin, and anti-biotin antibody were compared and data revealed significant differences in their apparent binding affinities and nonspecific binding. Specifically, protein-protein interactions were found to play an important role in the apparent binding affinity, making the streptavidin-biotin interaction the most energetically favorable. The details of the binding properties of these frequently employed tether/linker protein-biotin complexes provide valuable information for biosensors, immunoassays, and medical diagnostics.

As most biosensor platforms are designed for high throughput detection, the resolution and planar wave-front of the SSHGI system was thoroughly analyzed. It was demonstrated that the coherent plane wave generated by SHG followed Gaussian beam propagation, enabling SSHGI to image without a lens system at rather long distances. Lens-less imaging simplifies the detection method, increases photon collection efficiency, and increases the detection area. These advantages could potentially make SSHGI a simple, label-free high throughput detection method for surface biomolecular interactions.

The versatility and sensitivity of SHG were further probed by coupling SHG

with correlation spectroscopy, a statistical fluctuation time-dependent method. SHCS was established as a viable and valuable option for the detection of surface binding kinetics for small molecule and protein-ligand interactions at the surface of lipid bilayers. First, the simple binding kinetics of a small molecule, (s)-(+)-1,1'-bi-2-napthol (SBN), incorporating into a lipid bilayer was determined using SHCS and results were statistically similar to those obtained from a traditional binding isotherm. Next, SHCS was used to examine the binding kinetics of a more complex interaction between the multivalent proteins, cholera toxin subunit b (CTb) and peanut agglutinin (PnA), and a GM_1 doped lipid bilayer. SHCS was able to obtain the binding kinetics for these surface biomolecular interactions with more efficiency, less analyte, and less sensitivity to mass transport effects.

Cumulatively, the studies of this dissertation showcase SHG, SSHGI, and SHCS as valuable label-free detection methods with incredible sensitivity for investigation of surface biomolecular interactions.

TABLE OF CONTENTS

LIST OF TABLES

LIST OF FIGURES

LIST OF ABBREVIATIONS

ELISA	Enzyme linked immunosorbent assay
SPR	Surface plasmon resonance
QCM	Quartz crystal microbalance
SHG	Second harmonic generation
PSLB	Planar supported lipid bilayer
SSHGI	Surface second harmonic generation imaging
SBN	(S)-(+)-1,1'-bi-2-naphthol
FCS	Fluorescence correlation spectroscopy
DOPC	1,2-dioleoyl-*sn*-glycero-3-phosphocholine
CTb	Cholera toxin subunit B
PnA	Peanut agglutinin
GM_1	Monosialotetrahexosylganglioside
SHCS	Second harmonic correlation spectroscopy
UV	Ultraviolet
Biotin-cap-DOPE	1,2-dioleoyl-*sn*-glycero-3-phosphoethanolamine-N-(Cap biotinyl)
PBS	Phosphate buffer saline
IR/UV	Infrared/Ultraviolet
SUV	Small unilamellar vesicles

IgG	Immunoglobulin G
PMT	Photon multiplier tube
LOD	Limit of detection
USAF	United States Air Force
Rh-cap-DOPE	1,2-dioleoyl-*sn*-glycero-3-phosphoethanolamine-N-(lissamine rhodamine B sulfonyl)
UVO	Ultraviolet O-zone
CCD	Charged coupled detector
TIRF	Total internal reflection fluorescence
FWHM	Full width at half maximum
CS	Correlation spectroscopy
DLS	Dynamic light scattering
S/N	Signal-to-noise ratio

ACKNOWLEDGEMENTS

I would like to express my sincere appreciation for all those who have offered their support and encouragement throughout my graduate studies at the University of Utah; this dissertation would not have been possible without them.

I would particularly like to express my gratitude for the mentorship of Dr. John Conboy. I sincerely appreciate the patient guidance and support with my research projects. His passion and enthusiasm for science and research was contagious and extremely welcomed, especially at those times when research seemed overwhelming.

I would also like to extend my thanks to the members of my advisory committee, Drs. Harris, Heemstra, Hlady, and Porter, for their valuable insights and critiques of my research.

I am appreciative of all the support, friendship and enlightening conversations I had with the members of the Conboy lab. In particular, I would like to thank Dr. Trang Nguyen, who patiently taught me the necessary tools to do well in lab. I admire her dedication and determination and will always be thankful for her mentorship and friendship. I would also like to thank Story Mok for her assistance with initial troubleshooting of the correlation studies. Her calm personality and laughter were refreshing in the middle of many stressful times. Krystal Brown, my name twin, will always have my gratitude for her endless willingness to proofread, discuss research, and soothe an anxious friend before a presentation.

I would also like to express my deepest appreciation for my family. Specifically, I would like to thank my niece and nephew, who continually remind me not to take life too seriously; after all, everyone can be a princess or a pirate with the right outfit and imagination. I owe a great deal of thanks to Lee, who has been by my side through this journey and has given me encouragement along the way. Lastly, but certainly not least I need to thank my mother; she is my confidant, friend, and personal cheerleader, without whom I could not have survived the rollercoaster ride of graduate school. Mom, I love you more than a million red M&Ms!

CHAPTER 1

INTRODUCTION

Biomolecular interactions play an important role in several bioanalytical fields including chromatography,[1-3] immunoassays,[4,5] biosensors,[6-8] and medical diagnostics.[9,10] For example, protein-biotin complexes are often used as a tether/linker on biosensor platforms,[6] protein-carbohydrate interactions are utilized for the differentiation of cells via the glycoprotein/glycolipid expression,[11] and antibody-antigen pairs are employed for detection of viruses, bacteria and drugs.[7] The high affinity and high specificity of these protein-ligand pairs increase the sensitivity and efficiency of these bioanalytical techniques such that trace amounts of contaminants, drugs, antibodies, and biomarkers are detectable.[4-8,12,13] The significant role of protein-ligand pairs makes it extremely important to examine their binding properties at a surface. A more detailed understanding of these crucial biomolecular interactions will provide valuable insights for better biosensor development, drug design, and medical diagnosis.

A variety of analytical techniques have been employed for investigating protein-ligand and other biomolecular interactions at a surface. Some of the more common techniques utilized include fluorescence,[14-16] enzyme linked immunosorbent assays (ELISA),[13,17] surface plasmon resonance (SPR),[7,18,19] quartz crystal microbalance (QCM),[20,21] and confocal Raman Microscopy.[22,23] Fluorescence has particularly shown

incredible sensitivity in detecting biomolecular interactions at surfaces with the ability to detect fg/cm^2 quantities and even, more remarkably, single-molecule interactions.[14,16] Other fluorescence studies have examined these biomolecular interactions at the surface of planar supported lipid bilayers (PSLBs) and liposomes,[24,25] which mimic the fluidity found in cellular membranes and allow for precise control of the ligand density.[26] Although the high sensitivity, versatility, and ability to use biologically relevant platforms makes fluorescence an attractive and useful technique for investigating surface biomolecular interactions, its major obstacle lies in the fact that an external fluorophore label is often required. The time consuming and complex process of chemically attaching a label is often problematic, leading to changes in charge, hydrophobicity and altered binding energetics.[27] Additionally, photobleaching of the attached fluorophore can complicate the analysis of biomolecular binding kinetics.[28]

ELISA is probably even more widely utilized for detection of biomolecular interactions than fluorescence, especially for the analysis of biosensors and immunoassays where high-throughput detection is required.[29] ELISA typically involves the immobilization of an antigen and at least one antibody specific for that antigen. The specific antibody can either be covalently linked to a signal inducing enzyme or itself be detected by an enzyme-linked secondary antibody. The many commercially available and relatively affordable ELISA kits make detection of these antibody-antigen interactions relatively straightforward and simple. Although ELISA was the first widely used medical screening method to detect viruses and proteins in blood serum and urine samples,[13,17,29] problems can arise from passive adsorption and competitive binding of contaminants.[30]

Several label-free techniques capable of detecting surface biomolecular

interactions have been shown to circumvent some of the difficulties associated with indirect detection through an external label. SPR is one of the most widely used label-free techniques for detecting surface biomolecular interactions. SPR is an optical technique where the detected changes in the refractive index are related to the change of adsorbed mass on the sensor surface, which allows real-time detection of surface biomolecular interactions.[18,31] Although SPR has proven to be a valuable biosensing detection method capable of detecting protein-ligand interactions, protein-DNA interactions, and protein conformational changes,[18,19,32,33] it requires a metal surface that must be chemically modified in order to attached biomolecules. The chemical activation of the sensor surface is often nonspecific and can lead to multiple coupling sites on the immobilized biomolecule, resulting in some partially or fully blocked binding sites that may cause complex binding energetics.[31]

In the label-free detection method, QCM, sensor surfaces are not limited to metal and can be pure quartz, alleviating some of the obstacles seen with SPR. QCM detects changes in mass by measuring the decrease in the resonance frequency of a quartz crystal as molecules are adsorbed.[21] Several modifications to the QCM technique, such as dissipation and electrodeless QCM,[21] have allowed detection of a variety of biomolecular interactions, including aggregations of peptides, protein-ligand interactions, and antibody binding to an immunosensor.[21] Although both SPR and QCM do not require a label while still typically having a limit of detection on the order of ng/cm^2 to pg/cm^2,[19-21,34] both techniques lack the chemical specificity of spectroscopic methods, which may limit their application.

Confocal Raman microscopy is a spectroscopic and label-free technique that is

capable of providing detailed chemically specific information. Although confocal Raman microscopy is more prevalently used in examining the composition of cells,[35] viruses[36] and bacteria[37] rather than the binding of these biomolecules, it has been utilized to detect surface biomolecular interactions[22,23,38] including protein-ligand interactions and drug-membrane interactions.[21,22,34] However, the inherently weak scattering of Raman often requires signal amplification by using a metal surface or an increase in acquisition time.[23]

Another spectroscopic and label-free alternative for detecting surface biomolecular interactions is second harmonic generation (SHG). SHG has been widely used as a valuable surface science technique ever since Bloembergen and coworkers demonstrated that the lack of inversion symmetry found at interfaces produced optical SHG.[39] This incredible surface specificity makes SHG capable of detecting both large proteins and small drug or antigen molecules, making it particularly well-suited for detecting a variety of biomolecular interactions at a surface. SHG has monitored the conformational changes of biomolecules tethered to a surface,[40] protein adsorption at liquid/solid interfaces,[41,42] and peptide and small molecule interactions with a PSLB.[43] In these studies, SHG was found to have a limit of detection on the order of pg/cm^2 to fg/cm^2.[44,45] The combined surface specificity, high sensitivity, chemical specificity and label-free nature of SHG make it a very attractive technique to examine surface biomolecular interactions.

This dissertation details the study of several biomolecular interactions at the surface of PSLBs examined using SHG. The general principles of the SHG process under a counter-propagating geometry are presented in Chapter 2 with an emphasis on the properties that make SHG particularly suitable for investigating surface biomolecular

interactions. Specifically, the surface specificity from symmetry constraints and high sensitivity from resonant enhancement are detailed. The ability of SHG to detect surface biomolecular interactions is applied in Chapter 3 to the investigation of the binding properties of four biotin-bound protein pairs at the surface of a biotinylated PSLB. The proteins, avidin, streptavidin, neutrAvidin, and anti-biotin antibody are all commonly used in bioanalytical applications as tether/linkers designed to capture the biomolecule of interest.[4,6,9,46] Although avidin and its two analogs, streptavidin and neutrAvidin, are often used interchangeably on the platforms of biosensors, little work exists that compares their relative binding affinities and properties. Investigation of these biotin-protein interactions under identical experimental conditions allows a more detailed and informative comparison of the relative binding properties to be made. The equilibrium binding affinities of all three proteins were extracted from a traditional binding isotherm measured by SHG and used to determine the relative energetics for each protein binding to a biotinylated lipid bilayer. Other properties known to affect the energetics of protein-ligand binding, such as interactions between the protein molecules and nonspecific binding of the protein, were also investigated in Chapter 3. From the shape of the binding isotherm at low protein concentrations and use of a cooperativity binding model developed by Zhao and coworkers, the effective protein-protein interactions and their energetic contributions to the overall binding affinity were determined.[15] The findings presented in Chapter 3 not only showcase SHG as a valuable surface specific, label-free, and highly sensitive technique for the detection of surface protein-ligand interactions, but also provide important new insights into these biotin bound protein complexes commonly used in several bioanalytical applications.

As most bioassays and biosensors require high throughput detection, SHG imaging was recently used to examine drug-membrane interactions at the surface of a multicomponent lipid bilayer array;[47] however, the SHG imaging properties have not yet been fully explored. Chapter 4 is dedicated to thoroughly examining the properties of surface second harmonic generation imaging (SSHGI). Specifically, the implications of the coherent plane-wave nature of SHG are investigated. Theoretically, if a planar wave front exists, there is no need for a lens to be used in the imaging system and the beam should propagate according to Gaussian beam propagation theory.[48] Since Gaussian beam propagation theory depends on the size of the imaged object,[48] an SHG active molecule, (*s*)-(+)-1,1'-bi-2-naphthol (SBN), incorporated into a lipid bilayer was imaged for various image sizes at several object-detector distances without the aid of a lens system. Using Gaussian beam propagation theory the resolution and confocal length of the counter-propagating lens-less SSHGI system was determined. Removing the lens has the potential to simplify the detection method, raise photon collection efficiency, and expand the field-of-view. These advantages would allow greater throughput and could make lens-less SSHGI a potentially valuable detection method for biosensors and medical diagnostics. Additionally, the analysis of the coherence length and propagation of the emitted SH output provides important details of the parameters and properties of SHG. More importantly, the analysis of the coherence of SHG was critical for the development of coherent second harmonic correlation spectroscopy (SHCS), a statistical fluctuation time dependent method, whose general principles are developed in Chapter 5.

Correlation spectroscopy has been used as an analysis method since the early 1950s when Van Hove first utilized the spontaneous fluctuations seen in coherent neutron

scattering to determine the dynamic properties of the sample.[49] Photon correlation spectroscopy or dynamic light scattering has been around for nearly as long,[50] but today the most popular correlation spectroscopy is fluorescence correlation spectroscopy (FCS).[51,52] Since its inception in 1972, FCS has been utilized for investigating translational, diffusional and rotational coefficients,[53-55] as well as surface binding dynamics[51,56] and conformational dynamics of biomolecules.[57] Although FCS still remains at the forefront of correlation spectroscopy, other methods, such as Raman correlation spectroscopy and coherent x-ray correlation spectroscopy,[58,59] have recently been used to study dynamic surface processes. SHCS was demonstrated in the 1990s by Zhao and coworkers for a limited investigation of diffusion and orientational fluctuations seen in lipid bilayers;[60,61] however, it was never implemented as a method to study surface biomolecular interactions.

In Chapter 6 the first implementation of SHCS in measuring surface binding kinetics is demonstrated in the investigation of SBN intercalating into a lipid bilayer. The local fluctuations of the measured SH signal were used to extract the binding kinetics of SBN intercalation into a 1,2-dioleoyl-*sn*-glycero-3-phosphocoline (DOPC) bilayer. The kinetic rates as well as the calculated equilibrium binding constant obtained from the correlation studies are compared with those obtained from a conventional binding isotherm in order to validate the findings obtained through SHCS. The primary advantage of using SHCS is that both the absorption and desorption rate can be determined in the same experiment with only data collection of a single concentration of analyte. The results of these studies demonstrate that SHCS can be used to provide accurate kinetic and thermodynamic binding data in lieu of conventional isotherm studies, especially

where time and analyte are scarce.

As an extension of this simple binding system, SHCS was used to investigate more complex multivalent protein-ligand interactions in Chapter 7. Multivalent proteins have been extremely useful for detection and separation of biomolecules on biosensors and immunoassays.[62-64] Their high affinity and specificity are some of the properties that make these multivalent proteins valuable bioanalytical tools.[65,66] In Chapter 7, the binding kinetics of two commonly used multivalent proteins, cholera toxin subunit b (CTb) and peanut agglutinin (PnA), to a GM_1 doped DOPC lipid bilayer were investigated using SHCS. The adsorption and desorption rates, as well as the binding affinity, for 3 bulk protein concentrations were determined using SHCS and compared to those obtained using a typical binding isotherm. As opposed to the traditional binding isotherm, SHCS was able to examine the binding kinetics as a function of protein concentration for these multivalent protein-ligand complexes. The findings of this study provide additional insight into the complex interactions between multivalent proteins and their ligands, as well as emphasize the advantages of SHCS for examining these complex yet technologically important protein-ligand complexes.

Collectively, the studies presented in this dissertation demonstrate that SHG is a valuable label-free detection method for biomolecular interactions at a surface and that SHCS is an extremely useful fluctuation analysis method that increases the versatility of SHG spectroscopy. The findings from these studies provide indispensable insights for important bioanalytical applications including biosensor development, drug design and medical diagnostic devices.

1.1 References

(1) Silva, M. S.; Graca, V. C.; Reis, L. V.; Santos, P. F.; Almeida, P.; Queiroz, J. A.; Sousa, F. *Biomed. Chromatogr.* **2013**, *27*, 1671-1679.

(2) Mallik, R.; Hage, D. S. *J. Sep. Sci.* **2006**, *29*, 1686-1704.

(3) Schiel, J. E.; Mallik, R.; Soman, S.; Joseph, K. S.; Hage, D. S. *J. Sep. Sci.* **2006**, *29*, 719-737.

(4) Zhavnerko, G. K.; Yi, S. J.; Chung, S. H.; Yuk, J. S.; Ha, K. S. *NATO Sci. Ser., II* **2004**, *152*, 95-108.

(5) Barton, A. C.; Davis, F.; Higson, S. P. J. *Anal. Chem.* **2008**, *80*, 9411-9416.

(6) Ladd, J.; Boozer, C.; Yu, Q.; Chen, S.; Homola, J.; Jiang, S. *Langmuir* **2004**, *20*, 8090-8095.

(7) Hall, W. P.; Ngatia, S. N.; Van Duyne, R. P. *J. Phys. Chem. C* **2011**, *115*, 1410-1414.

(8) Hunt, H. K.; Dahmen, J. L.; Soteropulos, C. E. *Proc. SPIE* **2014**, *8960*, 89600O/89601-89600O/89610.

(9) Cooper, M. A. *Nat. Rev. Drug Discovery* **2002**, *1*, 515-528.

(10) Fard, S. T.; Grist, S. M.; Donzella, V.; Schmidt, S. A.; Flueckiger, J.; Wang, X.; Shi, W.; Millspaugh, A.; Webb, M.; Ratner, D. M.; Cheung, K. C.; Chrostowski, L. *Proc. SPIE* **2013**, *8629*, 862909/862901-862909/862914.

(11) Makita, A.; Tsuiki, S.; Fujii, S.; Warren, L.;*Membrane Alterations in Cancer;* Japan Scientific Societies Press, 1983.

(12) Fromell, K.; Forsberg, P.; Karlsson, M.; Larsson, K.; Nikolajeff, F.; Baltzer, L. *Anal. Bioanal. Chem.* **2012**, *404*, 1643-1651.

(13) Sokolov, O.; Kost, N.; Andreeva, O.; Korneeva, E.; Meshavkin, V.; Tarakanova, Y.; Dadayan, A.; Zolotarev, Y.; Grachev, S.; Mikheeva, I.; Varlamov, O.; Zozulya, A. *Peptides* **2014**, *56*, 68-71.

(14) Wayment, J. R.; Harris, J. M. *Anal. Chem.* **2009**, *81*, 336-342.

(15) Zhao, S.; Walker, D. S.; Reichert, W. M. *Langmuir* **1993**, *9*, 3166-3173.

(16) Shi, J.; Yang, T.; Kataoka, S.; Zhang, Y.; Diaz, A. J.; Cremer, P. S. *J. Am. Chem. Soc.* **2007**, *129*, 5954-5961.

(17) Nagamine, T.; Nakajima, K. *Curr. Pharm. Biotechnol.* **2013**, *14*, 427-431.

(18) Kodoyianni, V. *BioTechniques* **2010**, *50*, 32-40.

(19) Prabowo, B. A.; Chang, Y.-F.; Lee, Y.-Y.; Su, L.-C.; Yu, C.-J.; Lin, Y.-H.; Chou, C.; Chiu, N.-F.; Lai, H.-C.; Liu, K.-C. *Sens. Actuators, B* **2014**, *198*, 424-430.

(20) Janshoff, A.; Steinem, C.; Sieber, M.; Galla, H.-H. *Eur. Biophys. J.* **1996**, *25*, 105-113.

(21) Ogi, H. *Proc. Jpn. Acad., Ser. B* **2013**, *89*, 401-417.

(22) Fox, C. B.; Harris, J. M. *J. Raman Spectrosc.* **2010**, *41*, 498-507.

(23) Sandras, F.; Pezolet, M.; Marion, D.; Grauby-Heywang, C. *Langmuir* **2009**, *25*, 8181-8186.

(24) Schuette, O. M.; Ries, A.; Orth, A.; Patalag, L. J.; Roemer, W.; Steinem, C.; Werz, D. B. *Chem. Sci.* **2014**, *5*, 3104-3114.

(25) Machan, R.; Jurkiewicz, P.; Olzynska, A.; Olsinova, M.; Cebecauer, M.; Marquette, A.; Bechinger, B.; Hof, M. *Langmuir* **2014**, *30*, 6171-6179.

(26) Sandrin, L.; Coche-Guerente, L.; Bernstein, A.; Basit, H.; Labbe, P.; Dumy, P.; Boturyn, D. *Org. Biomol. Chem.* **2010**, *8*, 1531-1534.

(27) Lakowicz, J. R. *Principles of Fluorescence Spectroscopy*; 3rd. ed.; Spinger: New York, 2006.

(28) Weingart, C. L.; Broitman-Maduro, G.; Dean, G.; Newman, S.; Peppler, M.; Weiss, A. A. *Infect. Immun.* **1999**, *67*, 4264-4267.

(29) Jin, H.; Zangar, R. C. *Cancer Biomarkers* **2010**, *6*, 281-290.

(30) Kenny, G. E.; Dunsmoor, C. L. *J. Clin. Microbiol.* **1983**, *17*, 655-665.

(31) Gerrard, J. A.;*Protein Nanotechnology: Protocols, Instrumentation, and Applications*; 2nd ed.; Humana Press: New York, 2013.

(32) Homola, J.; Yee, S. S.; Gauglitz, G. *Sens. Actuators, B* **1999**, *54*, 3-15.

(33) Kuziemko, G. M.; Stroh, M.; Stevens, R. C. *Biochemistry* **1996**, *35*, 6375-6384.

(34) Li, G.; Li, X.; Yang, M.; Chen, M.-M.; Chen, L.-C.; Xiong, X.-L. *Sensors* **2013**, *13*, 12794-12803.

(35) Puppels, G. J.; de Mul, F. F.; Otto, C.; Greve, J.; Robert-Nicoud, M.; Arndt-Jovin, D. J.; Jovin, T. M. *Nature* **1990**, *347*, 301-303.

(36) Moor, K.; Ohtani, K.; Myrzakozha, D.; Zhanserkenova, O.; Andriana, B. B.; Sato, H. *Proc. SPIE* **2014**, *8939*, 893902/893901-893902/893907.

(37) Biju, V.; Pan, D.; Gorby Yuri, A.; Fredrickson, J.; McLean, J.; Saffarini, D.; Lu, H. P. *Langmuir* **2007**, *23*, 1333-1338.

(38) Salehi, H.; Derely, L.; Vegh, A.-G.; Durand, J.-C.; Gergely, C.; Larroque, C.; Fauroux, M.-A.; Cuisinier, F. J. G. *Appl. Phys. Lett.* **2013**, *102*.

(39) Bloembergen, N.; Chang, R. K.; Jha, S. S.; Lee, C. H. *Phys. Rev.* **1968**, *174*, 813-822.

(40) Salafsky, J. S. *Chem. Phys. Lett.* **2003**, *381*, 705-709.

(41) Hicks, J. M.; Petralli-Mallow, T. *Appl. Phys. B Lasers Opt.* **1999**, *68*, 589-593.

(42) Salafsky, J. S.; Eisenthal, K. B. *J. Phys. Chem. B* **2000**, *104*, 7752-7755.

(43) Kriech, M. A.; Conboy, J. C. *J. Am. Chem. Soc.* **2003**, *125*, 1148-1149.

(44) Nguyen, T. T.; Sly, K. L.; Conboy, J. C. *Anal. Chem.* **2012**, *84*, 201-208.

(45) Sly, K. L.; Mok, S.-W.; Conboy, J. C. *Anal. Chem.* **2013**, *85*, 8429-8435.

(46) Grunwell, J. R.; Glass, J. L.; Lacoste, T. D.; Deniz, A. A.; Chemla, D. S.; Schultz, P. G. *J. Am. Chem. Soc.* **2001**, *123*, 4295-4303.

(47) Nguyen, T. T.; Conboy, J. C. *Anal. Chem.* **2011**, *83*, 5979-5988.

(48) Goldsmith, P. F. *Quasioptical Systems: Gaussian Beam Quasioptical Propagation and Applications*; IEEE Press, 1998.

(49) van Hove, L. *Phys. Rev.* **1954**, *95*, 249-262.

(50) Pecora, R. *J. Chem. Phys.* **1964**, *40*, 1604-1614.

(51) Magde, D.; Elson, E.; Webb, W. W. *Phys. Rev. Lett.* **1972**, *29*, 705-708.

(52) R.Lakowicz, J.;*Topics in Fluorescence Spectroscopy*; Plenum Press, 1991; Vol. 1.

(53) Magde, D.; Elson, E. L.; Webb, W. W. *Biopolymers* **1974**, *13*, 29-61.

(54) Koppel, D. E.; Axelrod, D.; Schlessinger, J.; Elson, E. L.; Webb, W. W. *Biophys.*

J. **1976**, *16*, 1315-1329.

(55) Hansen, R. L.; Harris, J. M. *Anal. Chem.* **1998**, *70*, 2565-2575.

(56) Hansen, R. L.; Harris, J. M. *Anal. Chem.* **1998**, *70*, 4247-4256.

(57) Chattopadhyay, K.; Saffarian, S.; Elson, E. L.; Frieden, C. *Biophys. J.* **2005**, *88*, 1413-1422.

(58) Dierker, S. B.; Pindak, R.; Fleming, R. M.; Robinson, I. K.; Berman, L. *Phys. Rev. Lett.* **1995**, *75*, 449-452.

(59) Sikharulidze, I.; Dolbnya, I. P.; Madsen, A.; de Jeu, W. H. *Opt. Commun.* **2005**, *247*, 111-124.

(60) Zhao, X.; Goh, M. C.; Subrahmanyan, S.; Eisenthal, K. B. *J. Phys. Chem.* **1990**, *94*, 3370-3373.

(61) Zhao, X.; Eisenthal, K. B. *J. Chem. Phys.* **1995**, *102*, 5818-5826.

(62) Arosio, D.; Vrasidas, I.; Valentini, P.; Liskamp, R. M. J.; Pieters, R. J.; Bernardi, A. *Org. Biomol. Chem.* **2004**, *2*, 2113-2124.

(63) Moran-Mirabal, J. M.; Edel, J. B.; Meyer, G. D.; Throckmorton, D.; Singh, A. K.; Craighead, H. G. *Biophys. J.* **2005**, *89*, 296-305.

(64) Wittenberg, N. J.; Johnson, T. W.; Oh, S.-H. *Anal. Chem.* **2012**, *84*, 8207-8213.

(65) Emerson, D.; Juliano, R. L. *J. Cell. Physiol.* **1982**, *111*, 171-176.

(66) Molin, K.; Fredman, P.; Svennerholm, L. *FEBS Lett.* **1986**, *205*, 51-55.

CHAPTER 2

GENERAL PRINCIPLES OF SECOND HARMONIC GENERATION

2.1 Introduction

Second harmonic generation (SHG) was first demonstrated from a crystalline quartz sample in 1961 by Franken and coworkers.[1] Taking advantage of Franken and coworkers' observation that SHG is only produced in noncentrosymmetric media, Bloembergen and coworkers demonstrated that a similar lack of an inversion center found at interfaces can also produce optical SHG.[2] Bloembergen's discovery of the ability of SHG to probe chemical and physical properties of interfaces led to the wide use of SHG as a valuable surface science technique spanning several disciplines, such as physics, chemistry, biology, and materials science.[3-7] In particular, surface SHG has been used to examine various properties of interfaces including the surface structures of metals,[5] the structural symmetry of a semiconductor's surface layer,[4] the effective surface charge density on an electrode due to adsorption of ions,[6] the conformational changes of biomolecules tethered to a surface,[7] and protein adsorption at liquid/solid interfaces.[8,9] As the theory of SHG has already been described in detail elsewhere,[1-3,10-12] this chapter will discuss the general principles of SHG that make it an elegant label-free and surface specific technique for examining interactions of biomolecules at a surface.

2.2 General Principles of SHG

SHG is a second order nonlinear optical process where two input photons of the same frequency interact spatially and temporally to produce a third photon at twice the frequency. The symmetry constraints of second order nonlinear optical processes make SHG forbidden in centrosymmetric media where there is an inversion center, such as bulk solutions of molecules. However, at interfaces where there is a necessary break in inversion symmetry SHG is allowed. This particular property, along with resonant enhancement, affords SHG the ability to detect a submonolayer of molecules interacting at an interface without any contribution from the bulk solution. With these inherent properties, SHG is a highly sensitive surface specific technique that is well-suited for investigating a variety of biomolecules at a surface.

2.3 Symmetry Constraints and Surface Specificity

As a second order nonlinear optical process, SHG is only allowed when there is a break in inversion symmetry. For example, at a surface there is no inversion center, allowing an SHG response to be produced. When the two input photons at frequency ω are spatially and temporally overlapped the output SH response at 2ω is governed by an induced nonlinear polarization given by,

$$P_i^{(2)}(2\omega) = \chi_{ijk}^{(2)} E_j E_k \tag{2.1}$$

where χ_{ijk} is the second order susceptibility tensor which characterizes the interactions of the two incoming electric fields, E_j and E_k, with the molecules at the surface. The subscripts of χ_{ijk} indicate the output, i, and input fields, j and k. Since the output and input fields can be designated by any of the Cartesian coordinates, x, y, z, there are 27 possible

contributing elements to the susceptibility tensor. However, since the input fields have the same frequency and are interchangeable the number of possible tensor elements is reduced to 18 terms. As such the induced polarization for each of the Cartesian coordinate directions can be expressed as follows:

$$\begin{bmatrix} P_x(2\omega) \\ P_y(2\omega) \\ P_z(2\omega) \end{bmatrix} = \begin{bmatrix} \chi_{xxx} & \chi_{xyy} & \chi_{xzz} & \chi_{xxy} & \chi_{xxz} & \chi_{xyz} \\ \chi_{yxx} & \chi_{yyy} & \chi_{yzz} & \chi_{yxy} & \chi_{yxz} & \chi_{yyz} \\ \chi_{zxx} & \chi_{zyy} & \chi_{zzz} & \chi_{zxy} & \chi_{zxz} & \chi_{zyz} \end{bmatrix} \cdot \begin{bmatrix} E_x(\omega) & E_x(\omega) \\ E_y(\omega) & E_y(\omega) \\ E_z(\omega) & E_z(\omega) \\ 2E_x(\omega) & E_y(\omega) \\ 2E_x(\omega) & E_z(\omega) \\ 2E_y(\omega) & E_z(\omega) \end{bmatrix} \quad (2.2)$$

Although there are 18 possible contributing tensor elements for SHG, the symmetry dependence of the susceptibility tensor will lead to many zero or vanishing elements. For example, in centrosymmetic media where there is an inversion center and all directions are symmetric and equal, the resulting value of χ_{ijk} in opposing directions has to also be equal,[3,13]

$$\chi_{ijk}^{(2)} = \chi_{-i-j-k}^{(2)} \quad (2.3)$$

Furthermore, since χ_{ijk} is a third rank tensor describing the interactions of three fields, two input and an output field, changing the direction of all three fields will necessarily change the sign of the corresponding susceptibility tensor,[3,13]

$$\chi_{ijk}^{(2)} = -\chi_{-i-j-k}^{(2)} \quad (2.4)$$

For both of these requirements shown in Equations 2.3 and 2.4 to be satisfied, χ_{ijk} will have to be zero. This means that in media where there is an inversion center, such as a bulk solution, there will be no contributing elements to produce an SHG response.

On the other hand, at surfaces where the inversion symmetry is broken, there are some nonzero or nonvanishing tensor elements that lead to an SHG response. For

example, the surfaces used in the studies described in the following chapters have $C_{\infty v}$ symmetry. At a surface with a C_∞ rotation axis $z \neq -z$, but $x \equiv -x$ and $y \equiv -y$, which means that the surface is symmetric about the surface normal. Under these symmetry conditions Equation 2.4 must still be satisfied, but Equation 2.3 is only applicable when there is a change in either the *x* or *y* direction.[3,13] As such, there are three nonvanishing tensor elements that contribute to the observed SH response seen at a surface with $C_{\infty v}$ symmetry, χ_{zzz}, χ_{zii}, and χ_{izi} ($i = x$ or y).[13] These unique symmetry constraints of χ_{ijk} make SHG a highly surface specific technique as all tensor elements vanish in bulk solution where there is an inversion center.

2.4 Counter Propagating SHG Induced Nonlinear Polarization

In the previous section it was shown that at a surface there are three non-vanishing $\chi^{(2)}$ tensor elements contributing to the induced polarization of the SH response. The induced polarization can now be written in terms of the Cartesian components *x*, *y* and *z* for these nonvanishing $\chi^{(2)}$ elements as follows:[12]

$$P_x(2\omega) = \chi_{xzx}E_{x1}(\omega)E_{z2}(\omega) + \chi_{xzx}E_{z1}(\omega)E_{x2}(\omega), \quad (2.5a)$$

$$P_y(2\omega) = \chi_{yzy}E_{y1}(\omega)E_{z2}(\omega) + \chi_{yzy}E_{z1}(\omega)E_{y2}(\omega), \quad (2.5b)$$

$$P_z(2\omega) = \chi_{zxx}E_{x1}(\omega)E_{z2}(\omega) + \chi_{zyy}E_{y1}(\omega)E_{y2}(\omega) + \chi_{zzz}E_{z1}(\omega)E_{z2}(\omega), \quad (2.5c)$$

where E_x, E_y, and E_z are applied electric field vectors in the Cartesian coordinate system for the two input photons. Since the two input photons have the same frequency in SHG, the above susceptibility tensor elements χ_{xzx} and χ_{yzy}, and χ_{zxx} and χ_{zyy} are degenerate.

In the following chapters, a counter-propagating SHG geometry is employed where not all of the polarization components contribute to the SH response. A schematic

of the counter propagating setup used is shown in Figure 2.1. Counter-propagating SHG, as developed by Kriech and Conboy,[12] consists of the two input photons approaching the sample from opposing directions to produce the SH output along the surface normal in the *z* direction. Since the two input photons are equal in magnitude, but opposite in the *x* direction, the *x* component of the electric field vectors cancel each other out, $E_{x1}(\omega) = -E_{x2}(\omega)$, and the induced polarization in the *x* direction, $P_x(2\omega)$, becomes zero.[12] Furthermore, the induced polarization in the *z* direction, $P_z(2\omega)$, vanishes as this is the propagation axis of the SH output. As a result, the only nonlinear polarization component that contributes to the SH response in counter-propagating SHG is the *y* component, $P_y(2\omega)$. The remaining nonlinear polarization component (Eq. 2.5b) can be rewritten in terms of the interfacial coordinate system by using the following transformations for the electric field vectors:

$$E_y(\omega) = Ef_y \sin(\gamma) \tag{2.6a}$$

$$E_z(\omega) = Ef_z \sin(\theta)\cos(\gamma). \tag{2.6b}$$

where *E* is the magnitude of the electric field and is equal to the square-root of the intensity of the input beam, *I*. f_y and f_z are the transmitted linear Fresnel coefficients in the *y* and *z* directions of the transmitted electric fields, respectively. θ is the incident angle with respect to the surface normal and γ is the polarization angle with respect to the plane of incidence defined as the *xz* plane. After substituting Equations 2.6a-b into Equation 2.5b, the *y* component of the induced nonlinear polarization can be written as,

$$P_y(2\omega) = 2I sin\theta sin\gamma cos\gamma f_y f_z \chi_{yzy}. \tag{2.7}$$

Although the above equation is the only contributing nonlinear polarization component in counter-propagating SHG, it is still not complete. As part of the counter-

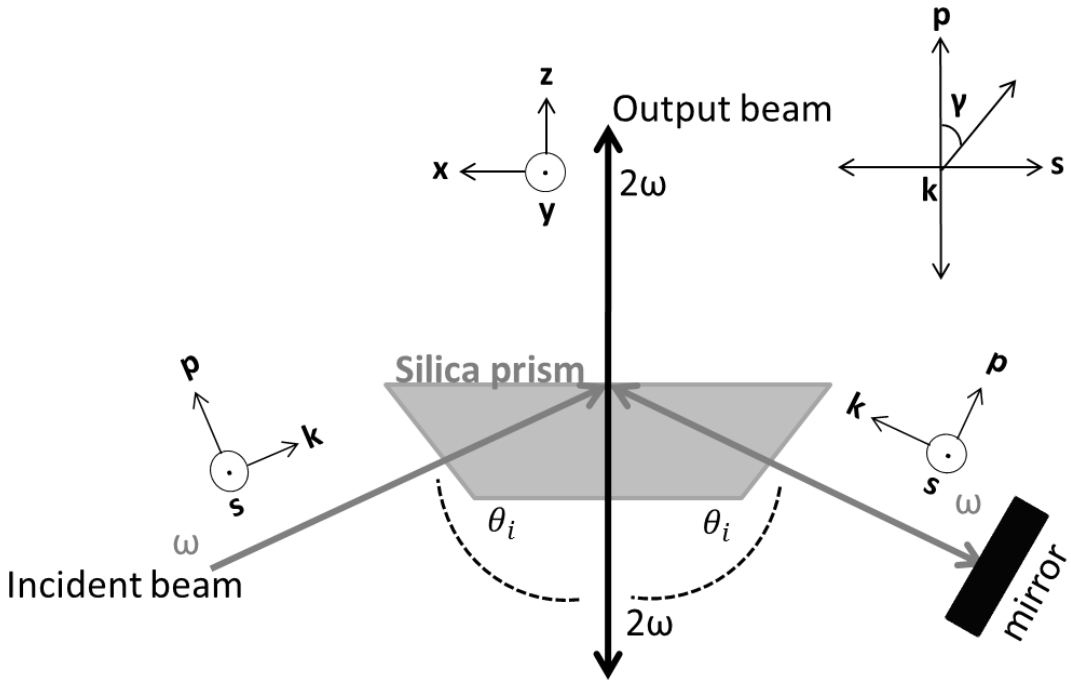

Figure 2.1. Schematic of counter-propagating SHG where two incident beams (dark gray) approach the sample from opposing directions such that the SHG output beam (black) is produced normal to the surface.

propagating geometry, the incident beam, after reaching the sample surface, is reflected back on itself by placing a mirror in its path. As such, the difference between the amount of *s* (perpendicular) and *p* (parallel) polarized light that is reflected back as the second incident beam needs to be taken into account. This correction is calculated by taking the difference in the linear Fresnel coefficients for *s* and *p* polarized inputs upon reflection (f_s^r and f_p^r), which are expressed as follows:[12]

$$f_s^r = \frac{cos\theta_I - \sqrt{\left({}^{n_T}/_{n_R}\right)^2 - sin^2\theta_I}}{cos\theta_I + \sqrt{\left({}^{n_T}/_{n_R}\right)^2 - sin^2\theta_I}}, \tag{2.8a}$$

$$f_p^r = \frac{-\left({}^{n_T}/_{n_R}\right)^2 cos\theta_I + \sqrt{\left({}^{n_T}/_{n_R}\right)^2 - sin^2\theta_I}}{\left({}^{n_T}/_{n_R}\right)^2 cos\theta_I + \sqrt{\left({}^{n_T}/_{n_R}\right)^2 - sin^2\theta_I}}. \tag{2.8b}$$

The induced nonlinear polarization for counter-propagating SHG, $P_y^{ct}(2\omega)$, can now be written as,[12]

$$P_y^{ct}(2\omega) = 2Isin\theta sin\gamma cos\gamma f_y f_z \chi_{yzy} K, \tag{2.9}$$

where

$$K = f_s^r - f_p^r. \tag{2.10}$$

2.5 Counter-Propagating SH Intensity

As mentioned in the previous section, counter-propagating SHG has only one nonzero induced polarization component propagating in the *y* direction along the surface normal or exactly perpendicular to the plane of incidence. Since the SH output is produced normal to the surface in counter-propagating SHG, there are no *s* and *p* polarized SH intensities produced and the SH output intensity can be described in the laboratory frame by,

$$I_y(2\omega) = \left|\tilde{f} P_y^{ct}(2\omega)\right|^2, \tag{2.11}$$

where $\tilde{f}$ is the nonlinear Fresnel coefficient, which describes the fraction of the SH output that is reflected or transmitted in the *y* direction. The transmitted and reflected nonlinear Fresnel coefficients ($\tilde{f}^T$ and $\tilde{f}^R$) in the *y* direction can be expressed as,[10,11]

$$\tilde{f}_y^T = \tilde{f}_y^R = \frac{8\pi d\omega sin\theta_T^{2\omega}}{cn_R^{2\omega} sin(\theta_R^{2\omega}+\theta_T^{2\omega})}, \tag{2.12}$$

where *d* is the thickness of the nonlinear medium, *c* is the speed of light, $n_R^{2\omega}$ is the index of refraction of reflected media in the SH beam, and $\theta_R^{2\omega}$ and $\theta_T^{2\omega}$ are the reflected and transmitted angles of the SH output beam, respectively. In the counter-propagating geometry the SH output is produced normal to the surface such that $\theta_T^{2\omega}$ and $\theta_T^{2\omega}$ are 90° and 270°, which simplifies Equation 2.12. Furthermore, by introducing an effective $\chi^{(2)}$ as previously described by Dick and coworkers,[11] *d* can be pooled into the corresponding tensor element, χ_{yzy}, and eliminated from Equation 2.12. With these simplifications, $\tilde{f}_y$ for the counter-propagating geometry becomes,[12]

$$\tilde{f}_y^T = \tilde{f}_y^R = \frac{8\pi\omega}{cn_R^{2\omega}}. \tag{2.13}$$

After substituting Equation 2.13 into Equation 2.11, the reflected and transmitted SH intensity for the counter-propagating geometry can be written as,[12]

$$I_y^R(2\omega) = I_y^T(2\omega) = \frac{64\pi^2 i^2 (sin\theta_i)^2 (sin\gamma)^2 cos\gamma^2 f_y^2 f_z^2 \chi_{yzy}^2 K^2}{c^2 \left(n_R^{2\omega}\right)^2}. \tag{2.14}$$

2.6 Resonant Enhancement of SH Intensity

In section 2.3 the symmetry constraints of $\chi^{(2)}$ were used to demonstrated that SHG is extremely surface specific and therefore highly sensitive to molecules adsorbed at

the surface. As such, $\chi^{(2)}$ can also be used to demonstrate how the properties, specifically the orientation and electronic transitions, of these adsorbed molecules can lead to enhancement in the SH response. The SH intensity is proportional to the square of $\chi^{(2)}$, which consists of both a nonresonant portion, $\chi_{NR}^{(2)}$, and resonant portion, $\chi_R^{(2)}$,

$$I_{SHG} \propto \left|\chi_{ijk}^{(2)}\right|^2 \propto \left|\chi_{NR}^{(2)} + \chi_R^{(2)}\right|^2. \tag{2.15}$$

The behavior of the adsorbed molecules is described by $\chi_R^{(2)}$ and $\chi_{NR}^{(2)}$ is the susceptibility term which describes the behavior of the substrate. When a dielectric substrate, such as silica, is used $\chi_{NR}^{(2)} \approx 0$ and the SH response obtained is solely from the adsorbed molecules or $\chi_R^{(2)}$. The resonant susceptibility term is given by,

$$(\chi_{ijk}^{(2)})_R \propto N \sum_{a,b,c} \frac{\langle a|\mu_i|c\rangle\langle a|\mu_j|b\rangle\langle b|\mu_k|c\rangle}{(2\hbar\omega - E_{ca} - i\Gamma_{ca})(\hbar\omega - E_{bc} - i\Gamma_{bc})}. \tag{2.16}$$

where N is the surface density of molecules, h is Planck's constant, μ is the Cartesian coordinate dipole operator, Γ is the transition linewidth, and a, b and c represent the initial, intermediate, and final states, respectively, which are shown in the energy diagram depicted in Figure 2.2. The bra-kets in the numerator of Equation 2.16 represent the average overall possible dipole orientations of the absorbed molecules. From this it is apparent that the more anisotropic the average dipole orientation, the larger $\chi_R^{(2)}$ will become and the higher the overall SH intensity will be. In other words, if the adsorbed molecules are highly ordered with a narrow orientation distribution over all the nonlinear susceptibility tensor elements there will be an increase in $\chi_R^{(2)}$ and the SH intensity. This orientation property of $\chi_R^{(2)}$ makes biomolecular surface interactions, as discussed in the following chapters, particularly well-suited for investigation using SHG as most

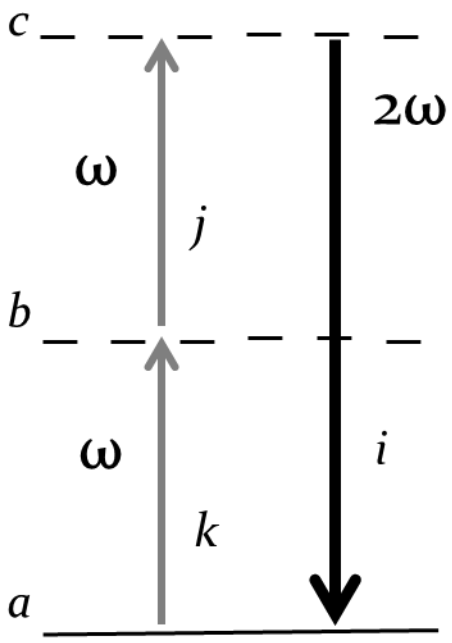

Figure 2.2. Energy diagram of SHG where two input photons (*j* and *k*) of frequency ω interact to produce an output photon (*i*) at 2ω.

biomolecules bind in a highly specific orientation to ligands at a surface. Additionally, the isotropic nature of most nonspecific biomolecular binding make SHG less sensitive to such nonspecifically adsorbed molecules, making it even easier to monitor biomolecular surface interactions. Obviously, if the nonspecific interactions show an ordered orientation there will be an SH response. However, this nonspecific response can be subtracted from the specific response by collecting the SH response in the absence of the ligand.

Another property of the adsorbed molecules that can greatly affect the overall SH response is their electronic transitions. It is apparent that when the SH output or the fundamental input is in resonance with an electronic transition of the absorbed molecule the denominator of Equation 2.16 will approach zero, which leads to in an increase in $\chi_R^{(2)}$ and the overall SH intensity. Accordingly, if the incident and SH wavelengths are chosen to correspond to the electronic transition of a molecule there will be an enhancement in the overall SH intensity, improving the sensitivity of SHG and providing the ability to detect a submonolayer of molecules.

2.7 Summary

In this chapter the general principles of counter-propagating SHG were discussed. The symmetry constraints of the second order nonlinear susceptibility tensor at a surface make SHG a highly surface specific technique with no contributions from bulk isotropic material. Accordingly, SHG is particularly well suited for probing biomolecular interactions at a surface as contributions from biomolecules in bulk solution are eliminated and no label is needed. Additionally, the highly ordered orientation of specific

biomolecular binding events also make these interactions even more ideal for SHG investigation as it can lead to an increase in the overall SH intensity. The SH intensity can be further enhanced by using a fundamental or SH frequency that is on resonance with the biomolecules being examined, making SHG an extremely sensitive label-free technique. As such, the implementation of SHG to determine the surface binding properties of various biomolecules in resonance with the SH frequency is discussed in the following chapters.

2.8 References

(1) P.A. Franken; A.E. Hill, C. W. P. G. W. *Phys. Rev. Lett.* **1961**, *7*, 118-119.

(2) Bloembergen, N.; Chang, R. K.; Jha, S. S.; Lee, C. H. *Phys. Rev.* **1968**, *174*, 813-822.

(3) Shen, Y. R. *Nature* **1989**, *337*, 519-525.

(4) Heinz, T. F.; Loy, M. M. T.; Thompson, W. A. *Phys. Rev. Lett.* **1985**, *54*, 63-66.

(5) Heskett, D.; Song, K. J.; Burns, A.; Plummer, E. W.; Dai, H. L. *J. Chem. Phys.* **1986**, *85*, 7490-7492.

(6) Corn, R. M.; Romagnoli, M.; Levenson, M. D.; Philpott, M. R. *Chem. Phys. Lett.* **1984**, *106*, 30-35.

(7) Salafsky, J. S. *Chem. Phys. Lett.* **2003**, *381*, 705-709.

(8) Hicks, J. M.; Petralli-Mallow, T. *Appl. Phys. B Lasers Opt.* **1999**, *68*, 589-593.

(9) Salafsky, J. S.; Eisenthal, K. B. *J. Phys. Chem. B* **2000**, *104*, 7752-7755.

(10) Bloembergen, N.; Pershan, P. S. *Phys. Rev.* **1962**, *128*, 606-622.

(11) Dick, B.; Gierulski, A.; Marowsky, G.; Reider, G. A. *Appl. Phys. B* **1985**, *B38*, 107-116.

(12) Kriech, M. A.; Conboy, J. C. *J. Opt. Soc. Am. B* **2004**, *21*, 1013-1022.

(13) Lambert, A. G.; Davies, P. B.; Neivandt, D. J. *Appl. Spectrosc. Rev.* **2005**, *40*, 103-145.

CHAPTER 3

COMPARISON OF THE BINDING KINETICS AND ENERGETICS OF PROTEINS BOUND TO BIOTINYLATED LIPID BILAYERS USING SECOND HARMONIC GENERATION SPECTROSCOPY

Reprinted (adapted) with permission from Nguyen, T. T.; Sly, K. L.; Conboy, J. C. *Anal. Chem.* **2012**, *84*, 201-208.

3.1 Introduction

In the previous chapter, SHG was shown to be a highly surface specific and sensitive label-free detection method that readily lends itself to detecting biomolecular interactions at a surface. It has already been demonstrated that detection of small molecule intercalation into a planar supported lipid bilayer (PSLB) is possible with SHG spectroscopy with a limit of detection of 4.5 femtomoles/cm^2.[1] Additionally, it was shown that the molecular chiral emission from a surface can be used as an intrinsic probe, allowing counter-propagating SHG to determine the binding properties of a peptide to a membrane.[2] SHG has also been used to monitor protein adsorption at a solid/liquid interface[3,4] and association of biomolecules to lipids.[2,5,6] The small molecules that have been readily monitored by SHG tend to bind in a highly ordered orientation, making

these small molecules give rise to a large SH response. On the other hand, even though proteins bind to their ligand in an ordered orientation, the large tertiary structures of proteins minimize the overall dipole orientation and lower the SH response. The SH signal can however be resonantly enhanced when the SH frequency is on resonance with an electronic transition of the proteins. Most proteins have a strong absorbance at 260-280 nm from the $\pi \rightarrow \pi^*$ transition of the tyrosine and tryptophan aromatic rings.[7] As such, a resonantly enhanced SH signal from surface bound proteins will be obtained if the SH output is tuned to a UV wavelength between 260-280 nm. As such, in this chapter it is demonstrated that with resonant enhancement, improved filtering and optimization of the SH output, SHG is able to detect nM concentrations of several biotin-bound proteins, avidin, streptavidin, neutrAvidin, and antibiotin antibody.

Avidin, streptavidin, neutrAvidin, and antibiotin antibody have all been used in a wide variety of bioanalytical applications, including monitoring biomolecule conformational changes,[8,9] biochip sensor fabrication,[10-15] and immunoassays.[16,17] Additionally, as a protein-biotin complex these four proteins have been commonly used to tether biomolecules to a surface[8,9] or used as a linker to capture biomolecules.[10-19] All four of these biotin-bound proteins have an extremely high affinity and specificity towards biotin and show high stability as a biotin-bound complex. The most common biotin-bound protein, avidin, is a tetramer consisting of 4 identical subunits, each of which has one binding site for biotin. Avidin has an extremely high binding affinity, $K_a \sim 10^{15}$ M^{-1} to free biotin in solution,[20] and forms a stable complex with biotin over a wide range of temperatures and pH values.[21] However, the basic isoelectric point (pI ~ 10)[21] of avidin causes a high degree of nonspecific adsorption, especially at physiological pH

where positively charged avidin can bind nonspecifically to negatively charged surfaces such as cell membranes[21] or silica substrates.[22] Additionally, avidin is composed of multiple carbohydrate groups, specifically four mannose residues and three N-acetyl-glucosamine residues per subunit,[23] which can increase nonspecific binding to carbohydrate-binding molecules. This proliferation of nonspecific binding seen with avidin complicates its use in bioassays. As an alternative to avidin, two of its analogs, streptavidin and neutrAvidin, have become increasingly popular in biosensors and bioassays.[10-12] Both streptavidin and neutrAvidin still retain the same high affinity and specificity towards biotin[24,25] as avidin while presumably lowering the degree of nonspecific binding. Streptavidin, which has a similar functional domain to avidin (~ 33% identical residues),[24] is a nonglycosylated protein with a slightly acidic pI of about 5-6.[21] NeutrAvidin is a commercially available deglycosylated form of avidin with a pI of 6.3.[26] The lower pIs and absence of the sugar groups in streptavidin and neutrAvidin are the factors that have been postulated to lead to a decrease in nonspecific binding. Antibiotin antibody, an immunoglobulin protein that is generated by plasma cells as part of the immune response to the antigen biotin, has also been used as a linker in biosensors[13,19] and immunoassays[27,28] as it not only exhibits extremely high specificity (~ 10^8 M^{-1}),[29] but also exhibits extremely low nonspecific binding.

Surprisingly, little work to date has compared the specific and nonspecific binding affinities of avidin, streptavidin, neutrAvidin, and antibiotin antibody to biotin at surfaces despite the use of these proteins in a broad range of biosensing applications. In this chapter the kinetics and energetics of the specific and nonspecific adsorption of all four proteins to biotinylated lipid bilayers are examined using SH spectroscopy. A typical

binding isotherm is collected for each of the four proteins binding to a biotin doped PSLB and a pure PSLB. This allows comparison between the specific and nonspecific binding responses. The thermodynamic binding constant is calculated by fitting the data to either a typical Langmuir binding model or cooperativity model, which takes into account interactions between the incoming protein and already bound protein molecules. A global fit of the adsorption of several protein concentrations was used to extract the adsorption and desorption rate of the protein-biotin complexes. The adsorption rates for individual protein concentrations were also examined to address the possible existence of protein concentration dependent binding kinetics from a population of high affinity binders at low protein concentrations. Using the same experimental conditions and analysis to examine all four proteins allows for a direct comparison of the binding properties of these biotin-protein complexes and provides useful information on these tether/linker complexes commonly used in several bioanalytical applications.

3.2 Experimental Design

3.2.1 Materials

1,2-dioleoyl-*sn*-glycero-3-phosphocholine (DOPC) and 1,2-dioleoyl-*sn*-glycero-3-phosphoethanolamine-N-(Cap biotinyl) (sodium salt) (biotin-cap-DOPE) were obtained from Avanti Polar Lipids and used as received. The structures of the lipids used are shown in Figure 3.1. NeutrAvidin™ was purchased from Pierce. Avidin from egg whites, streptavidin from Streptomyces avidinii, IgG from rabbit serum and antibiotin antibody produced in goat were obtained from Sigma-Aldrich. All water used in the experiments was obtained from a Nanopure™ Infinity Ultrapure water system with a minimum resistivity of 18.2 MΩ-cm. Phosphate buffered saline (PBS) was made from 50 mM

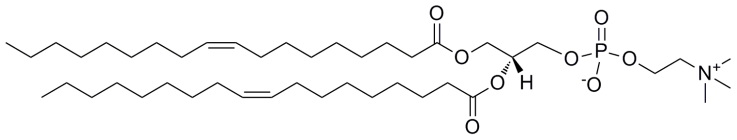

1,2-dioleoyl-s*n*-glycero-3-phosphocholine (DOPC)

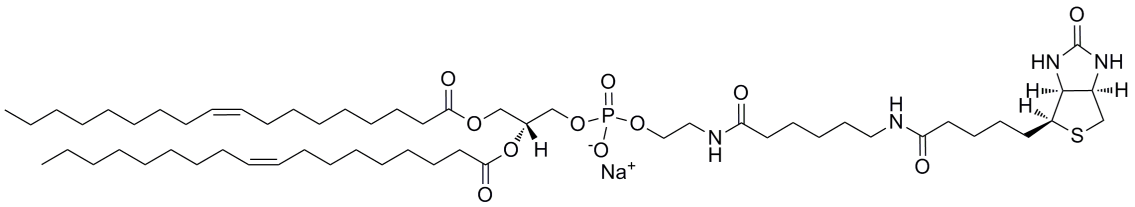

1,2-dioleoyl-s*n*-glycero-3-phosphoethanolamine-N-(Cap biotinyl)

Figure 3.1. The chemical structure of DOPC and biotin-cap DOPE.

$Na_2HPO_4 \cdot 7H_20$ and 100 mM NaCl in water and adjusted to a pH of 7.4 using NaOH. The proteins were dissolved in PBS pH 7.4 to the desired working concentrations. The substrates used for the preparation of the PSLBs were custom manufactured full spectrum grade (IR/UV) fused silica prisms (Almaz Optics). The prisms were cleaned by immersion in a solution of 70% sulfuric acid and 30% hydrogen peroxide overnight. (CAUTION: *this solution is a strong oxidant and reacts violently with organic solvents. Extreme caution must be taken when handling the solution*). Prior to use, the prisms were rinsed thoroughly with water and cleaned with Ar plasma (Harrick Scientific Plasma Cleaner/Sterilizer) for 3 mins.

3.2.2 Ligand Density

Although biosensing applications have employed the use of various types of surfaces, including functionalized gold,[10,11,17,30] glass,[8,31] silver nanoprisms,[13] PSLBs, and liposomes,[32] PSLBs were chosen as the platform for the protein binding assays in this study due to the ease of preparation and the ability to precisely control the biotin density.[33] It is important to control the surface density of the ligand as the binding affinity of the protein-ligand pair at a surface can be greatly affected.[34-36] In fact, Zhao and coworkers have shown that a biotin density greater than that necessary to bind a monolayer of avidin leads to steric hindrance of any additional avidin and lower affinity towards biotin.[35] Their study also showed that a doubly bound avidin-biotin complex (two biotin molecules for every one avidin molecule) is more stable than the singly bound complex.[35] This suggests that the optimal biotin density would be one that allows a monolayer of avidin to bind bivalently. As such, for this study the biotin density was

chosen so that a doubly bound monolayer of the protein would be formed at saturation of the binding sites. This density of biotin can be calculated using the area for avidin, 3025 $Å^2$,[21] and the area of a lipid and biotinylated lipid molecule, 70 Å.[37] For a monolayer of avidin (3.31×10^{12} molecule/cm^2) to bivalently bind to biotin, the biotin density must be twice as large; therefore, the density of the biotinylated lipid in the lipid bilayer should be about 4.6 mol % [($2 \times 3.31 \times 10^{12}$ biotinylated lipid molecule/cm^2)/(1.43×10^{14} lipid molecule/cm^2) × 100%]. The surface density of biotin calculated above is similar to the optimal biotin density seen experimentally in previous studies that investigated biotin binding to neutrAvidin and streptavidin in PSLBs where protein binding increased with biotin density up to 4 mol % and then saturated.[38,39] At 4 mol %, two biotin molecules can effectively bind to every one protein to form a doubly bound protein-biotin complex monolayer on the lipid bilayer surface. When the biotin density is lower than 4 mol %, fewer protein-ligand complexes are formed; above 4 mol %, steric hindrance from neighboring proteins decreases binding. Consequently, the biotin density chosen for these studies was 4 mol % (a monolayer coverage of bivalently bound protein), allowing the maximum number of biomolecules to be captured at the surface, which is an aim for many bioanalytical applications.

3.2.3 Planar Supported Lipid Bilayer Formation

All lipids were dissolved in chloroform then evaporated under a gentle stream of N_2(g) and vacuum dried overnight to remove residual solvent. The small unilamellar vesicle (SUV) solutions were formed by resuspending the dried lipids in PBS to a concentration of 1 mg/mL by vortexing, followed by bath sonication for 10 - 30 mins

until the solution became clear.

The prism used as the PSLB substrate was mounted in a custom built flowcell (volume of 0.4 mL). A PSLB for each experiment was formed on the silica prism by vesicle fusion, which involved incubating the surface with the SUV solution for 20 mins at room temperature. The flowcell was then flushed with PBS to remove any free lipids in solution.

3.2.4 Ligand-Protein Binding Assays

PSLBs of DOPC containing 4 mol % biotin-cap-DOPE for avidin, neutrAvidin, streptavidin and antibiotin antibody binding were created on a silica prism surface by vesicle fusion as described above. Three independent experiments were conducted for each protein, except for neutrAvidin and the antibiotin control where a t-test was conducted and resulted in the elimination of one data set for a total of two samples. To reduce nonspecific adsorption of the proteins, the PSLBs were incubated in 1mg/mL monoclonal IgG (pI ~ 6.1 – 6.5)[40] from rabbit serum in PBS pH 7.4 for 30 mins to block any defects that might exist on the lipid surfaces. For the binding of antibiotin antibody the IgG surface passivation was unnecessary. The PSLBs were then rinsed thoroughly with PBS to remove any free IgG remaining in solution.

Increasing concentrations of avidin, neutrAvidin and streptavidin ranging from 9.25 nM to 537.6 nM were injected into the flowcell and allowed to reach equilibrium. The same procedure was followed for antibiotin antibody; however, the concentration range was much narrower (4 nM to 121 nM). At each protein concentration, the SH intensity was recorded for 5 mins every 30 mins until a steady-state response was

achieved. Generally, low concentrations of the proteins required up to 4 hrs to reach equilibrium. During this period, at least 1.5 mL (~ 3 times the volume of the flowcell) of fresh protein solution was injected every 30 mins to account for the bulk depletion caused by surface adsorption of the proteins. It is important to note that protein dilutions were freshly prepared prior to each injection to further prevent the proteins from nonspecifically adsorbing to the vials and syringes. Thermodynamic measurements were made using the SH intensity collected at steady-state equilibrium for each protein concentration. Additionally, kinetic measurements were determined for the SH intensity collected over time.

To allow a direct comparison of the SH response from the specific and nonspecific binding of the proteins, the SH intensities were normalized with respect to each other. After subtracting the SH intensity of the IgG passivated DOPC bilayer, the SH response was normalized to the SH intensity of a solution of 10 mM KOH, which was injected into the flowcell after each experiment. The 10mM KOH solution provides a constant solution composition and pH for which the SH intensity did not vary significantly from experiment to experiment. Normalization of the SH intensities from the KOH solution provides a convenient means to make quantitative comparisons of the SH intensities from the specific and nonspecific binding isotherms of the proteins examined in this chapter.

3.2.5 SHG Measurements

Counter-propagating SHG was employed here. A detailed description of this technique can be found in Chapter 2 as well as other publications.[41] Briefly, a 532 nm

laser beam (2^{nd} harmonic output of a Nd:YAG laser, Surelite I, 10 Hz) with a mixed polarization state (equal amounts of *s* and *p* polarized components) was directed at the prism/water interface under total internal reflection. The laser intensity used was 14 mJ/pulse. The reflected beam was steered back to overlap spatially and temporally with the incident beam, generating an SH output at 266 nm. Optical filters were used to remove any scattered visible light before the reflected SH signal was collected by a solar-blind photomultiplier tube (Hamamatsu).

The SH intensity shown in equation 2.15 is proportional to the second-order susceptibility tensor, $\chi_{ijk}^{(2)}$, which is composed of a nonresonant and resonant portion. The resonant $\chi_R^{(2)}$ contribution described in Equation 2.16, illustrates the possible enhancement in the SH signal when the incident, ω, or SH, 2ω, frequency is resonant with an electronic transition of a molecule at the interface. This enhancement makes it possible for SHG to detect the presence of bound proteins to a lipid bilayer if the protein has electronic transitions at the frequency of the incident (532 nm) or the SH (266 nm) light. As seen in the extinction coefficient spectra of the proteins in Figure 3.2, the SH wavelength at 266 nm is in resonance with the $\pi \rightarrow \pi^*$ transitions of the protein's tryptophan and tyrosine's aromatic rings,[7] resulting in enhancement of the SH signal when the protein is present at the lipid surface. Although the electric-quadrupole response from the bulk solution or substrate can contribute to the overall SH signal,[42,43] its contribution to the measured signal is neglegible if the SH frequency is in resonance with the electric-dipole transition of molecules present at the surface.[42] Since the SH frequency used in this study is resonant with the transitions of the proteins adsorbed to the surface, the measured SH intensity is predominantly dipolar in nature with little to no

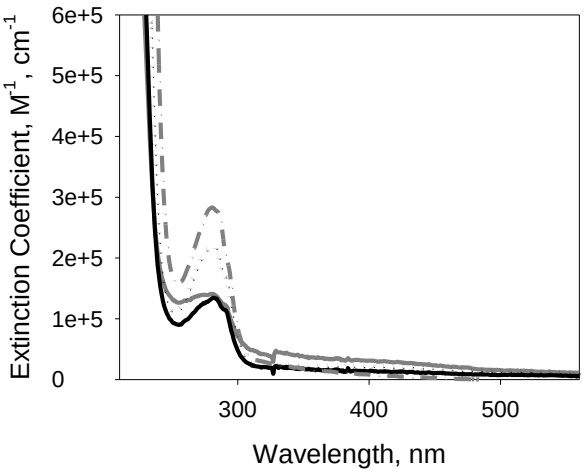

Figure 3.2. Extinction coefficient spectra of avidin (solid gray), streptavidin (dotted black), neutrAvidin (solid black), and antibiotin antibody (dash-dot black).

detectable contribution from the quadrupolar response expected.

3.2.6 Langmuir Adsorption Isotherm Equation

As mentioned earlier the SH intensity is proportional to the second-order susceptibility tensor, $\chi^{(2)}_{ijk}$. In this study it can be assumed that the nonresonant $\chi^{(2)}_{NR}$ is real due to the lack of any electronic resonances from the lipids, water or silica in the spectral region of interest, while the resonant $\chi^{(2)}_{R}$ is a complex number due to the resonance with electronic transitions in the proteins. For simplification, $\chi^{(2)}_{NR}$ and $\chi^{(2)}_{R}$ can be expressed as:

$$\chi^{(2)}_{NR} = A;\ \chi^{(2)}_{R} = B + iC\ , \tag{3.1}$$

where *A* represents the nonresonant response from the background assumed to be positive and real, and *B* and *C* denote the real and imaginary components of the resonant susceptibility due to the proteins, respectively. The SH intensity in Equation 3.1 can then be rewritten as:

$$I_{SHG} \propto \left|\chi^{(2)}\right|^2 \propto |A + N(B + iC)|^2 \propto (A + NB)^2 + (NC)^2\ . \tag{3.2}$$

Assuming the surface adsorption of the protein follows the Langmuir model, the surface density *N* in equation 3.2 is given by:

$$N = \frac{N_{max}K_o[P]}{1+K_o[P]}\ , \tag{3.3}$$

where N_{max} is the maximum surface density at saturation, K_o is the equilibrium association constant and $[P]$ is the bulk protein concentration. Substitution of Equation 3.3 into equation 3.2 gives:

$$I_{SHG} \propto \left|\chi^{(2)}\right|^2 \propto \left(A + B\frac{N_{max}K_o[P]}{1+K_o[P]}\right)^2 + \left(C\frac{N_{max}K_o[P]}{1+K_o[P]}\right)^2$$

$$\propto A^2 + 2AB\frac{N_{max}K_o[P]}{1+K_o[P]} + (B^2 + C^2)\left(\frac{N_{max}K_o[P]}{1+K_o[P]}\right)^2. \quad (3.4)$$

Assuming the value of A is real and positive, the SH intensity due to the nonresonant background in the absence of protein adsorption is given by:

$$I_{SHG}^{background} \propto A^2. \quad (3.5)$$

Subtracting the background contribution (eq. 3.5) from the measured SH intensity (eq. 3.4) and using the relationship between the surface density and SH intensity shown in Equations (2.15) and (2.16), $I_{SHG} \propto N^2$, gives the SH intensity rising solely from protein adsorption as:

$$I_{SHG} - I_{SHG}^{background} \propto 2\sqrt{I_{SHG}^{background}}B\frac{\sqrt{I_{SHG}^{Max}}K_o[P]}{1+K_o[P]} + (B^2 + C^2)\left(\frac{\sqrt{I_{SHG}^{Max}}K_o[P]}{1+K_o[P]}\right)^2, \quad (3.6)$$

where $\sqrt{I_{SHG}^{Max}}$ is the square root of the maximum SH intensity at surface saturation.

3.2.7 Cooperativity Adsorption Isotherm Equation

A previous study demonstrated that protein-protein interactions can modulate the energetics of protein association to a biotinylated surface.[34] When interactions between protein molecules are involved, a cooperative binding model presented by Zhao and coworkers[34] more aptly describes the adsorption data. The cooperative binding model expressed as,

$$N = \frac{N_{max}\omega^{\left(N/N_{max}\right)}K_o[P]}{1+\omega^{\left(N/N_{max}\right)}K_o[P]}, \quad (3.7)$$

assumes the distribution of the biotin-bound proteins follows a square lattice such that $\omega = \eta^4$ where η is the cooperativity coefficient characterizing the protein-protein interactions between neighboring protein molecules on the surface.[34] This has been

shown to be true for the avidin-biotin interaction by crystallography.[34] As done for the Langmuir adsorption isotherm, the SH intensity in terms of the cooperativity adsorption model is obtained by substituting Equation 3.7 into Equation 3.2, giving the following expression:

$$I_{SHG} - I_{SHG}^{background} \propto$$

$$2B\sqrt{I_{SHG}^{background}}\frac{\sqrt{I_{SHG}^{Max}}\omega\left(\sqrt{I_{SHG}}/\sqrt{I_{SHG}^{Max}}\right)K_o[P]}{1+\omega\left(\sqrt{I_{SHG}}/\sqrt{I_{SHG}^{Max}}\right)K_o[P]} + (B^2+C^2)\left(\frac{\sqrt{I_{SHG}^{Max}}\omega\left(\sqrt{I_{SHG}}/\sqrt{I_{SHG}^{Max}}\right)K_o[P]}{1+\omega\left(\sqrt{I_{SHG}}/\sqrt{I_{SHG}^{Max}}\right)K_o[P]}\right)^2. \quad (3.8)$$

As before, K_o is the intrinsic binding affinity of the protein to the ligand barring any protein-protein interactions.[34] When η > 1, the binding of a protein to a ligand exhibits a positive cooperativity, meaning that the protein-protein interaction enhances the ligand-protein binding. When η < 1, the protein-protein interaction reduces the ligand-protein binding, resulting in a negative cooperativity. The cooperativity model becomes the Langmuir model when η = 1.

3.3 Results and Discussion

3.3.1 Thermodynamics of Avidin, Streptavidin and NeutrAvidin Binding to Biotinylated DOPC Bilayers

The binding isotherms for avidin, streptavidin, and neutrAvidin binding to a 4 mol % biotinylated DOPC bilayer are shown in Figures 3.3, 3.4, and 3.5, respectively. The SH intensity was normalized to a solution of 10 mM KOH as described in Section 3.2.4,

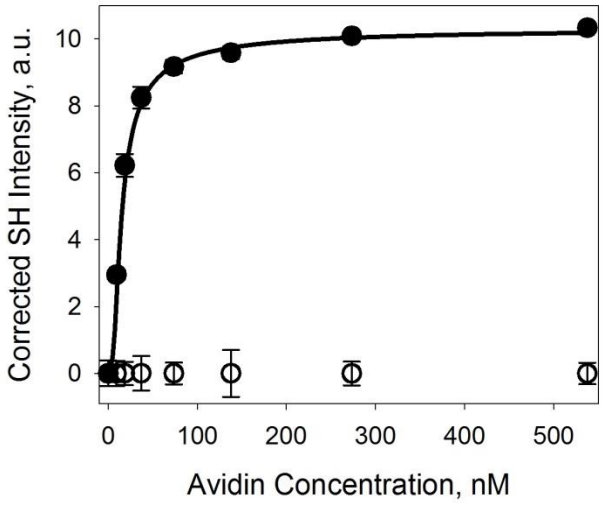

Figure 3.3. SHG intensity vs. bulk avidin concentration for avidin binding to a DOPC bilayer containing 4 mol % biotin-cap-DOPE (filled circles) and 0 mol % biotin-cap-DOPE (open circles). The line is the fit to the cooperativity binding model and the error bars represent the standard deviation from three independent experiments.

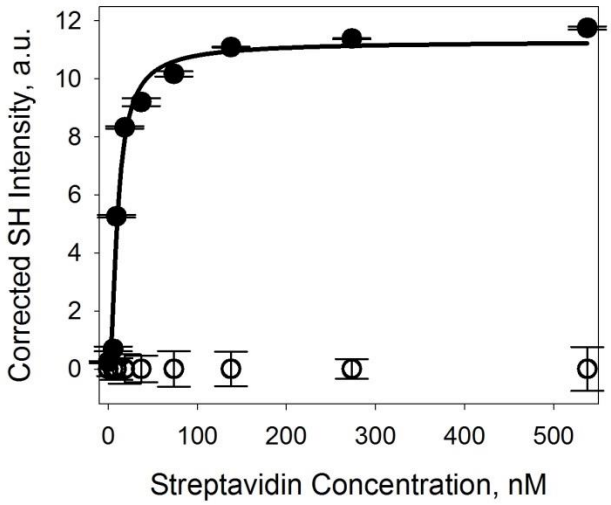

Figure 3.4. SHG intensity vs. bulk streptavidin concentration for streptavidin binding to a DOPC bilayer containing 4 mol % biotin-cap-DOPE (filled circles) and 0 mol % biotin-cap-DOPE (open circles). The line is the fit to the cooperativity binding model and the error bars represent the standard deviation from three independent experiments.

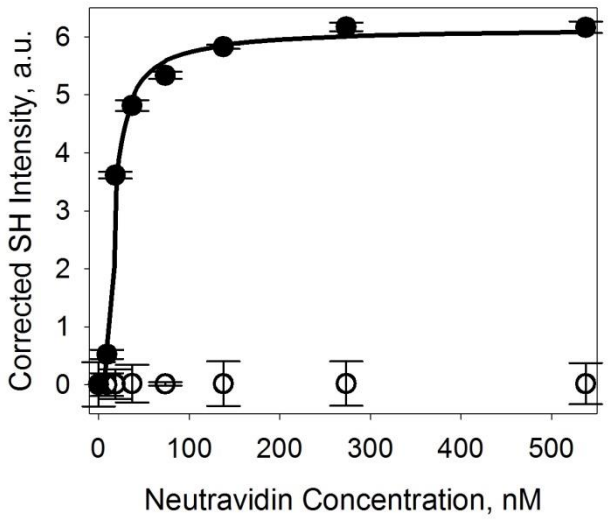

Figure 3.5. SHG intensity vs. bulk neutrAvidin concentration for neutrAvidin binding to a DOPC bilayer containing 4 mol % biotin-cap-DOPE (filled circles) and 0 mol % biotin-cap-DOPE (open circles). The line is the fit to the cooperativity binding model and the error bars represent the standard deviation from two independent experiments.

which allowed comparison between the proteins. As the protein concentration was increased the SH intensity increased until saturation of the binding sites had been reached, typically at protein concentrations above 100 nM. All three binding isotherms displayed a sigmoidal shape at low protein concentration, indicative of additional cooperative interactions.[34] As such, the binding isotherms were fit to both the typical Langmuir model and a cooperativity model where an *f*-test analysis was used to determine the best fit to the data.

The Langmuir equation shown in Equation 3.6 can be greatly reduced through analysis of the SH intensity obtained from the background response before addition of proteins and the SH response after addition of proteins. The cross-term in Equation 3.6 is the product of the nonresonant term, A, and the resonant real component, B, of the second order susceptibility tensor. This term describes the interference between the background (nonresonant) and protein adsorption (resonant) responses where the SH intensity can increase through constructive interference or decrease through destructive interference. In the data presented here, there is not an initial decrease in SH intensity at the lowest protein concentrations where the nonresonant and resonant contributions are presumably close to each other. This suggests that there is constructive interference between the resonant and nonresonant terms, meaning that the cross-term ($2AB$) in Equation 3.6 will be positive as A and B will have the same sign. Fitting the data in Figures 3.3-3.5 to Equation 3.6 with the parameters, B, C, $\sqrt{I_{SHG}^{Max}}$, and K_0 by performing a nonlinear least-squares regression, the calculated value of B is found to be approximately eight orders of magnitude smaller than C, the imaginary portion of the second order susceptibility tensor. Consequently, the second term of Equation 3.6 is dominant and the first term can be

neglected. Since the scaling factor, (B^2 + C^2), which is related to the surface density of proteins, can be pooled into $\sqrt{I_{SHG}^{max}}$ and with the aforementioned simplifications made, the Langmuir model can be expressed as:

$$I_{SHG} \propto \left(\frac{\sqrt{I_{SHG}^{max}} K_o[P]}{1+K_o[P]} \right)^2 . \tag{3.9}$$

Similarly, fitting the data to the cooperativity model in Equation 3.8 using the fitting parameters B, C, $N_{max,}$ K_o and ω, results in a value of B seven orders of magnitude smaller than C. As such, the same simplification as above can be employed for Equation 3.8, giving the expression for the cooperativity model as:

$$I_{SHG} \propto \left(\frac{\sqrt{I_{SHG}^{max}} \omega \left(\sqrt{I_{SHG}} \Big/ \sqrt{I_{SHG}^{max}} \right) K_o[P]}{1+\omega \left(\sqrt{I_{SHG}} \Big/ \sqrt{I_{SHG}^{max}} \right) K_o[P]} \right)^2 . \tag{3.10}$$

The binding isotherm data for avidin, streptavidin and neutrAvidin were fit to both the Langmuir model (Equation 3.9) and the cooperativity model (Equation 3.10). An *f*-test analysis determined that the cooperativity model fit best and the results of the nonlinear least square regression are given in Table 3.1.

The intrinsic binding affinities, K_0, obtained for the adsorption of avidin, streptavidin, and neutrAvidin to a 4 mol % biotinylated DOPC bilayer were 8.2 ± 2.4 × 10^7 M^{-1}, 4.3 ± 0.9 × 10^7 M^{-1} and 2.6 ± 0.01 × 10^7 M^{-1}, respectively. The K_o obtained in this study for avidin and streptavidin are in close agreement with previously published values obtained through fluorescence spectroscopy and SPR.[34,44] The slightly higher

Table 3.1. Measured binding kinetics and energetics for avidin, streptavidin, and neutrAvidin binding to biotinylated DOPC bilayers including the intrinsic binding affinity K_o, cooperativity coefficient η, intrinsic free energy ΔG_o, free energy due to protein-protein interactions, ΔG_η, total free energy ΔG_{total}, and apparent binding affinity K_{app} for the proteins. Data were obtained using the cooperativity binding model using the assumption that the distribution of the biotin-bound proteins follows a square lattice.[34]

Protein	$K_o \times 10^7$ **(M^{-1})**	η **(a.u.)**	ΔG_o **(kJ/mol K)**	ΔG_η **(kJ/mol K)**	ΔG_{total} **(kJ/mol K)**	$K_{app} \times 10^7$ **(M^{-1})**
Avidin	8.2 ± 2.4	1.2 ± 0.2	- 45 ± 0.8	- 1.7 ± 1.4	- 47 ± 1.7	18 ± 14
Streptavidin	4.3 ± 0.9	1.8 ± 0.2	- 44 ± 0.5	- 5.7 ± 1.1	- 49 ± 0.6	44 ± 10
NeutrAvidin™	2.6 ± 0.01	1.9 ± 0.01	- 42 ± 0.01	- 6.3 ± 0.04	- 49 ± 0.05	23 ± 0.7

value of K_o obtain here for streptavidin as compared to the previously reported value is most likely due to differences in the biotin density used. At higher ligand densities there is often steric hindrance that limits the accessibility of an incoming protein to bind to the ligand, leading to a decrease in the predicted K_o.[36] As such, the higher biotin density used in the SPR study of streptavidin on an SPR gold chip surface could have artificially lowered the predicted binding affinity.

Unlike avidin and streptavidin, the binding affinity of neutrAvidin to biotin obtained in this study is not consistent with previously published values.[25] The determined K_o for neutrAvidin to biotin by single molecule fluorescence as reported by Wayment and Harris was 4.5 orders of magnitude greater, $5.5 \pm 0.2 \times 10^{11}$ M^{-1}, than the one reported in this chapter. To further analyze this discrepancy between the binding affinities the kinetic analysis employed by Wayment and Harris was implemented in this chapter and is presented in Section 3.3.3. Results of this analysis suggest that protein concentration dependent kinetics may explain the large variance in K_o values.

The cooperativity coefficient, η, which describes the protein-protein interactions, was also determined for each adsorption isotherm by fitting the data to Equation 3.10 and is reported in Table 3.1. The adsorption of avidin, streptavidin and neutrAvidin to biotin all exhibited η values greater than one, suggesting the presence of positive protein-protein interactions. This result is not surprising as the positive contributions of protein-protein interactions have been previously reported for avidin binding to an immobilized monolayer of arachidic acid doped with a biotinylated lipid.[34] It is important to note that this fluorescence study of avidin binding to biotin found that protein-protein interactions were only present if (1) the biotin density was high enough that the distance between

adjacent biotin molecules was close enough for a bound avidin to interact with an incoming neighboring avidin and (2) the biotin accessibility to avidin had to be increased by placing a linker between the biotin and the lipid head group.[34] Both of these requirements are met in this current study, as the biotin density chosen allows a monolayer of protein to bind and a biotin-capped lipid is employed. As such, in this study a similar positive protein-protein interaction is observed for the adsorption of avidin and its analogs to biotin.

The cooperativity coefficient for avidin, 1.2 ± 0.2, was smaller than those obtained for both streptavidin, 1.8 ± 0.2, and neutrAvidin, 1.9 ± 0.01. Although this observation is interesting, it has been previously noted that streptavidin forms larger aggregates as compared to avidin and has been suggested that the greater strength of interaction between streptavidin molecules as compared to those between avidin molecules leads to increased aggregation and domain size.[35,46,47] Additionally, electrostatics may play a role in the observed protein-protein interactions. Avidin has a relatively high pI (~10) at the pH of 7.4 used in this study, meaning avidin will be positively charged. This could cause an increased electrostatic replusion between avidin molecules, whereas both streptavidin and neutrAvidin are nearly neutral at pH 7.4 and most likely do not have as much protein-protein replusion as compared to avidin-avidin interactions. The greater electrostatic replusion between avidin molecules as compared to those between streptavidin molecules or neutrAvidin molecules would decrease the positive cooperativity of avidin-avidin interactions and result in a lower observed η.

The role of the protein-protein interactions to the binding mechanism can be quantified by evaluating their contributions to the free energy of binding. The binding

free energy of the intrinsic protein-biotin interaction without any protein-protein interactions can be determined from K_o by the following expression:

$$\Delta G_o = -RTlnK_o, \tag{3.11}$$

where R is the gas constant and T is the temperature, which is equal to 25°C. Table 3.1 lists the calculated ΔG_o for the three proteins. Neglecting the free energy contributions from protein-protein interactions, the avidin-biotin and streptavidin-biotin interaction are slightly more energetically favorable than the neutrAvidin-biotin interaction with ΔG_o equal to - 45 ± 0.8 kJ/mol, - 44 ± 0.5 kJ/mol, and - 42 ± 0.01 kJ/mol, respectively.

Zhao and coworkers previously demonstrated that the free energy contributions from the protein-protein interactions, ΔG_η , could be written as:

$$\Delta G_\eta = -4RTln(\eta) \, . \tag{3.12}$$

The results of the calculated ΔG_η for each of the three proteins was determined and listed in Table 3.1. Interestingly, ΔG_η for the avidin-avidin interactions (- 1.7 ± 1.4 kJ/mol K) was approximately 3 times less than that obtained for streptavidin (- 5.7 ± 1.1 kJ/mol K) or neutrAvidin (- 6.3 ± 0.04 kJ/mol K), further illustrating the stronger protein-protein interactions between streptavidin molecules and neutrAvidin molecules as compared to avidin molecules.

The total binding free energy, ΔG_{total}, for the protein-biotin interaction with the contributions from the protein-protein interactions was determined by summing Equations 3.11 and 3.12 and the results are given in Table 3.1. The stronger protein-protein interactions seen between streptavidin molecules and neutrAvidin molecules make the ΔG_{total} obtained for streptavidin-biotin (- 49 ± 0.6 kJ/mol) and neutrAvidin-biotin (- 49 ± 0.05 kJ/mol) less than for avidin-biotin (- 47 ± 1.7 kJ/mol), meaning that

the later interaction is energetically less favorable in comparison.

The calculated ΔG_{total} can be used to determine the apparent binding affinity, K_{app}, upon inclusion of the free energy contributions from the protein-protein interactions (results are shown in Table 3.1). It is apparent that the protein-protein interactions enhance the binding affinity of all three protein-biotin interactions as K_{app} is greater than K_o in all three cases. After the contributions from the protein-protein interactions to K_o are included, avidin has the lowest K_{app} equal to $(18 \pm 14) \times 10^7$ M^{-1} while streptavidin [$(44 \pm 10) \times 10^7$] and neutrAvidin [$(33 \pm 0.7) \times 10^7$ M-1] have a relatively stronger K_{app} towards biotin.

3.3.2 Nonspecific Adsorption of Avidin, Streptavidin, and NeutrAvidin to a DOPC Bilayer

The specificity of avidin, streptavidin, and neutrAvidin towards biotin was further probed by nonspecifically adsorbing these proteins to an IgG passivated DOPC bilayer that did not contain biotin. The nonspecific adsorption was monitored as increasing bulk protein concentrations were allowed to incubate with the surface and the data is shown in Figures 3.3-3.5 as open circles. To quantify the nonspecific adsorption the square root of the SH intensity obtained at the saturation concentration of 537.6 nM, taken as complete surface coverage, was divided by the $\sqrt{I_{SHG}}$ obtained for the nonspecific adsorption at the same protein concentration. The calculated % surface coverage due to nonspecific adsorption could then be compared between avidin and its analogs. It is important to note that nonspecific adsorption might be more disordered and randomly oriented as compared to the specific adsorption of the protein, leading to a decrease in the measured SH

intensity. If the tryptophan and tyrosine residues probed in this experiment take on a more random orientation when the proteins are nonspecifically bound to a IgG passivated DOPC bilayer as compared to specifically bound to the biotinylated DOPC bilayer, the measured nonspecific adsorption might appear less than what is actually bound. Although care should be taken when comparing the nonspecific and specific binding, the trends in the observed nonspecific binding measured using SHG in this study are comparable to those found in literature.[22] It is apparent from Figures 3.3-3.5 that neutrAvidin displayed the highest degree of nonspecific adsorption, accounting for nearly 40% of the total measured surface coverage of neutrAvidin. On the other hand, both avidin and streptavidin exhibited negligible nonspecific binding to the IgG passivated DOPC bilayer. Similar results were reported for a study comparing the nonspecific adsorption of avidin, streptavidin and neutrAvidin on a negatively charged silica surface where neutrAvidin was found to have nearly 3 times more nonspecific adsorption than positiviely charged avidin or similarly neutral streptavidin.[22] It is unexpected that neutrAvidin has the highest degree of nonspecific adsorption as its deglycosylation and lower pI compared to avidin were modifications intended to decrease its nonspecific adsorption (information obtained from Pierce, Rockford, IL, USA). Even more interesting is streptavidin, a similarly deglycosylated protein with a similar pI, exhibits negligible nonspecific adsorption. Given these observations it is unlikely that the degree of glycosylation and pI of the protein are the only properties contributing to nonspecific adsorption.

3.3.3. Kinetics of Avidin Binding to a 4 mol % Biotinylated DOPC Bilayer

As mentioned previously the SH intensity was measured over time for each bulk protein concentration until a steady-state equilibrium response was reached and the SH intensity no longer increased at that protein concentration, after which the next bulk protein concentration was injected and the same protocol followed. Monitoring the protein adsorption as a function of time allowed the binding kinetics, namely the adsorption and desorption rate to be determined. Comparison of the binding affinity obtained through the kinetics and that obtained from the previous thermodynamic equilibrium measurements will provide more information on whether or not steady-state equilibrium was indeed reached for each bulk protein concentration. The avidin-biotin interaction exhibits the weakest protein-protein interactions and as such can be fairly accurately described by Langmuir kinetics[45] where the protein adsorption rate (k_{on}) is first-order with respect to the bulk protein concentration, C_{bulk}, and the fraction of unbound biotin (1-θ) while the protein desorption rate (k_{off}) is first-order with respect to the fraction of bound protein (θ). The rate of change in the surface coverage of protein is equal to the difference between the adsorption and desorption such that,

$$\frac{d\theta}{dt} = k_{on}C_{bulk}(1-\theta) - k_{off}\theta \ . \qquad (3.13)$$

θ is the fraction of protein surface coverage equal to the ratio of $\sqrt{I_{SHG}}$ to $\sqrt{I_{SHG}^{Max}}$. Application of Equation 3.13 assumes that the bulk protein concentration is unchanged with time. As mentioned in the experimental section C_{bulk} in replenished throughout the course of the adsorption process and can be considered to be nearly constant.

The SH intensity was measured continuously as C_{bulk} was increased in a single experiment, meaning all but the first C_{bulk} did not start at zero surface coverage and the

initial θ for subsequent protein concentrations is equal to the maximum θ of the previous bulk protein concentration. To adjust for this, θ for each C_{bulk} is adjusted by setting θ_o at $t = 0$ equal to the maximum θ obtained from the previous bulk protein concentration. The fraction of surface coverage for avidin binding to a 4 mol % biotinylated DOPC bilayer as a function of time for the bulk avidin concentration range of 9.25 nM to 537.6 nM is plotted in Figure 3.6.

Solving Equation 3.13 for the following boundary conditions, (1) at time $t = 0$ the initial surface coverage fraction is θ_o and (2) at any time $t > 0$ the fraction of surface coverage will equal some fraction θ. Under these conditions the following expression is obtained,

$$\theta = \frac{k_{on}C_{bulk}}{k_{on}C_{bulk}+k_{off}}\left[1 - exp\left(-k_{on}C_{bulk} + k_{off}\right)t\right] + \theta_o exp\left(-k_{on}C_{bulk} + k_{off}\right)t, \quad (3.14)$$

where θ_o is zero for the first protein concentration, after which, θ_o is equal to the maximum θ measured at the previous bulk protein concentration.

The adsorption data for all bulk protein concentrations shown in Figure 3.6 were fit simultaneously to Equation 3.14, giving the adsorption and desorption rates equal to $(9.8 \pm 5.3) \times 10^3$ M^{-1} s^{-1} and $(6.0 \pm 1.8) \times 10^{-5}$ s^{-1}, respectively. The binding affinity can be calculated by dividing the adsorption rate by the desorption rate to give a K_0 equal to $(16 \pm 10) \times 10^7$ M^{-1}. The good agreement between the K_0 obtained here and the K_{app} of avidin ($(18 \pm 14) \times 10^7$ M^{-1}) obtained through the thermodynamic equilibrium measurements suggests that each protein concentration had reached or nearly reached steady-state equilibrium. Although at the lowest avidin concentration, it appears to not have completely reached a steady-state equilibrium, meaning the obtained binding

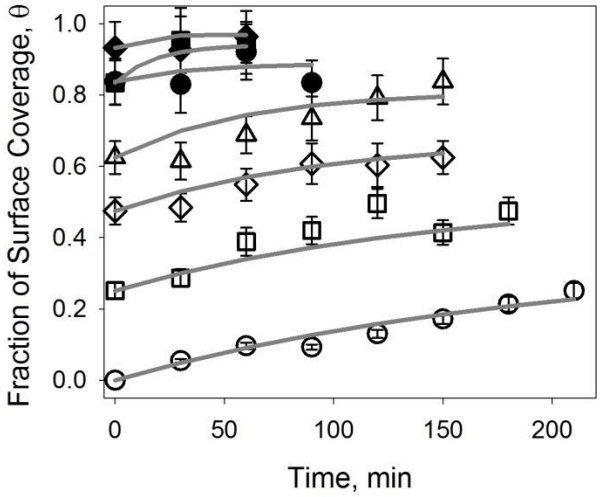

Figure 3.6. Fraction of surface coverage, θ, as a function of time for avidin binding to a 4 mol % biotinylated DOPC bilayer at the following bulk avidin concentration: 9.25 nM (open circles), 18.5 nM (open squares), 37.0 nM (open diamonds), 73.7 nM (open triangles), 137.7 nM (solid circles), 273.2 nM (solid squares), and 537.6 nM (solid diamonds). The solid lines are the global fit to equation 3.14.

kinetics may be slightly distorted.

Assuming the calculated binding kinetics of avidin to biotin are roughly indicative of the neutrAvidin-biotin interaction, the binding kinetics obtained above can be used to address the previously mentioned inconsistency between the K_0 obtained for neutrAvidin in this study and that obtained by Wayment and Harris. The measured k_{on} for Figure 3.6 is approximately 4.5 orders of magnitude slower than that obtained by Wayment and Harris [$(2.1 \pm 0.5) \times 10^8$ M^{-1} s^{-1}],[25] suggesting that the binding affinity observed here is much weaker. One plausible explanation is the existence of two binding regimes such that at low protein concentrations the protein binds biotin at a higher affinity and at higher protein concentrations the protein binds biotin at a lower affinity. The first binding regime is consistent with the results of Wayment and Harris and the latter binding regime is consistent with the result presented in this chapter. This binding behavior has been seen before for multivalent protein-ligand pairs and most likely plays a role on the measured binding affinities.[46,47] Although the lack of a visible bi-phasic binding isotherm suggests that the high affinity binders at low protein concentration most likely make up only a small population of the total surface coverage or saturate at a much lower protein concentration than measured here. Given that the lowest protein concentration used here is roughly 3 orders of magnitude greater than the protein concentration studied by Wayment and Harris who also used only enough biotin to form less than 10^{-6} of a protein monolayer,[25] it is highly possible the high affinity binders seen by Wayment and Harris are no longer detectable at the nM protein concentrations investigated in this study.

If a small population of high affinity binders is more abundant at low protein concentrations it is likely the binding kinetics would be highly dependent on the protein

concentration, especially near the shift from high affinity binders to moderate affinity binders. As such, it might be more accurate to fit the data in Figure 3.6 individually as opposed to simultaneously. Assuming the desorption rate obtained from Equation 3.14 is more or less constant for the protein concentration range examined here, the individual adsorption rates for each bulk protein concentration can be determined by using the following expression,

$$I_{SHG} = a(1 - exp^{-bx}), \tag{3.15}$$

where a is the amplitude at the maximum fraction of surface coverage and b is equal to $k_{on}[P] + k_{off}$. Since the adsorption at higher avidin concentrations does not have enough data points to fit to Equation 3.15 and the adsorption at the lowest avidin concentration does not reach a true steady-state response, only the middle 3 avidin concentrations (18.5 nM, 37 nM, and 73.7 nM) were fit to Equation 3.15. The adsorption rates were found to decrease from $(7 \pm 0.9) \times 10^5$ M^{-1} s^{-1} at 18.5 nM bulk avidin concentration to $(1.7 \pm 0.7) \times 10^5$ M^{-1} s^{-1} at 37 nM and $(5 \pm 2) \times 10^4$ M^{-1} s^{-1} at 73.7 nM. Using the desorption rate obtained from the kinetic model the calculated K_0 is found to decrease from $(1.2 \pm 0.2) \times 10^{10}$ M^{-1} to $(3 \pm 1) \times 10^9$ M^{-1} to $(9 \pm 3) \times 10^8$ M^{-1} as the bulk avidin concentration is increased from 18.5 nM to 37 nM to 73.7 nM. These results illustrate that the binding kinetics of the proteins to biotin have a strong dependence on the bulk protein concentration, suggesting that a typical binding isotherm or simultaneously fitting several bulk protein concentrations may not predict the most accurate binding affinity. Additionally, the individual adsorption rates suggest that the isotherm models may be more heavily weighted towards the higher protein

concentrations that comprise the isotherm as the value of K_0 obtained for the highest concentration (73.7 nM) examined individually was approaching the K_0 predicted from the binding isotherm data in Figure 3.3.

Obviously some error in the predicted K_0 for the bulk avidin concentrations 18.5 nM, 37 nM, and 73.7 nM exists from assuming k_{off} remains completely constant for all three concentrations. Comparison of k_{off} obtained in this study using the kinetic model and that obtain by Wayment and Harris ($(3.8 \pm 0.5) \times 10^{-4}$ s^{-1})[25] reveals there is a much lower discrepancy between the two measured values for k_{off} as compared to k_{on}, suggesting k_{off} may not be as sensitive to the bulk avidin concentration as k_{on}, especially when rebinding of the protein is assumed to be negligible. As such, it is most likely a valid assumption that k_{off} does not significantly change over the much narrower avidin concentration range examined in this chapter.

3.3.4. Binding of Antibiotin Antibody to Biotinylated DOPC

The binding isotherm for antibiotin antibody binding to a 4 mol % biotinylated DOPC bilayer is shown by the solid circles in Figure 3.7. The K_o for the data in Figure 3.7 was determined to be $1.0 \pm 0.4 \times 10^8$ M^{-1} by performing the nonlinear least-squares regression to the Langmuir binding model (Equation 3.9). The measured K_o is consistent with the value $2.8 \pm 0.8 \times 10^8$ M^{-1} obtained by a fluorescence study examining the interaction between antibiotin antibody and a 5 mol % biotin doped lipid bilayer.[29]

The binding isotherm for antibiotin antibody to a biotinylated DOPC bilayer was collected under the same experimental conditions as used for avidin, streptavidin, and

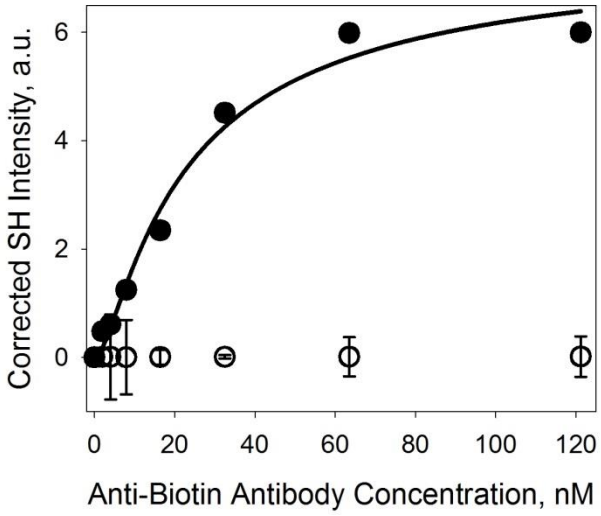

Figure 3.7. Corrected SHG intensity vs. bulk protein concentration for antibiotin antibody binding to DOPC bilayers containing 4 mol % biotin-cap-DOPE (filled circles) and 0 mol % biotin-cap-DOPE (open circles). The line is the fit to the Langmuir adsorption isotherm. The error bars represent the standard deviation from three independent positive experiments and two control experiments.

neutrAvidin, allowing for direct comparison between the binding affinities obtained for all four proteins. There were no protein-protein interactions seen in the antibiotin antibody-biotin interaction, meaning $K_o = K_{app}$. The K_{app} found for all four proteins binding to a biotinylated DOPC bilayer are similar ~ 10^8 M^{-1}. The binding free energy for antibiotin antibody (- 46 ± 1.0 kJ/mol) is also fairly similar to that of avidin and its analogs. This observation is interesting as the solution binding affinities for avidin, streptavidin, and neutrAvidin (~ 10^{15} M^{-1})[48] are much higher than the solution binding affinity for antibiotin antibody (~ 10^8 M^{-1}).[48] A previous study examining streptavidin and antibiotin antibody binding to biotin attached via a linker to bovine serum albumin also noted the similar surface binding affinities between the two protein-biotin complexes.[48] It is possible that the drastically lower binding affinity seen for avidin, streptavidin, and neutrAvidin to immobilized biotin as compared to free biotin in solution is a result of their binding affinity more strongly depending of the accessibility of biotin as compared to antibiotin antibody. Specifically, the binding sites of avidin are located in a deep depression near the end of β-barrels,[24] making it much more difficult to bind biotin when biotin is immobilized as compared to free in solution. On the other hand, the binding sites of antibiotin antibody are located at the end of the Fab segments,[49] meaning that there is less steric hindrance and greater accessibility for biotin to bind whether biotin is free in solution or immobilized on a surface. Additionally, the Fab segments of the antibody have a much greater flexibility and can move from 0° to 180°,[50] giving the antibody the ability to adjust the orientation and spacing of the binding sites in order to facilitate antibiotin antibody-biotin binding. The less hindered binding sites on antibiotin antibody make its binding affinity less dependent on the biotin accessibility as compared to

avidin.[48] The less accessible binding sites on avidin and its binding affinity having a greater dependence on the biotin accessibility are most likely why there is a significant decrease from its solution biotin to immobilized biotin binding affinity. The easily accessible binding sites of antibiotin antibody and its flexibility to make adjustments in orientation allow the binding affinity to be unaffected by the biotin accessibility as compared to avidin. As a result, the binding affinities of all four proteins, avidin, streptavidin, neutrAvidin, and antibiotin antibody to a biotinylated DOPC bilayer are relatively the same. As will be discussed in Chapter 7, the binding affinities reported here could be mass transport limited and may also explain why a lower surface binding affinity is reported for avidin and its analogs as compared to their solution binding affinities.

The nonspecific binding of antibiotin antibody to a pure DOPC bilayer was also monitored for increasing protein concentrations and is shown in Figure 3.7 as open circles. It is apparent from the data that there is negligible nonspecific adsorption of antibiotin antibody to the DOPC bilayer. It is interesting to note that IgG was not used to reduce the nonspecific binding of antibiotin antibody. The reduced nonspecific adsorption without additional chemical passivation may make the antibiotin antibody-biotin interaction a valuable complex in bioanalytical applications as the time and cost of minimizing the nonspecific binding can be avoided without seeing a reduction in binding affinity.

3.3.5 Limit of Detection of SHG

A quantitative assessment of the limit of detection (LOD) of SHG was made by using the spectroscopic sensitivity determined from the calibrated SH intensity and the standard deviation of the measured signal using the following expression,

$$LOD = \frac{\sigma}{sensitivity} \tag{3.16}$$

where σ is the average standard deviation of the background before addition of the proteins. The *sensitivity* is obtained from the calibrated SH intensity measure for each protein-biotin binding isotherm and is equal to the slope obtained from plotting the surface excess Γ (molecules/cm^2) as a function of bulk protein concentration. The maximum surface excess is taken as the number of protein molecules that form a complete monolayer multiplied by the measured SH intensity at the saturation concentration. The surface excess for protein concentrations below the saturation concentration are calibrated to the maximum surface excess using the average SH intensity detected for that protein concentration. The lowest LOD is found for antibiotin antibody (2.4 ng/cm^2 or 17 femtomoles/cm^2), followed by avidin (5.3 ng/cm^2 or 80 femtomoles/cm^2) and streptavidin (4.4 ng/cm^2 or 84 femtomoles/cm^2), with the highest LOD for neutrAvidin (8 ng/cm^2 or 133 femtomoles/cm^2). It is not surprising that the LOD for the proteins examined in this chapter was lower than that obtained by Kriech and Conboy for a chiral small molecule,[1] as the tryptophan and tyrosine residues giving rise to the detected SH intensity for the proteins have a much lower net orientation than the highly ordered orientation of the chiral small molecule. The lower net orientation of the proteins and lower extinction coefficient at the SH wavelength (266 nm) leads to the much lower SH response. Despite the low SH response from the proteins, an LOD on par

with other label-free detection methods for surface biomolecular reactions was obtained using SHG. It is important to note that several enhancing methods could be used to increase the LOD, such as surface enhancement by using a metal surface[51,52] or increased resonant enhancement by probing the proteins with an SH output closer to the electronic transition peak at 280 nm. Even without further signal enhancement, this study demonstrates SHG is a valuable label-free technique capable of examining unique binding properties of protein-ligand interactions at the surface of PSLBs.

3.4 Summary

In this chapter the binding of avidin, streptavidin, neutrAvidin, and antibiotin antibody to a biotinylated DOPC lipid bilayer was investigated using SHG. The binding affinities of avidin, streptavidin and neutrAvidin to a biotin doped lipid bilayer were determined. Analysis of the binding isotherms indicated a positive cooperative binding behavior where protein-protein interactions enhance the binding between the proteins and biotin. Upon calculating the binding free energy, it was determined that streptavidin and neutrAvidin binding to biotin are more energetically favorable as compared to the avidin-biotin interaction. This is primarily a result of the stronger protein-protein interactions seen for both streptavidin and neutrAvidin. Comparison of the nonspecific adsorption to a pure DOPC bilayer revealed that neutrAvidin has the highest degree of nonspecific adsorption while both streptavidin and avidin have negligible amounts of nonspecific adsorption. Additionally, the binding affinity of antibiotin antibody was shown to be similar to that of avidin, streptavidin, and neutrAvidin. Antibiotin antibody also exhibits negligible nonspecific adsorption to a pure DOPC bilayer even without any additional

chemical to passivate the surface. The LOD of SHG for the proteins is in the ng/cm^2 range, suggesting that SHG is a suitable alternative to other label-free methods for the investigation of surface protein-ligand interactions. Furthermore, this chapter presents important binding properties of avidin, streptavidin, neutrAvidin and antibiotin antibody to biotin, which may prove valuable for biosensing and other bioanalytical applications.

3.5 References

(1) Kriech, M. A.; Conboy, J. C. *Appl. Spectrosc.* **2005**, *59*, 746-753.

(2) Kriech, M. A.; Conboy, J. C. *J. Am. Chem. Soc.* **2003**, *125*, 1148-1149.

(3) Salafsky, J. S.; Eisenthal, K. B. *J. Phys. Chem. B* **2000**, *104*, 7752-7755.

(4) Hicks, J. M.; Petralli-Mallow, T. *Appl. Phys. B Lasers Opt.* **1999**, *68*, 589-593.

(5) Fujii, S.; Morita, T.; Kimura, S. *J. Pept. Sci.* **2008**, *14*, 1295-1302.

(6) Mitchell, S. A. *J. Phys. Chem. B* **2009**, *113*, 10693-10707.

(7) Havel, H. A.; Chao, R. S.; Haskell, R. J.; Thamann, T. J. *Anal. Chem.* **1989**, *61*, 642-650.

(8) Grunwell, J. R.; Glass, J. L.; Lacoste, T. D.; Deniz, A. A.; Chemla, D. S.; Schultz, P. G. *J. Am. Chem. Soc.* **2001**, *123*, 4295-4303.

(9) Wennmalm, S.; Edman, L.; Rigler, R. *Proc. Natl. Acad. Sci. U. S. A.* **1997**, *94*, 10641-10646.

(10) Ladd, J.; Boozer, C.; Yu, Q.; Chen, S.; Homola, J.; Jiang, S. *Langmuir* **2004**, *20*, 8090-8095.

(11) Esseghaier, C.; Helali, S.; Ben Fredj, H.; Tlili, A.; Abdelghani, A. *Sens. Actuators, B* **2008**, *B131*, 584-589.

(12) Sun, H.; Choy, T. S.; Zhu, D. R.; Yam, W. C.; Fung, Y. S. *Biosens. Bioelectron.* **2009**, *24*, 1405-1410.

(13) Hall, W. P.; Ngatia, S. N.; Van Duyne, R. P. *J. Phys. Chem. C* **2011**, *115*, 1410-1414.

(14) Bashir, R.; Gomez, R.; Sarikaya, A.; Ladisch, M. R.; Sturgis, J.; Robinson, J. P. *Biotechnol. Bioeng.* **2001**, *73*, 324-328.

(15) Lazcka, O.; Del Campo, F. J.; Munoz, F. X. *Biosens. Bioelectron.* **2007**, *22*, 1205-1217.

(16) Barton, A. C.; Davis, F.; Higson, S. P. J. *Anal. Chem.* **2008**, *80*, 9411-9416.

(17) Zhavnerko, G. K.; Yi, S. J.; Chung, S. H.; Yuk, J. S.; Ha, K. S. *NATO Sci. Ser., II* **2004**, *152*, 95-108.

(18) Cooper, M. A. *Nat. Rev. Drug Discovery* **2002**, *1*, 515-528.

(19) Litos, I. K.; Ioannou, P. C.; Christopoulos, T. K.; Traeger-Synodinos, J.; Kanavakis, E. *Biosens. Bioelectron.* **2009**, *24*, 3135-3139.

(20) Green, N. M. *Biochem. J.* **1963**, *89*, 585-591.

(21) Green, N. M. *Adv. Protein Chem.* **1975**, *29*, 85-133.

(22) Wolny, P. M.; Spatz, J. P.; Richter, R. P. *Langmuir* **2010**, *26*, 1029-1034.

(23) DeLange, R. J. *J. Biol. Chem.* **1970**, *245*, 907-916.

(24) Green, N. M. *Methods Enzymol.* **1990**, *184*, 51-67.

(25) Wayment, J. R.; Harris, J. M. *Anal. Chem.* **2009**, *81*, 336-342.

(26) Priece Biotechnology. *Instructions for NeutrAvidin*, (prod. number 31000).

(27) Danilowicz, C.; Manrique, J. M. *Electrochem. Commun.* **1999**, *1*, 22-25.

(28) Mushahwar, I. K.; Spiezia, K. S. *J. Virol. Methods* **1987**, *16*, 45-54.

(29) Jung, H.; Yang, T.; Lasagna, M. D.; Shi, J.; Reinhart, G. D.; Cremer, P. S. *Biophys. J.* **2008**, *94*, 3094-3103.

(30) Xu, F.; Zhen, G.; Yu, F.; Kuennemann, E.; Textor, M.; Knoll, W. *J. Am. Chem. Soc.* **2005**, *127*, 13084-13085.

(31) Osborne, M. A. *J. Phys. Chem. B* **2005**, *109*, 18153-18161.

(32) Patel, A. R.; Frank, C. W. *Langmuir* **2006**, *22*, 7587-7599.

(33) Sandrin, L.; Coche-Guerente, L.; Bernstein, A.; Basit, H.; Labbe, P.; Dumy, P.; Boturyn, D. *Org. Biomol. Chem.* **2010**, *8*, 1531-1534.

(34) Zhao, S.; Walker, D. S.; Reichert, W. M. *Langmuir* **1993**, *9*, 3166-3173.

(35) Zhao, S.; Reichert, W. M. *Langmuir* **1992**, *8*, 2785-2791.

(36) Shi, J.; Yang, T.; Kataoka, S.; Zhang, Y.; Diaz, A. J.; Cremer, P. S. *J. Am. Chem. Soc.* **2007**, *129*, 5954-5961.

(37) Marsh, D. *CRC Handbook of Lipid Bilayers*; CRC Press: Boca Raton, Florida, 1990.

(38) Smith, K. A.; Gale, B. K.; Conboy, J. C. *Anal. Chem.* **2008**, *80*, 7980-7987.

(39) Mao, H.; Yang, T.; Cremer, P. S. *Anal. Chem.* **2002**, *74*, 379-385.

(40) Wu, X.-Z.; Huang, T.; Mullett, W. M.; Yeung, J. M.; Pawliszyn, J. *J. Microcolumn Sep.* **2001**, *13*, 322-326.

(41) Kriech, M. A.; Conboy, J. C. *J. Opt. Soc. Am. B: Optical Physics* **2004**, *21*, 1013-1022.

(42) Guyot-Sionnest, P.; Shen, Y. R. *Phys. Rev. B Condens. Matter* **1987**, *35*, 4420-4426.

(43) Shen, Y. R. *Appl. Phys. B: Lasers Opt.* **1999**, *68*, 295-300.

(44) Tang, Y.; Mernaugh, R.; Zeng, X. *Anal. Chem.* **2006**, *78*, 1841-1848.

(45) Langmuir, I. *J. Am. Chem. Soc.* **1918**, *40*, 1361-1402.

(46) Emerson, D.; Juliano, R. L. *J. Cell. Physiol.* **1982**, *111*, 171-176.

(47) Stanley, P.; Carver, J. P. *Proc. Natl. Acad. Sci. U. S. A.* **1977**, *74*, 5056-5059.

(48) Vincent, P.; Samuel, D. *J. Immunol. Methods* **1993**, *165*, 177-182.

(49) Tsai, C. S. *Biomacromolecules: Introduction to Structure, Function and Informatics*; John Wiley & Sons: New Jersey, 2007.

(50) Hanson, D. C.; Yguerabide, J.; Schumaker, V. N. *Biochemistry* **1981**, *20*, 6842-6852.

(51) Arfaoui, I.; Bermudez, V.; De Nadai, C.; Jalkanen, J.-P.; Kajzar, F.; Leigh, D.; Lubomska, M.; Mendoza, S. M.; Niziol, J.; Rudolf, P.; Zerbetto, F. *Proc. SPIE-Int. Soc. Opt. Eng.* **2005**, *5724*, 139-148.

(52) Chen, Z.; Chen, W.; Zheng, J.; Wang, W.; Zhang, Z. *Springer Ser. Opt. Sci.* **1985**, *49*, 324-325.

CHAPTER 4

SURFACE SECOND HARMONIC LENS-LESS IMAGING

Reprinted (adapted) with permission from Sly, K., Nguyen, T.T., and Conboy, J.C. *Opt. Express.***2013**, *20*, 21953-67.

4.1 Introduction

In the previous chapter, SHG was shown to be a valuable and sensitive surface science spectroscopic technique. Despite the high degree of sensitivity of SH spectroscopy seen in Chapter 3, only one interaction could be examined at a time. Implementing SHG as an imaging technique would enable high-throughput examination to allow direct label-free imaging with time-resolution capabilities.[1] In this chapter, the unique coherent nature of SH imaging is investigated and used to demonstrate the potential of employing lens-less surface SH imaging for biomolecular interactions.

Hellwarth and Christensen were the first to demonstrate SHG imaging when they combined SHG with an optical microscope in 1974.[2] SHG has since been used as a surface sensitive imaging technique to visualize the uniformity of the interfacial region of a metalloporphyrin film,[3] the carrier motion at interfaces of organic devices,[4] and the chirality of surface immobilized small molecules.[5] Although SHG imaging has been extensively employed in the field of biological tissue imaging,[6,7] these studies have

utilized the bulk structural symmetry of proteins in tissue or cells to generate the SH signal. The reports of surface SHG imaging (SSHGI) of biological interfaces are primarily limited to studies that probe SH-active dye molecules to monitor membrane potential,[8,9] individual liposomes,[10] and kinetic transport.[11,12] In efforts to reach single molecule detection, membrane proteins labeled with a gold nanoparticle have also been examined using SHG imaging.[13] Recently, a label-free SSHGI study in our lab probed drug-lipid interactions at a liquid/solid interface in a high-throughput manner.[14]

All of the aforementioned studies convey the versatility of SSHG and its effectiveness in imaging, but like most other imaging techniques the previous SSHG imaging studies utilized a lens system to reconstruct the surface image from the emitted SHG light. In this chapter, it is shown that the long coherence length and plane-wave nature of surface SHG minimizes diffraction and therefore makes lens-less SSHG imaging possible. Admittedly the idea of removing the lens from an imaging system is not new. Electron microscopy without lenses was demonstrated in 1948 by Gabor et al. when he used the recorded image of the Fresnel diffraction pattern from an object to reconstruct the image of the object;[15] however, this lens-less holographic imaging technique requires algorithms to reconstruct the image of the object.[16] Although advances in lens-less holographic microscopy designed to eliminate the need for propagation algorithms, such as wavelength multiplexing,[16] have been demonstrated, a reconstruction and decoding stage is still necessary. Thus, despite overcoming some of the shortcomings of lenses, holographic microscopy inherently only allows for indirect imaging. If an optical imaging system could directly image the amplitude distribution from a surface without incorporation of an objective lens, it would greatly simplify the

imaging process while still avoiding the limitations of lenses. Ideally, the incorporation of an objective lens in an optical imaging system should only be necessary to resolve an image if diffraction and scattering effects cause divergence of the beam as it travels through space.[17] When SSHG is produced with the use of a collimated light source with limited divergence, a collimated coherent plane-wave is produced. Theoretically, under these conditions, the need for an objective lens could be eliminated.

In order to test the feasibility of lens-less SSHGI, images of various sized lipid bilayers containing an SH active molecule were obtained at several distances. According to optical beam propagation theory, the transverse amplitude distribution or intensity is dependent on the propagation distance and the initial beam width.[18] In SSHGI, each object behaves as a local emitter of light and produces its own propagating beam where the object size can be taken as the initial beam width. Since the object size is related to the initial beam width, it will influence how rapidly the transverse amplitude distribution spreads as the beam propagates through space.[18] Therefore, the behavior of the SHG propagating beam from each lens-less image can be characterized by analyzing the imaged object beam width as a function of distance using optical beam propagation theory. To further demonstrate that minimal divergence is required for imaging without an objective lens a comparison to an identically set up lens-less fluorescence imaging study where the generated wave-front is instantaneously spherical was also conducted.

To the best of the authors' knowledge, this idea of imaging without a lens using surface SHG has never been demonstrated and more significantly lens-less imaging has never before been demonstrated in the ultraviolet wavelength range. The lens-less SSHG imaging method presented in this chapter is considerably simpler than lens-less

holographic microscopy. No reconstruction of the object is necessary as the intrinsic second harmonic amplitude distribution of the object can be directly imaged, thus only requiring an array detector. Additionally, the removal of the microscope and objective lens allows more light to be collected, increasing the overall photon collection efficiency as it eliminates the amount of light loss through a microscope and aperture. Furthermore, without the objective lens the field of view or detection area is no longer limited by the magnification of the objective lens, but rather the size of the beam or illumination area. The larger detection area possible with lens-less SSHG imaging could increase throughput significantly relative to imaging with an objective lens, which in the field of biosensors and medical diagnostics would be advantageous. On a more fundamental level, the lens-less SSHG imaging method presented in this chapter illustrates the differences between coherent and incoherent imaging. Coherent plane-wave imaging was thoroughly investigated using Gaussian beam propagation theory to describe the effect of the object size and the detector-sample distance on image formation and diffraction. Gaussian beam propagation theory was also shown to accurately describe the observed lens-less SSHG images.

4.2 Theory of Lens-less SHG Imaging

In a typical imaging system, diffraction caused by the transverse spreading of the light source leads to an unavoidable increase in the imaged object beam width as the propagation distance increases.[17] For this reason focusing elements, such as a lens, are used to reconstruct the image at some distance from the object.[17] However, if there were minimal transverse spreading and therefore negligible change in the imaged beam width,

images could be resolved without the use of a lens. Since transverse spreading results when the electromagnetic waves emitted from an object are not parallel, not in phase, or not planar, an imaging source that produces parallel waves with constant phase and frequency is needed if one wishes to eliminate the need for an objective lens. In other words, lens-less imaging is only possible if the imaged light source is a collimated (parallel), coherent (in phase) plane wave (constant phase and frequency). Surface SHG is a technique that under the proper conditions can generate a plane-wave that is both coherent and collimated over a long distance providing the possibility for lens-less imaging.

The SH response from the surface is produced when two light waves of the same frequency are spatially and temporally overlapped at the surface.[19] The resulting SHG emission can be described by:

$$I_{SH} \propto \left| f_{SH} f_w^2 \chi^{(2)} \right|^2 \tag{4.1}$$

where $\chi^{(2)}$ is the nonlinear susceptibility tensor and f_{SH} and f_w are the Fresnel coefficients for the SH and incident fields. $\chi^{(2)}$ dictates the interaction of the applied electric fields $E_1(w)$ and $E_2(w)$, and the resulting SH field at the surface. Since SHG is a second-order nonlinear process in which two photons of the same frequency are spatially and temporally overlapped (no relative phase change) to generate a third photon of twice that frequency (narrow frequency distribution), there exists a near constant phase and frequency in the output and thus coherent plane waves are generated. The two incoming electromagnetic waves, *A* and *B*, with the same frequency, ω, can be written as:[20,21]

$$f(x,t) = A\exp\left[i\left(k_1(\omega)x - \omega t + \delta_A(t)\right)\right] \tag{4.2}$$

$$f(x,t) = B\exp\left[i\left(k(\omega)x - \omega t + \delta_B(t)\right)\right] \tag{4.3}$$

where k is the propagation vector, A and B are the amplitude of waves travelling some distance x over time t, and δ_A and δ_B are the phase factors for wave A and B, respectively. Since the frequency distribution of waves A and B is narrow due to the monochromatic incident light, then on average δ_A and δ_B do not change significantly for a given period. Additionally, since the two electromagnetic waves interact in such a way that there is no relative phase difference, $\delta(t) = \delta_B(t) - \delta_A(t) = 0$, the generated SHG wave can be described by:

$$f(x,t) = E(2\omega)\exp\left[i\left(k_{SH}(2\omega)x - 2\omega t\right)\right]. \tag{4.4}$$

Due to the incident beams having both a narrow frequency distribution and negligible phase difference there is minimal constructive and destructive interference,[20] producing an SHG output that has a constant relative phase and is therefore coherent. The coherence of the electromagnetic waves creates infinite parallel planes of uniform amplitude distribution (constant frequency and phase), meaning that the generated surface SHG wave has a planar wave-front. However, the above derived expressions are only valid under the assumption that the incident waves are plane-waves where the sum of the propagation vectors for each of the incident beams are parallel and thus propagate in a single direction. If the incident beams were focused on the sample their wave-fronts would be near radial due to the large distribution of k vectors. Consequently, in order to assure the incident beams are plane-waves having a single propagation direction, they

must be highly collimated.

In the counter-propagating SHG geometry used here (shown in Figure 4.1) where the two incident light waves approach the sample from opposing directions there is a change of sign in the x component of the propagation vector, which due to the conservation of momentum, the generated SH signal is produced normal to the surface. Generating the SHG output normal to the surface further eliminates any distortion to the wave-front caused by emission at an angle, which helps produce a more planar wave-front.

Under the conditions described above, surface SHG generates both a collimated and coherent electromagnetic plane-wave where transverse spreading is negligible over a significant distance. In principle, imaging without an objective lens should be possible. However, since the generated wave is not stationary it is important to consider the behavior of the plane-wave as it propagates through space. A plane-wave of constant phase and frequency can persist and propagate along a given direction (*z* axis) if the plane (x-y plane) is also infinitely perpendicular to the propagation axis. From an imaging perspective, the objects which generate the SH field will be of finite dimension, and thus generation of an infinite plane-wave is not possible.[22] However, if the object dimension is a sufficiently large number of wavelengths there will be a slow rate of transverse spreading and the plane-wave approximation can be made. Additionally, since SHG produces relatively narrow and highly collimated beams which propagate relatively parallel to the optical axis, the paraxial approximation can also be used.[18] Assuming the SHG output from each object has an ideal Gaussian intensity profile (TEM_{00} Gaussian mode) the SHG beam can be described by solutions to the paraxial wave equation for a

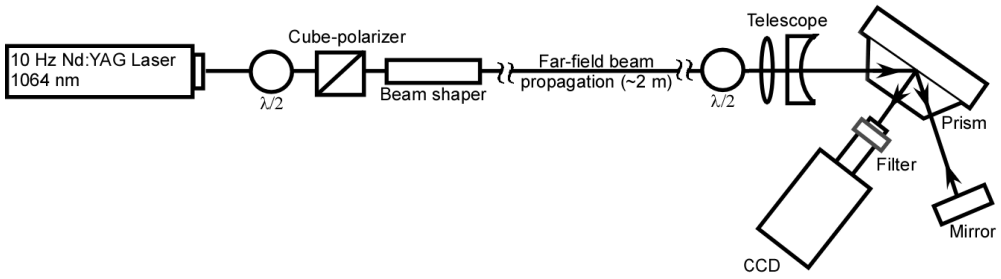

Figure 4.1. Schematic of the counter-propagating lens-less SHG setup.

coherent plane-wave with a Gaussian intensity profile. The solutions to the wave equation under these conditions lead to two important beam parameters, the object width ($w(z)$) and the radius of curvature ($R(z)$), which represent the expansion of the beam width with propagation distance and the curvature of the phase front, respectively. (shown graphically in Figure 4.2 (A) and (B)).[23]

The variation of the image width at any plane at some distance *z* perpendicular to the propagation axis can be described as follows,[18]

$$w(z) = w_0 \sqrt{1 + \left(\frac{\lambda z}{\pi w_0^{\,2}} \right)^2}, \tag{4.5}$$

where w_0 is the initial object width and λ is the wavelength. From the above equation it can be seen that the divergence of the beam or spreading of the image width is not only dependent on the propagation distance, but is also highly dependent on the initial object width where small objects lead to a much more rapid transverse spreading of the beam and a greater deviation from an ideal plane-wave. The curvature of the phase front of the beam at any distance *z* can be determined by,

$$R(z) = z \left[1 + \left(\frac{\pi w_0^{\,2}}{\lambda z} \right)^2 \right]. \tag{4.6}$$

Equation (4.6) demonstrates that as the distance from the object increases $R(z)$ becomes larger and significant curvature of the wave-front occurs. At sufficiently large distances from the object the beam has a spherical wave-front; this drastic deviation from a plane wave-front causes classic diffraction. The distance at which the wave-front is no longer

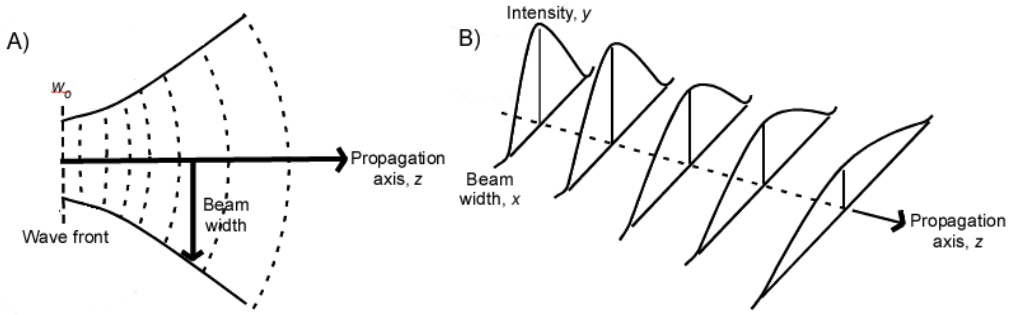

Figure 4.2. Schematic diagram of Gaussian beam propagation. (A) Propagating wave front showing a near planar wave-front increase in curvature as distance increases (B) Propagating beam showing increase in beam width and transverse spreading and decrease in intensity as distance increases. (Reconstructed from Ref. 17).

planar, or collimated, occurs when $w(z)$ has increased by $\sqrt{2}w_0$.[18] This distance is referred to as the Rayleigh range or confocal distance, z_R, and can be determined by setting equation 4.5 equal to $\sqrt{2}w_0$ and solving for z to give,[18]

$$z = z_R = \frac{\pi w_0^2}{\lambda}. \tag{4.7}$$

As seen in equation 4.7, the smaller the initial object width, w_0, the shorter the collimated region.[17] Past this collimated region where the wave-front is significantly curved, diffraction will be evident and imaging without a lens system would not be possible. Consequently, the ability to image without a lens is dependent on both the initial object size and the object-image distance.

In order to test the hypothesis that lens-less SSHGI is possible without a lens system, SHG images of a lipid bilayer containing an SH active molecule, (*s*)-(+)-1,1'-bi-2-naphthol (SBN, 99%), patterned into various sized line-widths using the United States Air Force (USAF) test pattern were obtained at several object-image distances. Imaging different sized objects at different distances provides an efficient means of evaluating lens-less SSHG imaging using Gaussian beam propagation theory.

4.3 Experimental Design

4.3.1 Materials

DOPC and 1,2-dioleoyl-*sn*-glycero-3-phosphoethanolamine-N-(lissamine rhodamine B sulfonyl) (rhodamine-cap-DOPE) were obtained from Avanti Polar Lipids and used as received. SBN was obtained from Sigma Aldrich and used as received. The

structures of rhodamine-cap-DOPE and SBN are shown in Figure 4.3. The structure for DOPC was shown in Figure 3.1. All water, PBS buffer and cleaning of the fused silica prisms were the same as described in section 3.2.1 of Chapter 3. SBN was dissolved in PBS pH 7.4 to the desired working concentration (55 μM).

4.3.2 PSLB Pattern Preparation

The PSLBs were formed using vesicle fusion as described in section 3.2.3 of Chapter 3. Following the rinse with PBS buffer to remove unbound lipids, the 1951 (USAF) positive resolution test target (chrome pattern on UV transparent glass) purchased from Edmund Optics was placed on top of the PSLB gently and taped down allowing only a small water layer to remain between the PSLB and test target. The prism with the resolution test target attached was placed in an ultraviolet ozone (UVO) cleaner (Jelight Co.) with a low pressure mercury vapor grid lamp for 13 mins. The PSLB not covered by the chrome pattern was etched by the UV light to form the positive resolution test pattern.[24] After formation of the resolution test pattern, the prism was removed and mounted in a custom built flowcell (volume of 0.4 mL) under Ultrapure water. SBN was then injected into the flowcell and allowed to adsorb to the patterned DOPC bilayer. SBN was chosen because it resonantly enhances the SH emission and preferentially intercalates into the DOPC bilayer.[5] As such, a large SH response is seen where SBN has intercalated into the bilayer left from the pattern, while there is minimal SH response where the bilayer has been etched away due to the negligible nonspecific adsorption of SBN to the silica prism. After intercalation of the SBN into the bilayer, the flowcell was flushed with PBS to remove any unbound SBN before images were taken.

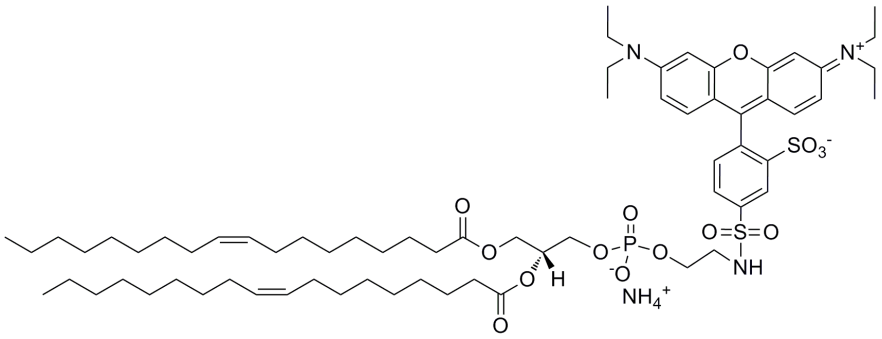

1,2-dioleoyl-*sn*-glycero-3-phosphoethanolamine-N-(lissamine rhodamine B sulfonyl) (rhodamine-cap-DOPE)

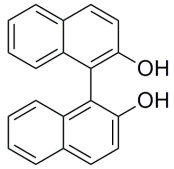

(*s*)-(+)-1,1'-bi-2-naphthol (SBN)

Figure 4.3. Chemical structure of Rh-cap-DOPE and SBN.

4.3.4 SHG Imaging

Counter-propagating SHG imaging was used to detect the SBN-lipid membrane patterned substrate.[5] A schematic of the optics and setup is shown in Figure 4.1. The second harmonic output (532 nm) of a Nd:YAG laser (Continuum, Surelite I, 20 Hz, 7ns) was first directed through a half-wave plate and cube polarizer to adjust the power. The laser beam was then sent through a beam shaper (MolTech GmbH, 6 mm π-shaper) to create a uniform amplitude distribution across the beam profile while maintaining the polarization of the beam. To further homogenize the beam intensity distribution and wave-front, a Keplerian telescope was used to bring the beam to a focus. The beam was then resized (beam width of ~ 3mm) and collimated over a long distance ~ 2m using a Galilean telescope, after which the beam, with an energy of 20 mJ/pulse as measured at the sample position, was directed onto the surface of the prism under total internal reflection. The reflected beam was steered back on itself so as to spatially and temporally overlap with the incident beam. The resulting SHG photons were emitted at 266 nm along the surface normal. A UV solar blind filter (OFIL, Ltd, Israel) was used to allow light only from the SHG signal to be collected.

SHG image acquisition was achieved using a CCD camera (Andor, 1024 x 1024 pixels). Images were taken at 5 different distances from the sample, ranging from 7.6 cm to 40 cm. All SHG images were collected for 60 mins to produce the final image. The software package Image J (http://rsbweb.nih.gov/ij/index.html) was used to analyze the SHG images. After background subtraction of the minimum pixel intensity from the images, the images were flat-field corrected using the Image J macro available at the Integrated Microscopy Core Facility at the University of Chicago

(http://digital.bsd.uchicago.edu/%5Cimagej_macros.html) in order to correct for any variations in the illumination beam intensity.

4.3.5 UV Back Illumination Imaging

UV back illumination images of the 1951 (USAF) negative resolution test target (UV transparent glass pattern with a chrome covered background) were collected using a low pressure mercury UV pen lamp (Beckman Coulter, Inc.) as the light source. The light from the pen lamp was collimated and sent through a fused silica diffuser to create a more uniform intensity profile. A narrow bandpass filter was used to select only the 254 nm line of the mercury lamp. Images were collected using a CCD camera and analyzed as mentioned above.

4.3.6 Total Internal Reflection Fluorescence Imaging

Total internal reflection fluorescence (TIRF) images where collected using an argon-ion laser (Ion Laser Technology) with a 514 nm output. The PSLBs were imaged by incorporating 1 mol % Rhodamine B-capped-DOPE. TIRF imaging were collected using a modified Olympus microscope[5] with a 4× objective (Optics for Research). Acquisition of the image was accomplished using a CCD camera (Roper Scientific, 512 x 512 pixels). Images were then taken without the microscope and objective at the same distances as the lens-less SHG images.

4.4 Results and Discussion

4.4.1 Analysis of Lens-less SHG Imaging

SSHG images of an SBN-lipid membrane patterned with the 1951 USAF resolution test target collected without an objective lens measured at 5 distances ranging from 7.6 cm to 40 cm are shown in Figure 4.4 (A-E). The SH signal generated in these images are from the SBN that has preferentially intercalated into the DOPC bilayer, allowing the pattern to be visualized with negligible signal from the regions void of lipids. For comparison, Figure 4.4 (F) shows a white light image of the positive USAF test target line-width groups, 0 and 1, used to pattern the lipid bilayer. In this experiment elements 3-6 of group 0 were imaged because their line-widths are in the range of spot sizes used in chemical and biological microarrays (280 μm to 397 μm), while the smaller elements of group 1 were imaged to demonstrate the limits of the current lens-less SSHG imaging system before diffraction effects are seen (140 μm to 250 μm). Figure 4.4 (A) shows that all elements of both group 0 and group 1 are discernible at an object to detector distance of 7.6 cm. As the distance between the object and detector increases, the line-widths become less discernible due to increased transverse spreading of the image widths and increased curvature in the wave-front, especially for the smaller line-widths of group 1.

To confirm that the nonuniformity seen in the lens-less SSHG images shown in Figure 4.4 is not a result of the lens-less imaging system, an image of the group 0 elements (397 μm, 355 μm, and 314 μm) was taken using a convex lens to reconstruct the image (shown in Figure 4.5). It is apparent in Figure 4.5 that even when a lens is employed the line-widths are nonuniform in nature, which suggests the nonuniformity

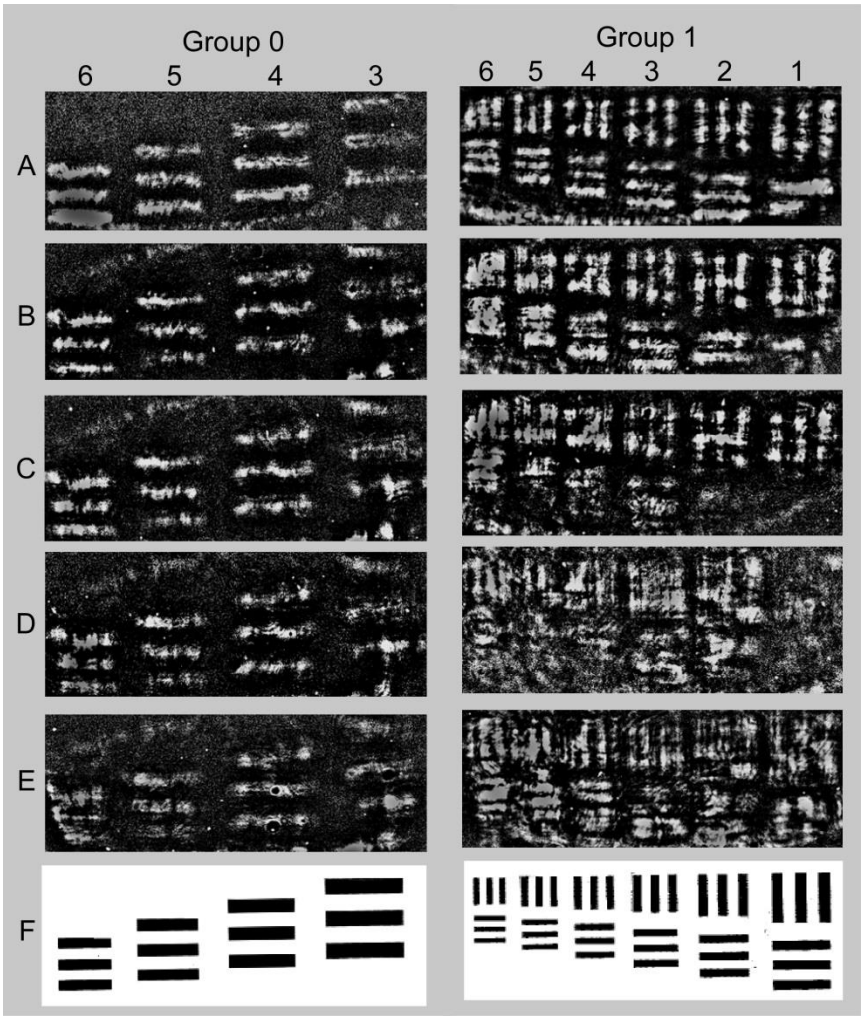

Figure 4.4. Lens-less SSHG images of a patterned DOPC bilayer containing SBN using the USAF test target group 0 horizontal lines only (elements 3 through 6) on the left and group 1 horizontal and vertical lines (elements 1 through 6) on the right corresponding to line-widths of 397 μm, 355 μm, 314 μm, 280 μm, 250μm, 223 μm, 198.5 μm, 176.5 μm, 157.5 μm and 140.5 μm, respectively. Images were recorded at detector-sample distances of (A) 7.6 cm, (B) 15.2 cm, (C) 22.9 cm, (D) 30 cm, and (E) 40 cm. A white light image of group 0 and group 1 of the USAF test target is shown in (F).

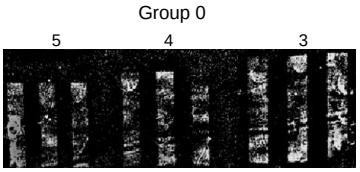

Figure 4.5. SSHG images taken using a convex lens of a patterned DOPC bilayer containing SBN using the USAF test target group 0 vertical lines only (elements 3 through 5) corresponding to line-widths of 397 μm, 355 μm, and 314 μm.

seen in the images is not a by-product of the imaging system, but rather an inherent artifact of the objects themselves. The nonuniformity of the line-widths is most likely due to the nonuniform binding of SBN to the DOPC lipid bilayer and the chemical etching process.

Each line from the pattern can be taken as a separate object that generates its own SH signal and is described by its own propagating field. The intensity distribution imaged for each line-width can then be analyzed separately to determine the dependence of the imaged width on the propagation distance using equation 4.5. The image width taken as the full width at half maximum (FWHM) of the peak intensity was determined by fitting intensity profiles for the short axis of the line-widths, where the intensity was averaged along the long axis, to a Gaussian distribution (equation 4.8) for four representative line-widths (397 μm, 355 μm, 280 μm, and 196 μm).

$$y = y_0 + A\exp\left[-\left(\frac{(x-b)^2}{2\sigma^2}\right)\right]. \tag{4.8}$$

In the above equation y_0 is the baseline offset from zero, A is the amplitude at the peak center, b is the position (x) at maximum intensity or the peak center, and σ^2 is the variance from the x value at maximum intensity. The FWHM (2.35σ) was determined for the four elements at each distance. The measured FWHM for each of the four representative elements of the test pattern was plotted for each distance and the results are shown in Figure 4.6.

The theoretical imaged beam width for each element was calculated from equation 4.5 for distances up to 50 cm where w_0 was taken as the line-width from the test

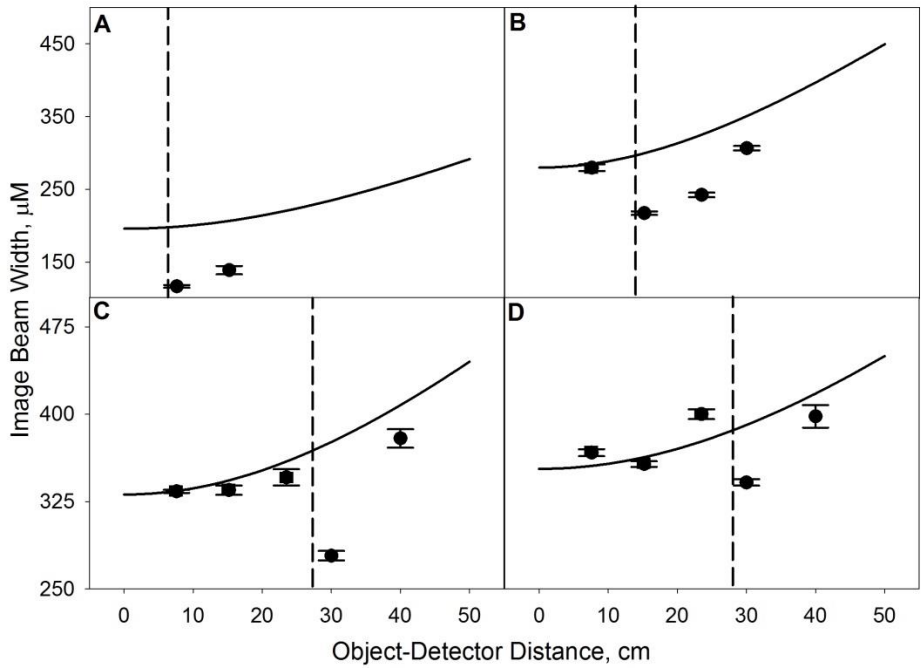

Figure 4.6. Image beam width as a function of distance for the line-widths of (A) 196µm, (B) 280µm, (C) 355, and (D) 397µm. Error bars represent the error between the FWHM from the three peaks generated for each element. The dashed line indicates the distance at which diffraction occurs and the solid lines indicate the fit to Gaussian beam propagation theory according to equation 4.9.

target and then compared to the experimentally-determined image widths obtained from analysis of the images in Figure 4.4. The experimental and theoretical image widths follow the same general exponential increase with increasing distance; however, the experimentally determined image widths were seen to increase more rapidly with increasing distance. In order to determine how much faster the image widths were spreading with distance, the data points where diffraction was not observed (the 7 data points to the left of the dashed line in Figure 4.6) were then globally fit to the following equation with the resulting fit shown in Figure 4.6,

$$w(z) = w_0\sqrt{1+\left(\frac{\lambda z\alpha}{\pi w_0^{\,2}}\right)^2}, \tag{4.9}$$

where w_0 was determined by extrapolating the fit to *z=0*, and α represents the parameter which accounts for the more rapid spreading with distance. The experimentally determined image widths were shown to increase 2.33 times faster than that predicted by Gaussian beam propagation theory. This more rapid increase in image width with increasing distance most likely comes from the imperfect assumption that the incoming light waves are perfectly collimated plane-waves. Although much care was taken to highly collimate the incoming light beams, it is inevitable that some distortion of the wave-front of the incoming beams will exist due to the inherent slightly curved wave-fronts from the incident laser and the disturbances in the beam parameters $R(z)$ and $w(z)$ caused by the lenses used to resize and collimate the incoming beams.[23] Despite the more rapid spreading of the image widths seen here, the data fit well to equation 4.9 for each sized line-width at close distances. An interesting observation is then seen for all sized

line-widths, a sudden decrease in image width occurs and the data seem to no longer follow the fit predicted by Gaussian beam propagation theory. Since diffraction would cause a decrease in the expected image width,[25] the images were analyzed according to classic diffraction theory to determine whether or not this drop in image width coincided with diffraction effects. The intensity profiles were analyzed according to classic Fraunhofer diffraction theory[25] in one dimension using the following:

$$I = I_0 \left(\frac{\sin \beta}{\beta} \right)^2 \tag{4.10}$$

$$\beta = \frac{1}{2} kb \sin \theta \tag{4.11}$$

where I is the intensity, k is the wavenumber, b is the short axis width of the bar and θ is the angle of the diffracted ray. Fraunhofer diffraction for a single slit was used as the object size and separation between adjacent linewidths is much larger than the wavelength of light used here and the emitted light source is a collimated plane-wave.[25] The Fraunhofer diffraction model was then compared to the Gaussian beam propagation model in examining the image width as a function of distance, results are shown in Figure 4.7.

Using the concordance test, the distance at which the Fraunhofer diffraction model was found to fit best as compared to the Gaussian beam propagation model coincided with the distance at which the sudden decrease in image width occurred for each sized line-width. The dashed line in Figure 4.6 indicates where the Fraunhofer diffraction model was found to fit best compared to the Gaussian beam propagation model. These results are consistent with the predictions that when diffraction occurs the

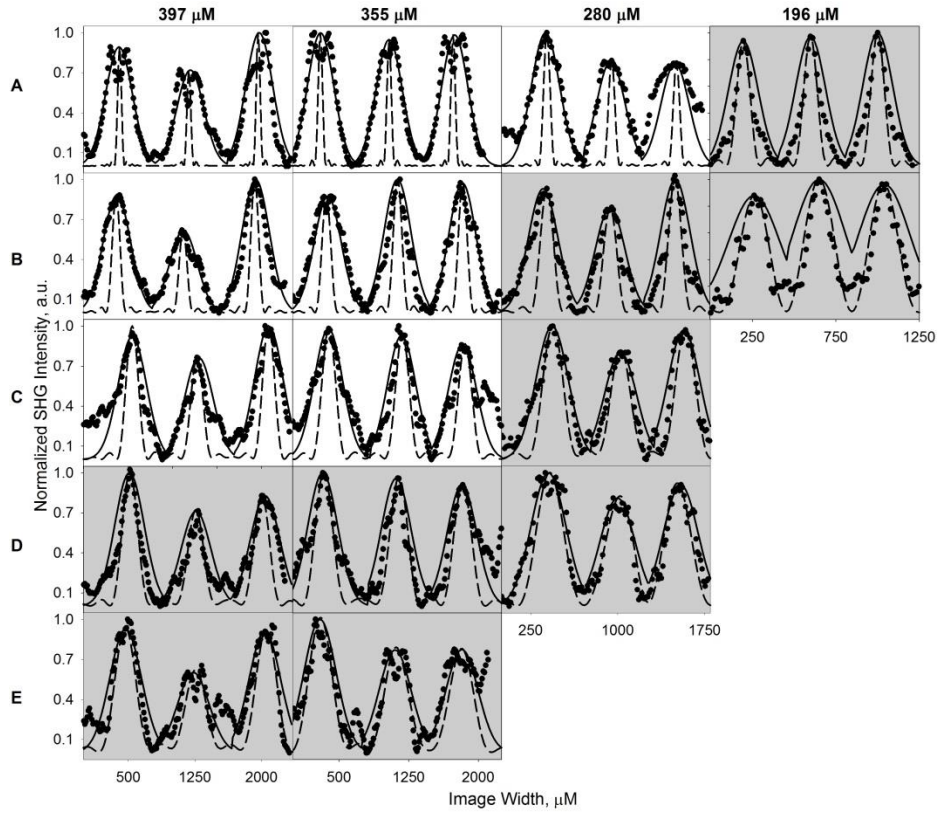

Figure 4.7. Gaussian beam propagation fit (solid lines) and Fraunhofer diffraction fit (dashed lines) to the intensity profiles for line-widths of 397 μm, 355 μm, 280 μm, and 196 μm at detector-sample distances of (A) 7.6 cm, (B) 15.2 cm, (C) 22.9 cm, (D) 30 cm and (E) 40 cm. The gray graphs represent where the Fraunhofer diffraction fit best to the data.

image width is much smaller than expected and begins to change linearly with distance. Theoretically, the distance at which diffraction occurs is the confocal distance. However, even after taking into account the 2.33 times more rapid spreading of the image widths seen here, the calculated confocal distance using equation 4.7 of roughly 80 cm, 64 cm, 39 cm, and 19 cm for the line-widths of 397 μm, 355 μm, 280 μm, and 196 μm, respectively, is still ~2.5 times longer than where diffraction is visible in our data. This discrepancy can be explained in terms of the degree of curvature of the wave-front. Calculating the radius of curvature from equation 4.6 and subsequently the degree of curvature at the expected confocal distance the wave-front is found to have a degree of curvature of ~38° for each sized line-width; however, the distance at which diffraction is apparent in our data has the degree of curvature of between ~19° to 20°. This suggests that although theoretically diffraction should not occur until the wave-front has curved 38°, lens-less imaging is much more sensitive to the curvature of the wave-front and diffraction is obvious when there is only a slight deviation from a planar wave-front. Despite this lower threshold for the curvature of the wave-front, the similar limit of degree of curvature (~20°) seen to produce diffraction effects for all sized line-widths is consistent with the predictions of Gaussian beam propagation in which diffraction effects are observed at a much closer distance for smaller line-widths as compared to larger line-widths. This observation is due to the more rapid transformation of the wave-front from planar to spherical for smaller objects and is evident in Figure 4.7.

4.4.2 UV Back Illumination Imaging Analysis

In order to further verify that the lens-less SHG images shown in Figure 4.4 result from the coherent plane-wave nature of the emitted light, lens-less transmission images of the USAF negative pattern (shown in Figure 4.8) were collected using an incoherent UV light source to back illuminate the sample. As expected these images had visible diffraction even at the closest distance of 7.6 cm for both group 1 and group 0 elements. No discernible image is obtained at distances greater than 22.9 cm for group 0 and group 1, in stark contrast to the SSHG images shown in Figure 4.4. Additionally, the background was much brighter due the diffraction and there was rapid transverse spreading of the beam, making the line-widths difficult to differentiate. Although this incoherent UV back illuminated control demonstrates diffraction was not seen in the SHG images at close distances, a more appropriate control to demonstrate the difference between coherent and incoherent imaging is to use an emissive incoherent light source such as fluorescence imaging to compare to the emissive coherent SHG imaging.

4.4.3 Analysis of Fluorescence Lens-less Imaging

Lens-less fluorescence imaging was used to image a 1 mol% Rhodamine labeled USAF patterned DOPC lipid bilayer at the various distances. As opposed to SHG, fluorescence is an incoherent process in which scattering and diffraction of the generated electromagnetic waves distort the wave-front at very short distances such that the amplitude and phase of the beam vary randomly with respect to time and position instantaneously. As a result, the coherence length is significantly shorter, causing considerable divergence of the beam and consequently, distortion of the image, making it

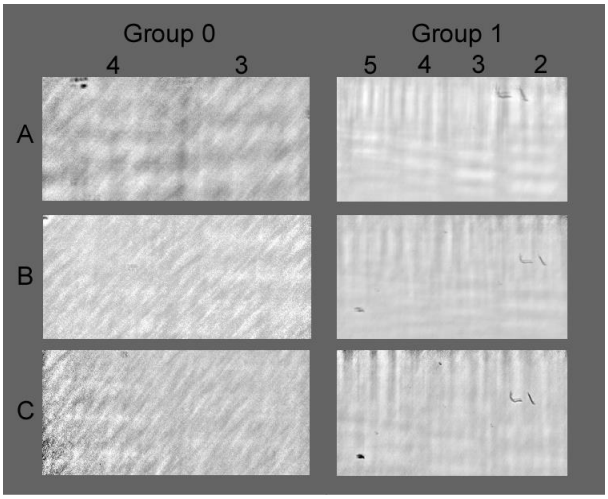

Figure 4.8. UV back illuminated lens-less imaging of the USAF test target group 0 horizontal lines only (elements 3 and 4) on the left and group 1 horizontal and vertical lines (elements 2 through 5) on the right corresponding to line-widths of 397 μm, 355 μm, 223 μm, 198.5 μm, 176.5 μm, and 157.5 μm, respectively. Images were recorded at detector-sample distances of (A) 7.6 cm, (B) 15.2 cm, and (C) 22.9 cm.

impossible to resolve an image without the use of a lens system. A 4x objective lens in combination with a CCD was first used to verify that the CCD was aligned and the pattern was in the detection area; the resulting discernible image is shown in Figure 4.9 (A). Once the objective was removed, no image was discernible even at the closest distance (7.6 cm) as shown in Figure 4.9 (B). These results demonstrate that the transverse spreading and radial wave-front caused by the incoherent nature of fluorescence necessitates the use of an objective lens to resolve an image, and therefore confirms that only a collimated, coherent plane-wave source has the ability to image without a lens system. Therefore, even though the experimentally determined confocal distance of the SSHG lens-less images deviates from the theoretical confocal distance due to the slightly curved wave-fronts of the incoming beams, the SH emission is still significantly planar and collimated, giving SSHG the ability to image without a lens system.

The image spreading and ultimately diffraction seen at increasing distances for this SSHGI system is not merely classic diffraction, but is a consequence of Gaussian beam propagation, which predicts that with increasing distance the beam will become less collimated, less coherent, and less planar, causing increased transverse spreading or divergence of the beam and diffraction. Despite the more rapid increase in image width and shorter confocal distance observed in the lens-less SSHG imaging due to the nonideal plane-wave nature of the incoming beams, the image data presented in Figure 4.4 and analyzed in Figure 4.6 are consistent with the general predictions of optical beam propagation theory for the behavior of a Gaussian plane-wave propagating through space. This not only confirms that surface SHG generates a near-collimated, coherent plane-

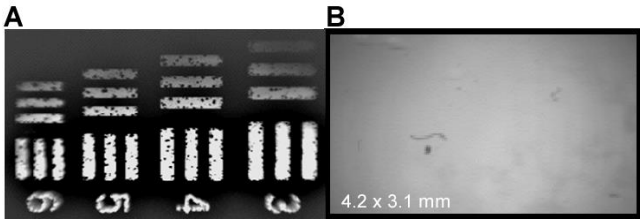

Figure 4.9. Fluorescence imaging of SBN binding to a Rh-DOPC bilayer. (A) Fluorescence image of group 1 elements 3 through 6 of the USAF test target using a 4x objective lens. (B) Lens-less fluorescence image at 7.6 cm object-image shows no visible image.

wave at relatively long distances, but also confirms that lens-less SSHG imaging is possible as a result of the collimated, coherent plane-wave nature of the process, which minimizes transverse spreading and diffraction effects. It is important to keep in mind that diffraction is only avoided if the object size is large compared to the wavelength and the object-image distance is shorter than the confocal distance.

4.5 Summary

The work presented in this chapter has demonstrated the capabilities of SSHG imaging based on its long coherence length and plane-wave nature to directly image the intensity distribution of a patterned SBN-lipid bilayer without a lens system. The SHG beam propagated through space according to Gaussian beam propagation theory, which was used to analyze the image widths as a function of distance. The distance at which lens-less SSHG imaging was able to resolve images without diffraction effects was shown to be dependent on the object size. Even though diffraction is readily observed at even the closest object-detector distance (7.6 cm) for line-widths of 196 μm, there is no observable diffraction for line-widths of 223 μm at this close distance and line-widths of 397 μm did not show diffraction until ~ 30 cm. Although the experimentally determined confocal distance deviated from the theoretical confocal distance, the deviation was consistent for all object sizes, indicating that the discrepancy was due to the incoming beams having nonideal planar wave-fronts. Lens-less SSHG imaging was also seen to be more sensitive to the curvature of the wave-front, producing diffraction effects at a degree of curvature of only 20°. However, the complete inability of fluorescence imaging, an incoherent emissive process, to resolve an image without an objective lens

demonstrated that the SH emission was still significantly planar and coherent and that it was this property that permits SSHG lens-less imaging without a lens system. Therefore, the inherent properties (highly collimated, coherent plane-wave) of SSHG allow simple, direct amplitude distribution imaging without a lens system. Although it is true that higher resolution images can be produced when a single lens is used, the noticeable differences between the lens-less coherent SSHG imaging and the lens-less incoherent fluorescence imaging shown here emphasize the effects the wave-front of the beam have on image formation. The initial object size and detector-sample distance are also shown to affect imaging. Additionally, being able to image without a lens reduces optical aberrations, improves the overall photon collection efficiency and increases the detection area, which can be used to increase throughput. In the field of biosensors and medical diagnostics where only relative intensities are being used these advantages could be extremely beneficial, as larger arrays could be directly imaged and analyzed simultaneously.

4.6 References

(1) Shen, Y. R. *Annu. Rev. Mater. Sci.* **1986**, *16*, 69-86.

(2) Hellwarth, R.; Christensen, P. *Opt. Commun.* **1974**, *12*, 318-322.

(3) Motreff, A.; Raffy, G.; Del Guerzo, A.; Belin, C.; Dussauze, M.; Rodriguez, V.; Vincent, J.-M. *Chem. Commun.* **2010**, *46*, 2617-2619.

(4) Iwamoto, M.; Manaka, T. *Thin Solid Films* **2011**, *519*, 961-963.

(5) Kriech, M. A.; Conboy, J. C. *J. Am. Chem. Soc.* **2005**, *127*, 2834-2835.

(6) Campagnola, P. *Anal. Chem.* **2011**, *83*, 3224-3231.

(7) Liao, C.-S.; Zhuo, Z.-Y.; Yu, J.-Y.; Tzeng, Y.-Y.; Chu, S.-W.; Yu, S.-F.; Chao, P.-H. G. *Appl. Phys. Lett.* **2011**, *98*, 153703/153701-153703/153703.

(8) Bouevitch, O.; Lewis, A.; Pinevsky, I.; Wuskell, J. P.; Loew, L. M. *Biophys. J.* **1993**, *65*, 672-679.

(9) Ben-Oren, I.; Peleg, G.; Lewis, A.; Minke, B.; Loew, L. *Biophys. J.* **1996**, *71*, 1616-1620.

(10) Moreaux, L.; Sandre, O.; Blanchard-Desce, M.; Mertz, J. *Opt Lett* **2000**, *25*, 320-322.

(11) Srivastava, A.; Eisenthal, K. B. *Chem. Phys. Lett.* **1998**, *292*, 345-351.

(12) Yan, E. C. Y.; Eisenthal, K. B. *Biophys. J.* **2000**, *79*, 898-903.

(13) Peleg, G.; Lewis, A.; Linial, M.; Loew, L. M. *Proc. Natl. Acad. Sci. U. S. A.* **1999**, *96*, 6700-6704.

(14) Nguyen, T. T.; Conboy, J. C. *Anal. Chem.* **2011**, *83*, 5979-5988.

(15) Gabor, D. *Nature* **1948**, *161*, 777.

(16) Schwarz, A.; Weiss, A.; Fixler, D.; Zalevsky, Z.; Mico, V.; Garcia, J. *Opt. Commun.* **2009**, *282*, 2780-2786.

(17) Goldsmith, P. F. *Quasioptical Systems: Gaussian Beam Quasioptical Propagation and Applications*; IEEE Press, 1998.

(18) Siegman, A. E. *An Introduction to Lasers and Masers*; McGraw Hill, 1971.

(19) Dick, B.; Gierulski, A.; Marowsky, G.; Reider, G. A. *Appl. Phys. B Lasers Opt.* **1985**, *38*, 107-116.

(20) Steinberg, R. G. W. A. M. In *Access Science*, McGraw Hill: 2008.

(21) Tyras, G. *Radiation an Propagation of Electromagnetic Waves*; Academic Press: New York, 1969.

(22) Shen, Y. R. *The Principles of Nonlinear Optics*; John Wiley & Sons, Inc., 1984.

(23) Kogelnik, H.; Li, T. *Appl Opt* **1966**, *5*, 1550-1567.

(24) Masina, R.; Zhu, X. D.; Parikh, A. N.; Bruch, R.; Landry, J. P. *Proc. SPIE-Int. Soc. Opt. Eng.* **2006**, *6095*, 60950T/60951-60950T/60959.

(25) Fowles, G. R. *Introduction to Modern Optics*; Second ed.; Holt, Rinehart and Winston, Inc., 1968.

CHAPTER 5

SECOND HARMONIC CORRELATION SPECTROSCOPY

Reprinted (adapted) with permission from Sly, K.L. and Conboy, J.C. *Anal. Chem.*, **2014**, *submitted.*

5.1 Introduction

In the previous chapters, SH spectroscopy was shown to have the ability to detect proteins and small molecules at the surface with incredible sensitivity and specificity without the use of an external label. In Chapter 4 it was demonstrated that the coherent property of surface SHG allowed imaging of a small molecule intercalating into a lipid bilayer without using a lens. More importantly, Chapter 4 provided a detailed analysis of the coherence length and properties of counter propagating SH spectroscopy. Despite the high sensitivity of SHG seen in the previous chapters, there were bothersome shortcomings in the traditional method of data collection. Specifically, the collection of binding isotherms required an extremely long acquisition time and the analysis of such binding isotherms neglected the dependence of the binding kinetics on bulk protein concentration. These obstacles can be easily overcome by coupling the proven surface specific and sensitive SH spectroscopy technique with coherent correlation spectroscopy for the direct measurement of surface biomolecular kinetics. In this chapter the general

principles and important properties of the second harmonic correlation spectroscopy (SHCS) process are discussed.

Correlation spectroscopy (CS) is a well-known statistical analysis method capable of extracting dynamic events within a system by correlating a temporally measured property of the system. CS has been used to extract correlated dynamics in a variety of methods such as neutron scattering,[1] dynamic light scattering,[2-5] fluorescence spectroscopy,[6-10] and Raman spectroscopy.[11,12] More recently coherent x-ray spectroscopy[13-16] and nonlinear spectroscopic methods[17,18] have been coupled with correlation analysis, including second harmonic correlation spectroscopy (SHCS). SHCS has been used as a method to determine the diffusion coefficient of aggregate dye molecules at a surface[17] and long chain para substituted amphiphiles.[19]

The theoretical groundwork for all these correlation spectroscopic methods was first presented by Van Hove in 1954 in his studies of the coherent scattering of neutrons.[1] Van Hove's time-dependent correlation function demonstrated that the average time variation of the density distribution of a system could be used to determine the correlated dynamic time evolution of the particles of the system.[1] This time-dependent correlation function, based on the expression of the system in terms of a simple Poisson density distribution of measured intensities from the scattered particles within the system, only requires that (1) the system or state does not change during the scattering process (is ergodic) and (2) the mean intensity measured over time remains constant (stationary).[1] These criteria are easily satisfied for any photon process used to measure a system in steady-state equilibrium. It is possible to examine a system that is not stationary or ergodic using correlation spectroscopy; however, distortions will be seen in the

correlation function and special considerations must be taken for a proper analysis.

Nearly a decade after Van Hove introduced correlation spectroscopy, Pecora combined the developed correlation function with Brillouin's theory of scattered light to create photon correlation theory or what is known today as dynamic light scattering (DLS).[2] Pecora has since written extensively on the theory and analysis of photon correlation spectroscopy, including a detailed presentation of various signal to noise parameters and ideal instrumentation and system requirements.[3] One of the biggest obstacles in obtaining meaningful correlation data in DLS has been low signal from weak scatterers.[3] To overcome this limitation, an increase in the detected power density is usually made through increasing the solute concentration or laser intensity. However, decreasing the scattering angle or illumination area, which will decrease the measured signal, increases the spatial coherence (coherence area) and the signal-to-noise (S/N) of the correlation data.[3,4] As such, there is a trade-off between the number of molecules in the illumination area and the size of the illumination area in order to obtain correlation data with low noise while still having fairly large measured signal. Most DLS studies have illustrated the importance of increasing the detected signal and maintaining good spatial coherence, whether it be from increasing the solute concentration and decreasing the scattering angle by using a pinhole before the detector or decreasing the illumination area and increasing the intensity of the excitation source.[3,4] Using Pecora's established experimental framework for photon correlation spectroscopy, DLS has been used to obtain the dynamic time constants for translational,[20,21] rotational,[22] and intramolecular diffusion of macromolecules,[23,24] as well as provide information on equilibrium critical phenomena of fluid systems.[2,25]

Even though DLS is well-established, today people first think of fluorescence correlation spectroscopy (FCS) when speaking of correlation spectroscopy. Although many significant advances have also been seen in FCS, it wasn't until several years after the development of DLS when Magde, Elson and Webb first demonstrated Van Hove's correlation analysis could also be used to examine the instantaneous fluctuations in fluorescence intensity and used to determine both the diffusion coefficient and binding kinetics of the reversible binding of ethidium bromide to DNA.[26] Several groups have since made extraordinary advances in developing FCS. Most notably, the detailed statistical analysis of FCS by Koppel, Saffarian and Elson,[27,28] the examination of multiple parameters and their contribution to the correlation data by Thompson and coworkers,[29,30] and many other studies which have shown the diversity of dynamic constants that can be measured using FCS. FCS has provided a means of obtaining the rotational and translational diffusion coefficients of species in bulk solution,[31] lateral diffusion coefficients of biomolecules attached to planar supported lipid bilayers (PSLB),[32,33] and the binding kinetics of fluorescently labeled biomolecules at surface.[10,34] As in DLS, the temporal fluctuations in the signal are measured and used to obtain the correlated dynamic events occurring within the observation volume. However, an important fundamental difference between FCS and DLS makes the ideal experimental parameters and application of correlation spectroscopy for these two methods very different.

DLS is a coherent process where the signal intensity from individual photons produces stationary interference such that the spontaneous fluctuations caused by individual photon positional changes can be additive (constructive interference) or

subtractive (deconstructive interference) to the measured average density distribution.[4] Experimentally, the stationary interference of the scatterers in DLS makes having a higher concentration of molecules advantageous for obtaining higher S/N in the correlation data.[3,4] With a higher number of molecules in the illumination area, there will be an increased probability of interference, causing a greater additive or subtractive effect seen from the fluctuations and leading to higher S/N in the correlation data.[3] Additionally, optimal S/N in the correlation data will be obtained if the illumination area or the detection area is spatially coherent and equal to the coherence area. For DLS this area is relatively small (less than a few microns), meaning that although it is advantageous to increase the photon flux the detection area much be kept small to have spatial coherence and high S/N of the correlation data. The spatial coherence of the excitation source and output signal of a system drastically affects the optimal experimental conditions to obtain the best correlation data.

Recently, the role spatial coherence plays on the S/N of the correlation data has been detailed in several studies of x-ray correlation spectroscopy (XPCS) where it was shown that having partial coherence or complete incoherence drastically dampens the correlation data.[13,16,35,36] XPCS is analogous to DLS, as it too uses a coherent excitation source and measures the instantaneous complex interference of photons. Similar to DLS, it has been shown that better S/N of the correlation data is observed when the coherence area (spatial coherence) is matched to the scattering volume (one coherence area) and when the photon flux is large.[36] Again, there is a trade-off between the number of photons in the scattering volume and degree of spatial coherence (the number of coherence areas), with the optimum condition satisfied by having the maximum number

of photons in a single coherence area.

The main difference between DLS and XPCS is the incident wavelength. Although both DLS and XPCS use spatially and temporally coherent excitation sources, the small wavelengths in XPCS as compared to the larger visible wavelengths of DLS generate an signal with longer temporal coherence (coherence length), allowing the detector-sample distance to be longer before diffraction occurs and there is loss of coherence. The spatial coherence (coherence area) is also extremely small in XPCS (only a few microns) which requires the detection area to be small, which is usually achieved by sending the scattered light through a pinhole aperture. The smaller wavelengths in XPCS also allow dynamics of much smaller length scales down to interatomic spacing to be probed.[13,16,36] These differences obviously will dictate the most suitable experimental parameters (i.e., detector-sample distance and the size of the illumination and detection area) and which systems to study using these coherent photon correlation spectroscopic (PCS) methods.

Compared to both DLS and XPCS, the incoherent method FCS is significantly different. FCS does not measure the stationary interference of photons and the lack of coherence necessitates a very different conclusion regarding the ideal number of molecules present in the observation volume. FCS measures the total fluorescence in each dwell and the dwell time of individual fluorophores within the observation volume.[37] If a large number of fluorescent molecules were present then the probability of each molecule that enters the observation area fluorescing is small and the probability of finding the same molecule in two consecutive dwells becomes even smaller.[27,37] Koppel demonstrated that the incoherent nature of FCS means that the S/N of the FCS correlation

data is dependent on the ratio of photocounts ($\langle n \rangle$) per number of molecules to (N) correlation time (T), $S/N \propto \langle n \rangle \mathrm{T}^{1/2}/N$, as opposed to the ratio of photocounts per number of coherence areas (N_c) to correlation time, $S/N \propto \langle n \rangle \mathrm{T}^{1/2}/\mathrm{N}_c$, seen in DLS and XPCS. Accordingly, the observation volume and the detection area should ideally be kept as small as possible with as few molecules as possible to obtain better S/N of the correlation data in FCS.[27,28] This is much different from the desired large photon flux in a single coherence area in DLS and XPCS. The comparison of these photon correlation methods illustrates the importance of coherence, the source of the intensity fluctuations (ie. stationary interference or individual fluorophores), and incident wavelength on the resulting S/N of the correlation data for DLS, XPCS and FCS.[3,4]

One extremely important conclusion to be drawn from the above comparison of DLS, XPCS, and FCS is that the coherence of the incident light and output signal plays a significant role on the experimental parameters that lead to optimal S/N in the correlation data. For example, if the intensity fluctuations arise from the stationary interference of photons (as in DLS and XPCS) then increased spatial coherence (coherence area) and temporal coherence (coherence length) of the output signal would allow the illumination area to be relatively large with a large photon flux. This would be an extremely advantages experimental parameter as it would be much simpler to keep the illumination area and detection area equal to only one coherence area (or spatially coherent) over a long distance before coherence is lost. One such technique that exhibits an output with large spatial and temporal coherence is SH spectroscopy. SH spectroscopy is an emissive coherent process with a much more spatially and temporally coherent output compared to DLS or XPCS. The authors have previously shown that the coherence area of the output

is essentially the illuminated area of the sample as long as the incident beams are spatially and temporally coherent.[38] In Chapter 4, the coherence length (temporal coherence) of SH spectroscopy was found to be rather long with a linear relationship to the square of the spatially coherent illumination area, meaning the coherence length increases with increasing illumination area.[38] The incident beams in SHG have a narrow frequency distribution, such that when they are spatially and temporally overlapped from opposing directions, produce an extremely spatially and temporally coherent SH output, much more so than DLS or XPCS, making is possible to have a large spatially coherent illumination and detection area. The large spatial coherence eliminates the need for a pinhole aperture at the detector used to limit the detection area to one coherence area. This is drastically different from incoherent FCS or coherent DLS and XPCS.[3,4]

Another advantage of SHCS is its nonlinear nature and directional output allow simple heterodyne mixing of the SH fluctuations using the SH mean intensity as a local oscillator, which can increase the S/N of the correlation data.[4] This type of heterodyne mixing has been used in XPCS and shown to increase the S/N of the correlation data.[35,36] Heterodyne mixing has also been used in DLS; however, the source of the local oscillator is typically the incident excitation source that is recombined with the signal from the scatterers.[4] An added benefit of heterodyne mixing in SHCS is that there is a linear relationship between the SH heterodyned intensity and density of molecules comprising an intensity fluctuation. This linear relationship makes it much simpler to analyze the correlation data with the ability to use the already developed FCS correlation functions. Furthermore, having the SH mean intensity act as the local oscillator provides a simple and straightforward way to increase the S/N of the correlation data assuming the majority

of the noise is arising from the detection system shot noise and not from the excitation source and optics.[35,36] The advantages seen from heterodyning and a larger spatially and temporally coherent illumination area, along with the surface specificity and label-free nature of SHG, make SHCS an attractive alternative for the direct detection of the dynamics of surface biomolecular interactions.

SHCS has previously been used to determine the translational and rotational coefficients of dye molecules and hydrocarbon chain substituted amphilies;[17,19,39,40] however, its use for investigating surface binding kinetics has only just been explored. Chapter 6 and Chapter 7 are the first examples to examine the ability of SHCS to determine the binding kinetics of a monovalent interaction between the small molecule SBN and a DOPC lipid bilayer[41] and the more complex interaction between the multivalent proteins cholera toxin b subunit (CTb) and peanut agglutinin (PnA) with monosialotetrahexosylganglioside (GM_1) doped DOPC bilayers. These studies illustrate the bothersome shortcomings of traditional adsorption isotherms combined with desorption experiments to obtain surface binding kinetics. Specifically, the collection of adsorption isotherms at low concentrations requires an extremely long acquisition time to reach true steady-state equilibrium and as such are often limited by mass transport. These obstacles were easily overcome by coupling the surface specificity and sensitivity of SHG with correlation spectroscopy for the direct measurement of surface biomolecular kinetics.[41] This chapter is designed to expand on the theory of SHCS used in the studies presented in Chapters 6 and 7 and to thoroughly describe the correlation function for determining surface binding dynamics of a reversible biomolecular reaction. Important properties of SHG, such as coherence and heterodyne optical mixing, which play a

significant role on the measured S/N of the correlation data will be discussed in detail. Additionally, practical experimental considerations including collection time and illumination/detection area will be examined. The sample system used here, CTb binding to a GM_1 doped DOPC lipid bilayer, provides a simple means to investigate the dependence of the S/N of the correlation data on various experimental parameters.

5.2 General Principles of SHCS

The most fundamental approach used to evaluate all correlation methods stems from modern statistical mechanics and the many-body theory, which describes the collective behavior of a large assembly of interacting particles.[4] For any time dependent process within a given system, the measurement of a time-dependent real variable can be described by a simple probability density distribution where the instantaneous fluctuations in the measured intensity would fall between $I + \sqrt{I}$ and $I - \sqrt{I}$, giving a Poisson distribution in measured intensity.[3,4] Similarly, the instantaneous fluctuations in the measured SH intensity exhibit a Poisson probability density distribution about the SH mean intensity as shown in Figure 5.1. The data in Figure 5.1 were collected over time for every pulse of a 20 Hz Nd:YAG laser whose output was frequency doubled to produce 532 nm. The surface SHG produced at 266 nm was generated normal to the surface after the two incident beams from opposing directions interacted with a surface composed of 240 nM CTb binding to a GM_1 doped DOPC lipid bilayer. A histogram of the measure SH intensity was plotted as Figure 5.1B and using Poisson statistics the mean SH intensity of 1.246 was determined. Mathematical

The time required for a fluctuation in intensity to change from one extreme to

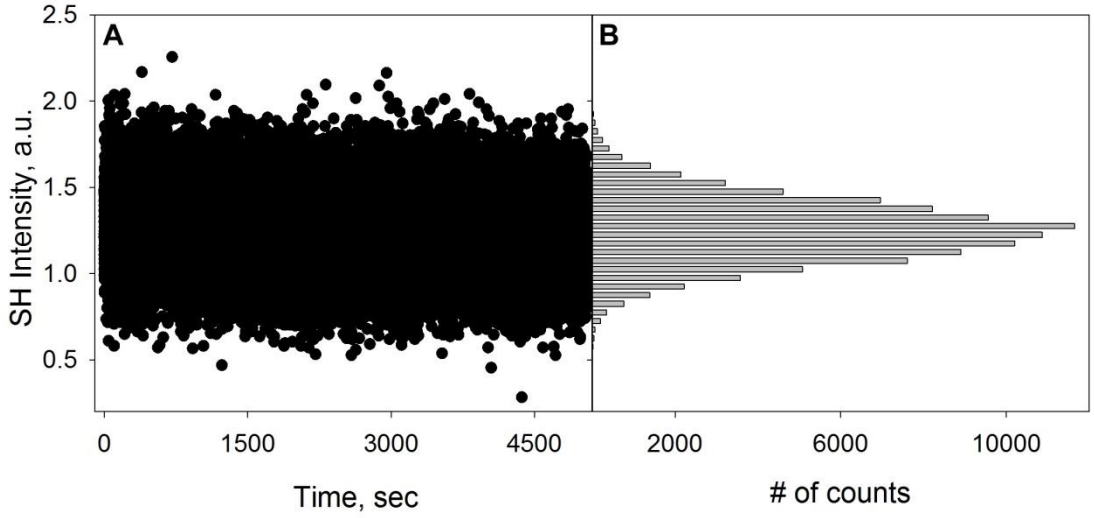

Figure 5.1. Probability density distribution of SH mean intensity. (A) Fluctuations in SH intensity measured for every pulse of a 20 Hz laser over time for the binding of 240 nM CTb to a GM_1 doped DOPC lipid bilayer and its (B) Poisson distribution in SH intensity with $\mu = 1.246$.

another is dependent on both the dynamic events within the system and the method of detection. For DLS the time required is related to the time it takes two molecules to move far enough apart to change the relative phase of the scattered light from 0 to π.[3] For FCS the fluctuations and time needed to fluctuate from one extreme to the other depends on the time it takes for a molecule to enter or leave the detection volume either by diffusion (lateral and translational) or adsorption and desorption.[30,37] The advantage of SHG having extreme surface specificity is it is possible to have the time it takes for the intensity to fluctuate between the extremes only depend on the time required for a molecule to adsorb or desorb from the surface.

An additional property of the intensity distribution of the fluctuations is that the distribution and ensemble average remain the same over the collection time, meaning the fluctuations are both stationary and ergodic.[4] For such a system, the time-dependent correlation function can be expressed as follows:[4]

$$G(\tau) = \lim_{T\to\infty} \frac{1}{T} \int_{-T/2}^{T/2} \delta SH(t+\tau)\delta SH(t)dt, \quad (5.1)$$

where $SH(t)$ is the measured SH intensity as a function of time and $SH(t+\tau)$ is the intensity of an individual spontaneous fluctuation after the time step equal to τ. The normalized correlation function can then simply be defined as,

$$G(\tau) = \frac{\langle \delta SH(t+\tau)\delta SH(t)\rangle}{\langle SH(t)\rangle^2}. \quad (5.2)$$

The angle brackets denote the ensemble average. Although the above correlation function is true for any stationary and ergodic system, its application and analysis largely depend on the detection method and dynamic processes occurring within the system. The following sections will describe the correlation function used in terms of detecting reversible biomolecular surface binding dynamics and then address some of the most

important factors of SHCS that influence the S/N of the correlation data.

5.3 Heterodyning

In DLS and XPCS the incident light from the laser is often used as a local oscillator to amplify the weak scattering, which allows detection of additional molecular dynamics that would otherwise not be measureable.[3,35] In a similar fashion, in SHCS the mean SH intensity can act as a local oscillator amplifying the weak fluctuations through heterodyning. The SH intensity can be described by the following expression,

$$I_{SHG} \propto \left| E_0^2 \chi_{ijk}^{(2)} \right|^2, \tag{5.3}$$

where E_0 is the incident electric field and $\chi_{ijk}^{(2)}$ is the nonlinear second order susceptibility tensor. As mentioned in Chapter 2 $\chi_{ijk}^{(2)}$ describes the interactions between the incident electric fields and the molecules at the surface, which makes it proportional to the amplitude of the SH generated electromagnetic wave, and can be expressed as follows,

$$\chi_{ijk}^{(2)} \propto N\langle \beta_{ijk} \rangle, \tag{5.4}$$

where $\langle \beta_{ijk} \rangle$ is the average ensemble molecular hyperpolarizability of the molecules at the surface. The SH generated electric field can be separated into a time-independent portion and time-dependent portion such that the generated field (E_{SH}) is a function of the density of molecules (q) and time (t), which can be expressed as,[36]

$$E_{SH}(q,t) = E_{\mu}(q) + E_{fluct}(q,t). \tag{5.5}$$

E_{μ} is the SH generated electric field from the population mean, making it the time-independent portion. The second term (E_{fluct}) is the time-dependent portion, which is defined as the fluctuation in the surface density of molecules with time.[36] The amplitude

of the SH generated electromagnetic wave from the population mean (E_μ) and those due to fluctuations associated with surface adsorption/desorption (E_{fluct}) can be described by,

$$E_\mu \propto N_\mu \langle \beta_{ijk} \rangle \tag{5.6}$$

$$E_{fluct} \propto N_{fluct} \langle \beta_{ijk} \rangle, \tag{5.7}$$

where N_μ and N_{fluct} represent the mean number of molecules and the number molecules giving rise to the fluctuations, respectively. E_μ and E_{fluct} interfere with each other, which results in heterodyning optical mixing where the time-independent E_μ acts as the local oscillator. The SH intensity generated when there is a local oscillator present is equal to the square of the sum or difference of the amplitudes of the electric fields of the signal and the local oscillator. As such, the SH heterodyned output intensity can be expressed as,

$$I \propto \left| N_\mu \langle \beta_{ijk} \rangle \pm N_{fluct} \langle \beta_{ijk} \rangle \right|^2$$

$$\propto \left(N_\mu \langle \beta_{ijk} \rangle \right)^2 + \left(N_{fluct} \langle \beta_{ijk} \rangle \right)^2 \pm N_\mu N_{fluct} \langle \beta_{ijk} \rangle^2. \tag{5.8}$$

In the cross term of the expanded expression there is a linear relationship between the overall SH intensity and N_{fluct}, which is enhanced by N_μ. Although the SH intensity is proportional to the square of the number density of molecules (Equations 5.3 and 5.4), a linear relationship between the SH intensity and N_{fluct} will always exist when heterodyne optical mixing is present. Given the linear relationship between the SH intensity and the number of molecules comprising an instantaneous fluctuation, the general correlation functions for linear spectroscopic methods can be applied to SHCS.

Optical heterodyning is very advantageous and provides a simple way to increase the measured intensity from individual fluctuations; the larger the mean SH intensity, the larger the measured fluctuations. Additionally, this also means that a larger mean

intensity or larger number of molecules will be more desirable in SHCS and provide more resolvable correlation data. This heterodyne effect has been extensively used with XPCS and shown to decrease the noise in the correlation data as the local oscillator intensity is increased.[4,35] It is important to note that the correlation function can be distorted by heterodyne optical mixing, such that the heterodyne correlation function is given as,[4]

$$G(\tau)_{hom} = C_1 G(\tau) + C_2^2 [G(\tau)]^2, \quad (5.9)$$

where C_1 and C_2 are constants related to the contributions from the fluctuation intensity and local oscillator intensity. The first term is the heterodyne term and second term is the intensity fluctuation term. If the local oscillator intensity is much larger than the intensity from the fluctuations, which is normally the case, the heterodyne term will dominate and the correlation function will just be $G(\tau)$ expressed in Equation 5.2.[4]

Experimentally, in SHCS heterodyning allows the number of molecules giving rise to the fluctuations, N_{fluct}, to be very small compared to the mean number of molecules while still being detectable (assuming most noise in the correlation data arises from detection system shot noise). Similarly in DLS and XPCS, when the local oscillator intensity is much greater than the intensity from the fluctuations, the fluctuations are still detectable and there is an improvement in the S/N of the correlation data.[3,35] This is drastically different from FCS, or other incoherent correlation spectroscopies, where the mean fluorescence signal can overwhelm the fluorescence intensity measured for an fluctuation if the number of molecules is too large.[27] This difference comes from the fact that the S/N of the correlation data is dependent on the spatial coherence of the detection area. In FCS this means the S/N is dependent on the number of molecules while in the

coherent processes of DLS, XPCS, and SHCS the S/N is dependent on the number of coherence areas sampled. The advantage of heterodyne mixing in SHCS is that it provides a rather simple way to increase the S/N of the correlation data by increasing the mean intensity, whether the intensity is increased by increasing the number of molecules within the illumination area or increasing the power of the excitation source.

5.4 Correlation Function for Surface Binding Kinetics

In order to extract any meaningful information from the correlation data, knowledge of the dynamic processes taking place within the observed system must be known. When investigating the reversible binding of a surface biomolecular interaction, the possible contributing dynamic processes include diffusion in and out of the detection area and adsorption and desorption of the molecules to the surface. In FCS, it has been repeatedly demonstrated that the instantaneous intensity fluctuations can indeed describe both of these dynamic events.[8,29,37] The correlation function is the sum of the contributions from surface-bound molecules [C] and molecules in solution [A], which is given by the following expression:

$$G(\tau) = G_{CC}(\tau) + G_{AA}(\tau) + G_{CA}(\tau) + G_{AC}(\tau) \quad (5.10)$$

where the last two terms can be neglected if the dynamic time constants from diffusion and surface binding are significantly different and rebinding of previously surface-bound molecules is negligible. Additionally, the surface specificity of SHCS allows the second term of Equation 5.10, $G_{AA}(\tau)$, to be neglected as it contains only contributions from molecules in solution. Additionally, the only term contributing to SHCS correlation data is $G_{CC}(\tau)$, which contains the contributions from surface-bound molecules, including

translational/rotational diffusion and chemical binding kinetics. The contributions from rotational and translational diffusion may be neglected if the rates occur at a different time scale than surface binding, similar to why the last two terms of Equation 5.10 can be neglected under the condition of differing time scale of events. The time scales of rotational/translation diffusion and surface binding can be separated where only contributions from surface binding are contributing if the time step (τ) is much slower than the rotational diffusion rate or the illumination area is sufficiently large that the translational diffusion rate would occur at a much longer time scale compared to the surface binding rates.[8,37] Given that the measured intensity fluctuations are only a result of dynamics that occur on the time scale greater than τ, only high repetition rate lasers (kHz and MHz) are able to detect the nanosecond time constants of the rotational diffusion of molecules.[33,42] Using a much longer time step of 50 ms from a 20 Hz laser (as used here and in the following chapters) these extremely fast rotational dynamics would be impossible to detect. Even large μm sized particles, whose rotational time constants are relatively slower (a few milliseconds in water)[40] are still too fast to be detected using a 50 ms time step.

The time scale of translational diffusion ($1/R_t$) is dependent on the diameter of the illumination area (d), such that $R_t = 4D/d^2$.[43] The translational diffusion of the surface-bound protein examined here is rather slow (a time scale of 10^6 s)[32] given the rather large illumination area (1 mm^2) used in this study, meaning that the translational diffusion would only be present at much longer time scales than the binding kinetics examined here which exhibit time constants on the order of a few seconds.[32] As such, it is highly improbable that the measured fluctuations in SH intensity on the time scale of a few

seconds with a time step of 50 ms and a 1 mm^2 illumination area are due to either translational or rotational diffusion. Under these conditions, the correlation data in SHCS are only a function of the surface binding kinetics. This situation is similar to the case in FCS where there are no diffusive contributions, which has been thoroughly developed by Starr and Thompson.[29]

As mentioned in the previous section there is a linear dependence of the SH intensity with respect to N from the instantaneous fluctuations due to the heterodyne optical mixing. As long as the heterodyned contribution is large there will be no distortion to the correlation function and it will resemble that of any linear ergodic system as discussed in the previous section.[4] The developed theory for FCS in the limit of no bulk diffusive contributions can then be applied to SHCS. The only condition being that the transport rate due to translational diffusion on the surface is much slower than the reaction rate of binding, which as mentioned earlier is almost always the case for large illumination areas.[8] Assuming a typical reversible biomolecular interaction where the average solution concentration of molecules, A, are in dynamic equilibrium with unoccupied surface binding sites with an average density B, and interact to produce an average density of surface-bound complexes, C, the reaction mechanism can be written as,

$$A + B \underset{k_{on}}{\overset{k_{off}}{\rightleftharpoons}} C, \tag{5.11}$$

with the adsorption and desorption rate given by k_{on} and k_{off}, respectively. The equilibrium binding constant, K_a, which describes the complete reaction, can then be determined using:

$$K_a = \frac{k_{on}}{k_{off}}. \tag{5.12}$$

When the observation area is very large and the reaction time constant is much less than the diffusion time constant, the dynamics are reaction rate limited and the correlation function will have the form of a first order exponential decay with the time constant equal to the reaction rate, R_r, written as,[34]

$$G(\tau) = G(0)\exp[-R_r\tau]. \tag{5.13}$$

Since the detectable change in the measured SH intensity is related to the change in bound molecules, the rate of reaction of Equation 5.13 can be described as,

$$R_r = k_{on}[A] + k_{off}, \tag{5.14}$$

where [A] is the concentration of the analyte in bulk solution. In SHCS, the number of molecules observed on the surface is always much greater than the number of molecules observed in solution with the number of molecules observed in solution equal to zero. Under these conditions the correlation function at time zero, $G(0)$, is described by,[34]

$$G(0) = \frac{1}{[C]R_r}, \tag{5.15}$$

where the concentration of bound complexes at the surfaces is represented by [C]. Knowing that Equation 5.12 is also equal to [C]/[A][B] and that the total surface density of binding sites is equal to the concentration of the bound and unbound sites, [C] + [B], Equation 5.15 can be more meaningfully expressed as,

$$G(0) = \frac{1}{N_s} \cdot \frac{1}{K_a[A]}, \tag{5.16}$$

where N_s is a normalization constant related to the surface density of adsorbed analyte. Combining Equations 5.13, 5.14, and 5.16 gives the normalized time dependent correlation function, $G(\tau)$, for a reversible biomolecular interaction that is reaction rate

limited and can be written as,[8]

$$G(\tau) = \frac{1}{N_s} \cdot \frac{k_{off}}{k_{on}[A]} \cdot exp\left[-\left(k_{on}[A] + k_{off}\right)\tau\right], \quad (5.17)$$

Using Equation 5.17, both the adsorption and desorption rate can be retrieved from the measured fluctuations in SH intensity for a single analyte concentration; however, to uncouple these parameters a separate measurement of the desorption rate is beneficial. Alternatively, if there are no concentration dependent binding kinetics, such as in a narrow range of [A], collecting correlation data for multiple bulk concentrations can also be used to provide the adsorption and desorption rate with decreased error.

5.5 Coherence

In DLS and XPCS the area of detection is often kept small; however, this is not to reduce the number of molecules in the detection area, as is the case in FCS.[3,4] Instead, the area is reduced in both DLS and XPCS to limit the detection area to one coherence area in order to satisfy the requirement that spatial coherence be maintained at the detector in order to maximize the fluctuations measured.[3] Each fluctuation in intensity takes place at a point in the scattered field and if another fluctuation occurs at a different point that is far away, outside one coherence area, the illumination area and detection area become spatially incoherent and it is much more difficult to correlate the fluctuations as they arise from multiple spatially incoherent intensity maxima and minima. Consider the case of DLS in which a scattering pattern from two molecules a distance of d apart produces an interference pattern. A maximum in intensity will occur every multiple of $\frac{\lambda}{d}\cos\theta$, where θ is the angle separating the two molecules.[3] If the detection area is larger than the angular separation between intensity maxima, then there will be many maxima and

minima in intensity (or multiple coherence areas) detected simultaneously. Consequently, the measured fluctuations are much less than those measured from a smaller detection area only containing one intensity maximum (or one coherence area).[3] This is primarily why it is necessary to reduce the portion of the sample which is illuminated or reduce the detection area in scattering processes that have small spatial coherence areas. In incoherent FCS, the illumination area is reduced to limit the number of molecules as fluctuations in intensity are the sum of many independent fluorophores each essentially representing its own coherence area. As such, smaller illumination areas will have fewer coherence areas (or fluorophores), resulting in improved S/N of the correlation data.[28] Although there is a need to maintain the detection system such that only one coherence area is sampled for both FCS and DLS, the parameter that determines the optimal size of the illumination or detection area is quite different. The single most important factor that governs the choice of the illumination or detection area is the coherence of the scattered field. In FCS where there is no spatial coherence between fluctuating florophores, the limitation of the illumination area is dependent on the number of florophores within it. On the other hand, both DLS and XPCS rely on the spatial coherence of the scattered field such that the size of the detection area is determined by the number of coherence areas and not the number of molecules within the illumination/detector area.

Similarly, the illumination area of coherent SHCS is determined by the spatial and temporal coherence of the SH output. However, the emissive coherent nature of SHG gives it a large coherence area with a relatively long coherence length under the proper experimental conditions described in Chapter 4.[38] The spatial coherence of the SH output is essentially equal to the overlapped area of the two spatially coherent incident beams.

This is quite different from DLS or XPCS where the spatial coherence is dependent on the angular separation between molecules and the incident wavelength, more akin to diffraction seen from a slit experiment. This is primarily due to the emissive process of SHCS as compared to the nonemissive scattering processes of DLS and XPCS. The large spatial coherence from the emissive SH output allows the illumination area and detection area to be kept large without decreasing the S/N of the correlation data. Additionally, using a counter-propagating SHG setup (as described in Chapter 2)[44] produces an extremely temporally coherent output where any distortion in the wavefront of the generated SH output is minimized as it is produced normal to the surface and not at an angle. This is not found in either DLS or XPCS as the scattered light necessarily comes out at an angle and loses its temporal coherence over a much shorter distance. The emission of the SH output normal to the surface allows the output to maintain its large spatial coherence over a long distance. In other words, the SH output is both extremely spatially and temporally coherent. The temporal coherence can be described by the length over which the SH output remains spatially coherent. This distance known as the confocal distance is dependent on illumination area and can be calculated for a propagating Gaussian beam by,[45]

$$C_L = \frac{\pi w_o^2}{\alpha \lambda}, \tag{5.18}$$

where w_0 is the detection area width, λ is the wavelength of the SH output and α represents the inherent nonideality of the incident beam from a plane-wave calculated in Chapter 4 to be equal to 2.33.[38] Consider a spatially coherent illumination area whose diameter is ~ 1 mm, using Equation 5.18 the expected coherence length would be ~ 5 m. As long as the detector is within this distance and the detection area is kept the same as

the spatially coherent illumination area, the detected intensity generated is from a spatially and temporally coherent plane-wave with a Gaussian intensity profile with only one intensity maximum. This situation is consistent with keeping the detection area smaller than one angular separation in DLS or XPCS in order to maintain spatial coherence and minimize the number of simultaneously detected intensity maxima. For practical purposes, the detector-sample distance in the SHCS studies presented here and in the following chapters was well-below the coherence length, usually only ~ 5 cm, providing an extremely spatially and temporally coherent wavefront at the detector.

The dependence of the coherence length on the size of the illumination area was shown in Chapter 4 to follow Equation 5.18 for SH emission produced using a counter-propagating optical arrangement. The coherence length was determined using lens-less surface SHG imaging (SSHGI) by incorporating the SHG active small molecule SBN into various sized DOPC PSLBs patterned using the USAF resolution test target.[38] The lens-less SSHG image of two different sized linewidths, 355 and 397 μm, is reproduced here from Figure 4.4 and shown in Figure 5.2A. For comparison a white light image of the same linewidths of the test target are shown in Figure 5.2D. The lens-less SSHG images show no diffraction and are readily resolvable at the detector-sample distance of 7 cm used to obtain the images. However, at further detector-sample distances diffraction was seen, indicating the loss of spatial coherence at that distance. As mentioned in Chapter 4, for the linewidths of 355 and 397 μm shown in Figure 5.2A, the coherence length was found to be approximately 64 and 80 cm, respectively. The distance dependence of the coherence length was found to follow Equation 5.18 where larger illumination areas (or linewidths) maintained spatial coherence over a greater distance

compared to smaller illumination areas. It is important to note that as the illumination area decreases, the temporal coherence or coherence length also decreases, as illustrated in Equation 5.18. This means that if the detector position is kept constant while the illumination area is decreased there would be a decrease in the measured fluctuations in intensity due to the decreased coherence. Chapter 4 not only demonstrates the large spatial coherence of the SH output (equal to the size of the illuminated area at distance zero), but also demonstrates that the temporal coherence is longer the larger the illumination area. For SHCS, the longer temporal coherence for large illumination areas means the illumination area can be kept much larger as compared to DLS and XPCS.

DLS and XPCS are scattering processes where the incident light interacts with the sample to generate nonemissive scattering. This is akin to back illuminating the USAF test target with an excitation light source as shown in Figure 5.2B for linewidths 355 and 397 μm (reproduced from Figure 4.8). These images are less discernable due to the loss of coherence and resulting diffraction at the same detector-sample distance (7 cm) used in Figure 5.2A. As with any diffraction or scattering experiment if a pinhole aperture at the detector was used to minimize the detection area to one coherence area than the image would be discernable and exhibit minimal diffraction. Comparing the images in Figure 5.2A and 5.2B it is apparent that the coherent properties of the system are significantly different for an emissive (SHCS) or scattering (DLS and XPCS) process where the former exhibits much greater spatial and temporal coherence.

An image of the same linewidths shown in Figure 5.2 was also obtained using lens-less fluorescence imaging, an incoherent emissive process (reproduced from Figure 4.9 and shown in Figure 5.2C). The lack of any discernable features seen in the lens-less

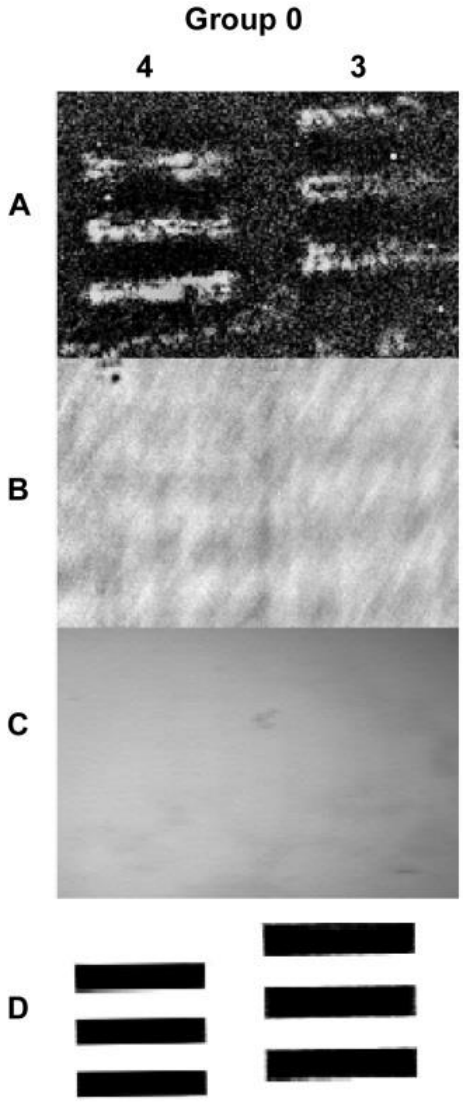

Figure 5.2. Comparison of coherence area and length between (A) lens-less SH imaging, (B) back illumination UV imaging, and (C) lens-less fluorescence imaging. (D) is a white light image of the USAF test target group 0 elements 3 (397 μm) and 4 (355 μm).

fluorescence image suggests that when there is complete incoherence, even if it is an emissive process, the linewidths cannot be resolved. Clearly, spatial coherence is necessary to resolve any image and temporal coherence is necessary to image at longer distances. The images in Figures 5.2A-C visually exhibit the difference between emissive (SHCS) and scattering processes (DLS and XPCS), as well as spatially coherent (SHCS) and incoherent processes (FCS). An emissive coherent process generates a much more spatially coherent output than a nonemissive process. Even though the excitation source is coherent, scattering processes, such as DLS and XPCS, are susceptible to diffraction if the detection area is larger than one coherence area. An emissive incoherent process, such as FCS, drastically limits the size of the illumination area to include as few molecules as possible as there is effectively no coherence area. The result of SHG having greater coherence for larger illumination areas suggests that minimization of the illumination area in order to improve spatial coherence, as seen in DLS or XPCS, is not as necessary or beneficial in SHCS.

5.6 Correlation Function Signal-to-Noise

There are a variety of factors that contribute to the S/N detected in the correlation data. The most significant of these is the shot noise of the detection system.[3,4] Most of the shot noise from the detection system is unavoidable; however, the majority of the noise from the detection system is uncorrelated and can simply be removed from the correlation data by removing the first data point or filtering the high frequency detection system noise.[42] Fluctuations in the laser intensity can also distort the correlation data. However, as a suitable laser can be tuned to produce a high quality TEM00 mode beam

and if a pinhole aperture is used to spatially filter the output of the laser, the noise contributions due to spatial inhomogeneities in the beam can be significantly reduced. Additionally, the noise from a suitable "background" sample can be monitored and correlated to determine if any correlated noise exists from the laser, background matrix or detection system. This will be shown in more detail in the following chapters where the correlation data from a pure DOPC bilayer (the background matrix) does not exhibit any correlation, indicating there were no correlated contributions from either the background matrix, laser optics or detector system. It is important to note that extreme care must be taken to align the cavity of the laser and optimize the beam intensity distribution, as these parameters greatly affect the noise of the correlation data and can prevent resolvable correlation data from being obtained. Maintaining the laser so it is stable means that most of the noise seen in the correlation data will be due to the detection system shot noise. The detection system noise is constant regardless of the system being probed,[3,4] meaning that heterodyne optical mixing between the SH mean intensity and the intensity fluctuations (discussed earlier) will lead to an increase in the S/N of the correlation data.[35] As shown earlier, using heterodyne mixing an increase in the SH mean intensity will increase the measured intensity fluctuations, leading to an increase in the S/N of the correlation data.

In Equations 5.3 and 5.4 it was shown that the square-root of the SH mean intensity, $\sqrt{I_{SH}}$, is linearly proportional to N_μ. Since the cross-term in Equation 5.8 is the dominant contributing term to the correlation data, it can be concluded that the S/N of the correlation data is linearly proportional to N_μ, or in other words is linearly proportional to the $\sqrt{I_{SH}}$. Experimentally, this is can be shown by collecting correlation data for the same

system at multiple excitation power intensities, which would increase the measured SH mean intensity while keeping the system otherwise unchanged (i.e., same number of molecules, same illumination area, same detection area). Here, data for the binding of 240 nM CTb to a GM_1 doped DOPC bilayer were collected over time (for at least 2 hrs) for every pulse of a 20 Hz Nd:YAG laser. Correlation data were obtained using three different laser powers (15 mJ/pulse, 21 mJ/pulse, and 25 mJ/pulse), which lead to an increase in the measured SH mean intensity. The S/N of the correlation data was calculated by taking the ratio of the amplitude of the correlation data at time zero to the standard deviation at long time. Plotting the S/N of the correlation data as a function of the $\sqrt{I_{SH}}$ shows that there is indeed a linear relationship (shown in Figure 5.3). The data in Figure 5.3 not only illustrate there is an increase in the correlation data S/N as the SH mean intensity is increased, but also show that heterodyning does in fact lead to a linear relationship between the correlation data and *N*. It is important to note that the S/N ratio approaches 1 as $\sqrt{I_{SH}}$ approaches 0; this stems from the fact that in the absence of any correlated fluctuations there will always be uncorrelated detection system noise in the correlation data where the signal (the magnitude of the correlation data) is equal to the noise (the standard deviation in the long time).

It is obvious from Equations 5.3 and 5.4 and Figure 5.3 that the most straightforward way to increase the overall SH intensity and S/N of the correlation data is to either increase the total density of molecules, *N*, or increase the overall power generated from the incident electric fields. This is similar to what is seen in DLS and XPCS; however, the larger spatially and temporally coherent output seen in SHCS as opposed to either DLS or XPCS makes it unnecessary to decrease the illumination or

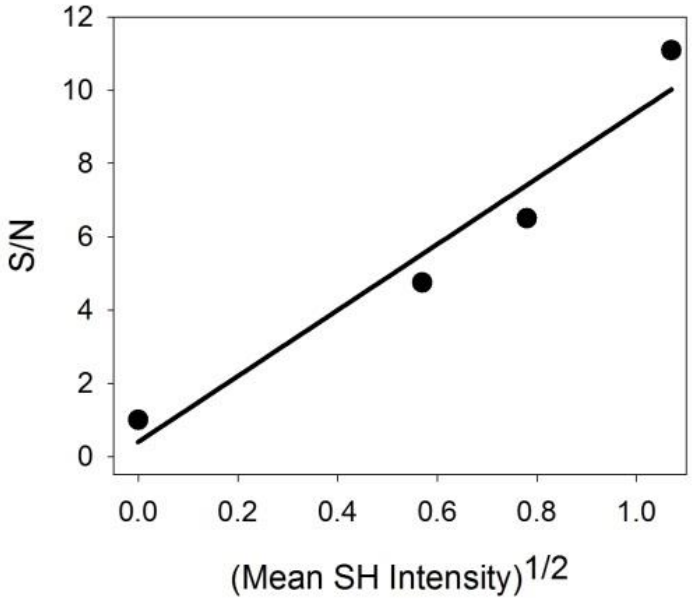

Figure 5.3. Plot of the S/N of the correlation data for 240 nM CTb binding to a GM_1 doped DOPC bilayer as function of $\sqrt{I_{SH}}$. The three laser powers used to collect the data were 15 mJ/pulse, 21 mJ/pulse and 25 mJ/pulse.

detection area in order to increase the S/N of the correlation data. To demonstrate the S/N of the correlation data is not improved when either the illumination or detection area is decreased, correlation data for 240 nM CTb binding to a GM_1 doped DOPC bilayer were collected for a 1 mm^2 detection area and a 0.6 mm^2 detection area (data shown in Figure 5.4). The detection area was adjusted by placing an aperture in front of the detector and opened to either 1 mm^2 and 0.6 mm^2. From the data in Figure 5.4 it is apparent that the larger detection area of 1 mm^2 (Figure 5.4A) has less noise in the correlation data as compared to the smaller 0.6 mm^2 detection area (Figure 5.3B). The calculated S/N of the correlation data for Figure 5.4A and 5.4B are 11.2 and 6.4, respectively. Although the reaction rate for both sets of correlation data is the same, it is clear decreasing the detection area does not lead to better S/N of the correlation data and in fact leads to a significant decrease in the S/N of the correlation data. Additionally, it is interesting to note that for the smaller (0.6 mm^2) detection area the collection time of the correlation data was 3 times longer (6 hrs) than the larger (1 mm^2) detection area and it still has more noise. This is consistent with Koppel's prediction that the S/N of the correlation data is proportional to $\langle n \rangle T^{1/2}/N_c$.[28] Since the correlation data shown in both Figures 5.4A and 5.4B are within one coherence area (N_c) or spatially coherent and the photocount ($\langle n \rangle$) significantly decreases from Figure 5.4A (1 mm^2) to 5.4B (0.6 mm^2) the collection time (T) necessarily had to be increased for Figure 5.4B to maintain the same S/N as Figure 5.4A.

Although increasing the density of molecules within the illumination area (Figure 5.3) or increasing the illumination area (Figure 5.4) will increase the SH intensity and the S/N of the correlation data, the collection time also significantly impacts the S/N of the

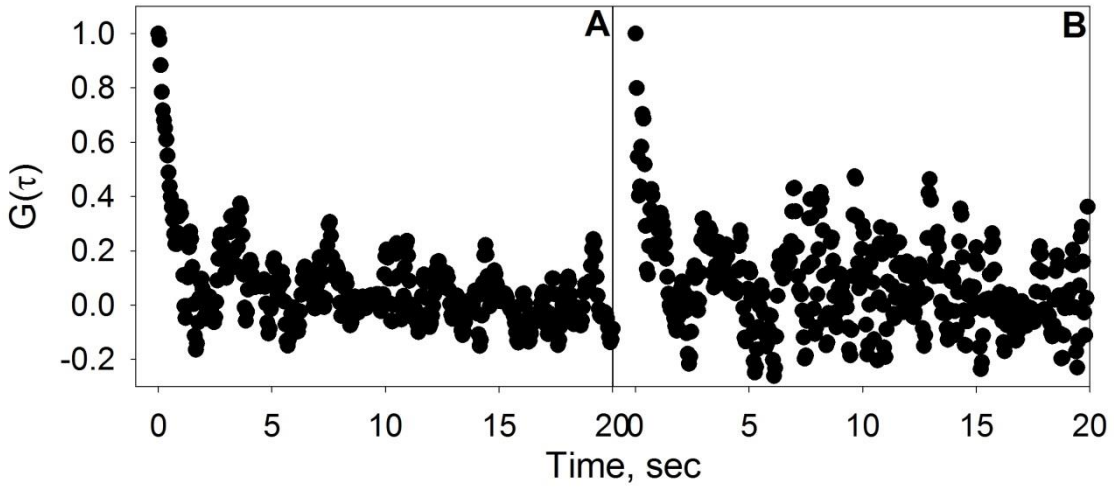

Figure 5.4. Correlation data as function of detection area for 240 nM CTb to a 1 mol % GM_1 doped DOPC bilayer using a detection area of (A) 1 mm^2 and (B) 0.6 mm^2.

correlation data.[28] This is especially true when detecting small fluctuations within a large number of molecules. The S/N of the correlation data is dependent on the photocount, the number of coherence areas, and the collection time ($S/N \propto \langle n \rangle \mathrm{T}^{1/2}/\mathrm{N}_c$). If the illumination area is already spatially coherent (one coherence area) and the photocount is as high as possible, then adjusting the collection time is necessary to improve the S/N of the correlation data. The contribution of the additional noise to the correlation data due to the finite collection time can be expressed as,[3,28]

$$\frac{S}{N} \propto \sqrt{\mathrm{T}}. \tag{5.19}$$

Equation 5.19 illustrates the importance of choosing an appropriate collection time to obtain reasonable S/N. To improve the S/N of the correlation data, the collection time needs to be long enough to collect a large enough number of dynamic events. For a large density of molecules this time may be relatively long. For example, FCS experiments have on average 10^3 molecules in the detection area whose diffusion dynamics occur on a time constant below a few milliseconds. This means resolvable correlation data can be obtained in less than a few mins.[32,37,42] The average collection time for FCS experiments of this type is typically well below a minute with the longest collection time found to be 10-15 min for longer dynamic rates. On the other hand, for a density of molecules on the order of 10^6 or greater, the collection time required to obtain resolvable correlation data is much longer, on the order of hrs. This can be seen in Figure 5.5A-C, which shows the correlation data obtained for three collection times for the same sample. In Figure 5.5A-C, the binding of 240 nM CTb to a GM_1 doped DOPC lipid bilayer was analyzed using SHCS with a calculated surface density of 8.8 $\times 10^{11}$ molecules. The intensity fluctuations were monitored for over 2 hrs and then analyzed by taking a 10 min segment of data

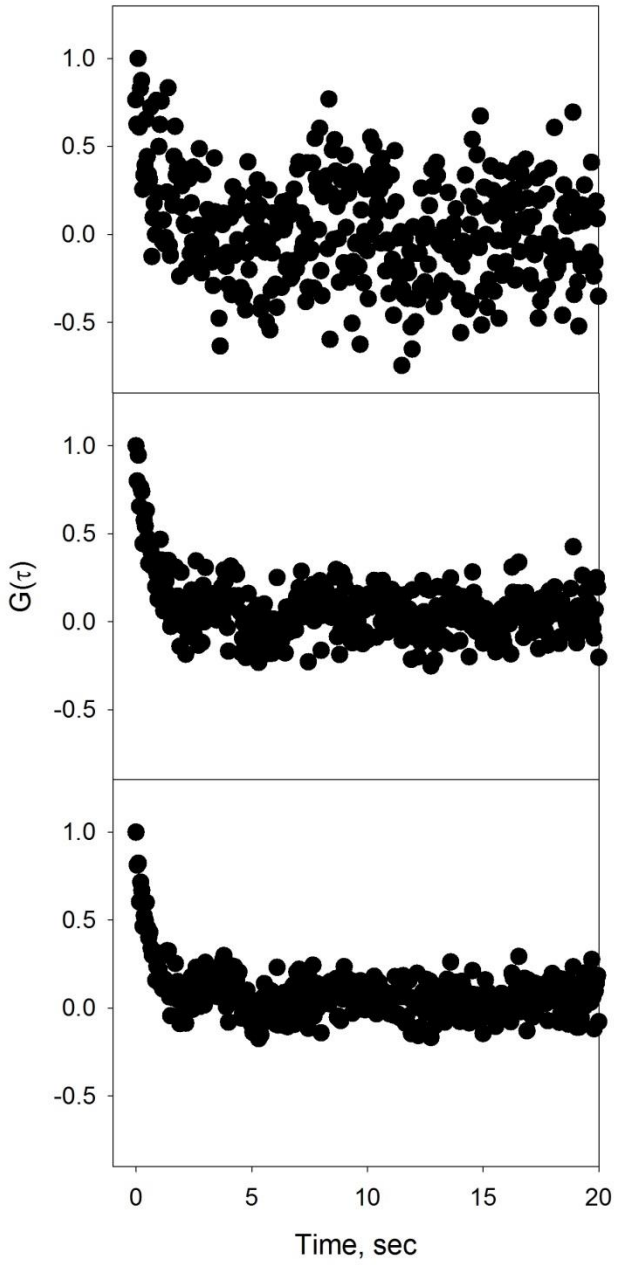

Figure 5.5. Correlation data as a function of collection time from measured intensity fluctuations collected for every pulse of a 20 Hz laser over time for the binding of 240 nM CTb to a GM_1 doped DOPC lipid bilayer for a collection time of (A) 10 min, (B) 1 hr, and (C) 2 hrs.

(Figure 5.5A), an hr segment of data (Figure 5.5B) and finally for the entire 2 hr data collection. (Figure 5.5C).

It is apparent that the shortest collection time (~10 min) is not long enough to extract the dynamics of the system as there are not enough dynamic events collected to be detectable; however, as the collection time is increased more dynamic events are collected. Additionally, as predicted by Equation 5.19 an increase in the S/N of the correlation data is seen as the collection time is increased. It is also important to note that the time constant of the dynamics shown in Figure 5.5A-C is on the scale of seconds, much longer than typical FCS diffusion experiments, which requires additional collection time to retain the same S/N.[28] For the data in Figure 5.5A-C the calculated S/N increases from 3.7 at a collection time of 10 min to 8.8 for 1 hr and 11.2 for 2 hrs of collection time. Plotting the experimental S/N versus $T^{1/2}$ produces a linear relationship as predicted by Equation 5.19 (shown in Figure 5.6), illustrating that the correlation data in Figures 5.5A-C are in fact from correlated molecular dynamics not merely from system noise. Clearly, the S/N is drastically affected by the collection time and must be significantly large when there is a large density of molecules in a large detection area in order to produce resolvable correlation data where there are enough dynamic events to make the intensity fluctuations detectable.

Another interesting observation related to the S/N in the SHCS setup employed here and the following chapters is that although the illumination area was kept rather large ~ 1 mm^2, only about 8% of the total area was actually responsible for the detected SH intensity. This was determined by taking an image of the illumination area using a CCD camera and integrating for 5 mins (this was the minimum integration time required

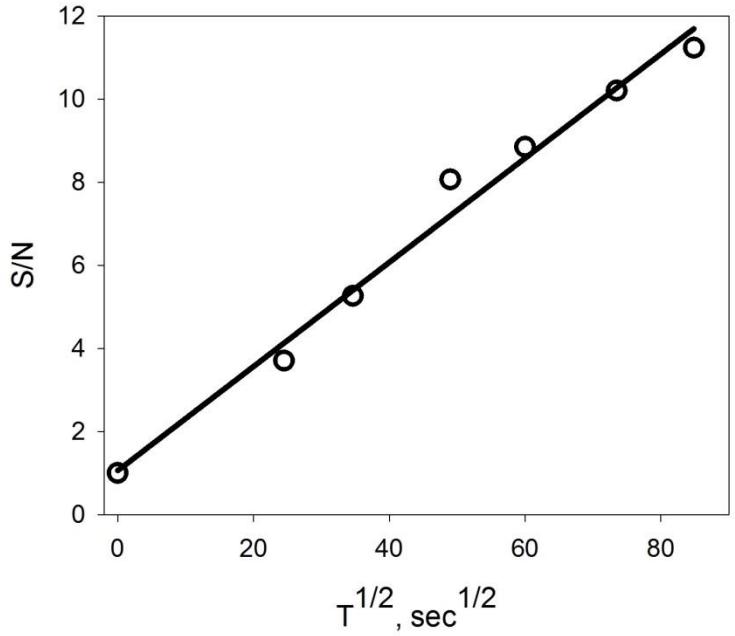

Figure 5.6. S/N of the correlation data as a function of the square-root of collection time from measured intensity fluctuations collected for every pulse of a 20 Hz laser over time for the binding of 240 nM CTb to a GM_1 doped DOPC lipid bilayer.

to visualize the illumination area). The resulting image is shown in Figure 5.7 with the imaged beam area equal to 1.4 mm^2. Here again, the same binding system used in Figure 5.1 was used. By subtracting the background noise from the detector (outside the illumination area) and then calculating the number of photons above the background threshold, the percent of the total area above the background could be calculated. For Figure 5.7 the contribution area above background was ~0.12 mm^2, which accounts for only 8% of the total illumination area. Thus, although in a beam area of ~ 1 mm^2 covered with a monolayer of protein whose diameter is ~14 nm there will be roughly 10^{11} protein molecules, only 8% will contribute to the measured SH intensity. It is important to note that this percentage is likely much smaller for the instantaneous SH intensity measured from the fluctuations as the image in Figure 5.7 was averaged for 5 mins and the fluctuations are only measured for the laser pulse duration of ~7 ns.

5.7 Summary

The general principles of correlation spectroscopy coupled with SHG were presented here. The advantages of the coherence and heterodyning possible with SHG and its contributions to the correlation data were thoroughly described. The large spatial and long temporal coherence of the SH output make it possible to have a large illumination and detection area without decreasing the S/N of the correlation data. In other incoherent correlation spectroscopies and scattering techniques the coherence area is nonexistent or small and as such the illumination/detection area must be kept small in order to improve the S/N of the correlation data. An additional advantage of SHCS is the enhancement in the measured SH intensity from the fluctuations by the mean SH

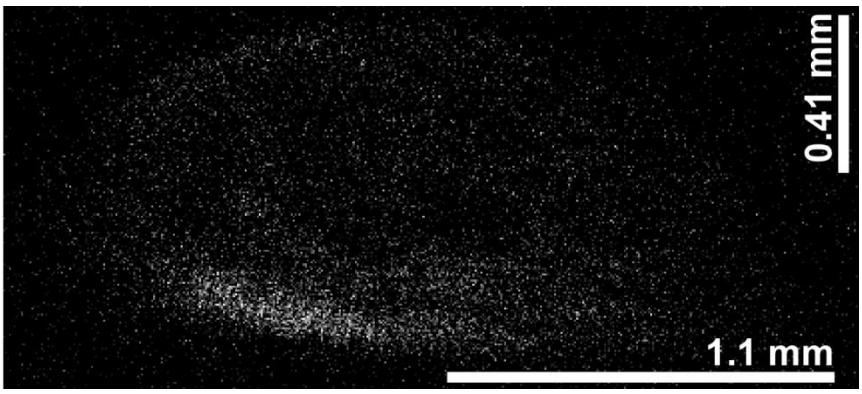

Figure 5.7. SHG image of the beam area with the 8% of photons responsible of detected SH intensity illuminating above the background.

intensity. This heterodyning effect increases the S/N of the correlation data as the mean intensity is increased while the majority of the noise, which comes from the detection system, remains constant. Sufficient collection time can also be adjusted to increase the S/N of the correlation data. Carefully choosing the proper parameters allows the instantaneous fluctuations in SH intensity to be detected and correlated to extract surface dynamic processes. The incredible surface specificity and label-free nature of SHCS make it extremely useful in extracting the binding kinetics of surface biomolecular interactions and will be utilized to this end in the following chapters.

5.8 References

(1) van Hove, L. *Phys. Rev.* **1954**, *95*, 249-262.

(2) Pecora, R. *J. Chem. Phys.* **1964**, *40*, 1604-1614.

(3) Pecora, R.;*Dynamic Light Scattering: Applications of Photon Correlation Spectroscopy*; Plenum Press: New York, 1985.

(4) Cummins, H. Z.; Pike, E. R.;*Photon Correlation and Light Beating Spectroscopy*; Plenum Press: New York, 1973; Vol. 3.

(5) Cummins, H. Z.; Knable, N.; Yeh, Y. *Phys. Rev. Lett.* **1964**, *12*, 150-153.

(6) Bismuto, E.; Gratton, E.; Lamb, D. C. *Biophys. J.* **2001**, *81*, 3510-3521.

(7) Chattopadhyay, K.; Saffarian, S.; Elson, E. L.; Frieden, C. *Biophys. J.* **2005**, *88*, 1413-1422.

(8) Starr, T. E.; Thompson, N. L. *Biophys. J.* **2001**, *80*, 1575-1584.

(9) Fahey, P. F.; Koppel, D. E.; Barak, L. S.; Wolf, D. E.; Elson, E. L.; Webb, W. W. *Science* **1977**, *195*, 305-306.

(10) Hansen, R. L.; Harris, J. M. *Anal. Chem.* **1998**, *70*, 4247-4256.

(11) Asiala, S. M.; Schultz, Z. D. *Anal. Chem.* **2014**, *86*, 2625-2632.

(12) Brun, N.; Poncot, M.; Bourson, P. *Chemom. Intell. Lab. Syst.* **2013**, *128*, 77-82.

(13) Riese, D. O.; Vos, W. L.; Wegdam, G. H.; Poelwijk, F. J.; Abernathy, D. L.; Grubel, G. *Phys. Rev. E Stat. Phys., Plasmas, Fluids, Relat. Interdiscip. Top.* **2000**, *61*, 1676-1680.

(14) Dierker, S. B.; Pindak, R.; Fleming, R. M.; Robinson, I. K.; Berman, L. *Phys. Rev. Lett.* **1995**, *75*, 449-452.

(15) Eisebitt, S.; Lorgen, M.; Eberhardt, W.; Luning, J.; Stohr, J.; Rettner, C. T.; Hellwig, O.; Fullerton, E. E.; Denbeaux, G. *Phys. Rev. B Condens. Matter Mater. Phys.* **2003**, *68*, 104419/104411-104419/104416.

(16) Grubel, G.; Abernathy, D. L.; Riese, D. O.; Vos, W. L.; Wegdam, G. H. *J. Appl. Crystallogr.* **2000**, *33*, 424-427.

(17) Gassin, P.-M.; Martin-Gassin, G.; Benichou, E.; Brevet, P.-F. *J. Phys. Chem. C* **2014**, *118*, 1135-1141.

(18) Geissbuehler, M.; Bonacina, L.; Shcheslavskiy, V.; Bocchio, N. L.; Geissbuehler, S.; Leutenegger, M.; Marki, I.; Wolf, J.-P.; Lasser, T. *Nano Lett.* **2012**, *12*, 1668-1672.

(19) Zhao, X.; Eisenthal, K. B. *J. Chem. Phys.* **1995**, *102*, 5818-5826.

(20) Rodriguez-Maldonado, L.; Fernandez-Nieves, A.; Fernandez-Barbero, A. *Colloids Surf., A* **2005**, *270-271*, 335-339.

(21) Nordmeier, E. *J. Phys. Chem.* **1993**, *97*, 5770-5785.

(22) Lisicki, M.; Cichocki, B.; Rogers, S. A.; Dhont, J. K. G.; Lang, P. R. *Soft Matter* **2014**, *10*, 4312-4323.

(23) Tsunashima, Y.; Nemoto, N.; Kurata, M. *Macromolecules* **1983**, *16*, 1184-1188.

(24) Tsunashima, Y. *J. Chem. Phys.* **2001**, *114*, 9163-9169.

(25) Zimnyakov, D. A.; Chekmasov, S. P.; Sviridov, A. P.; Ushakova, O. V.; Bagratashvili, V. N. *Laser Phys. Lett.* **2013**, *10*, 045601/045601-045601/045605, 045605 pp.

(26) Magde, D.; Elson, E.; Webb, W. W. *Phys. Rev. Lett.* **1972**, *29*, 705-708.

(27) Saffarian, S.; Elson, E. L. *Biophys. J.* **2003**, *84*, 2030-2042.

(28) Koppel, D. E. *Physical Review A* **1974**, *10*, 1938-1945.

(29) Thompson, N. L.; Navaratnarajah, P.; Wang, X. *J. Phys. Chem. B* **2011**, *115*, 120-131.

(30) Lagerholm, B. C.; Thompson, N. L. *Biophys. J.* **1998**, *74*, 1215-1228.

(31) Kuttner, Y. Y.; Kozer, N.; Segal, E.; Schreiber, G.; Haran, G. *J. Am. Chem. Soc.* **2005**, *127*, 15138-15144.

(32) Kelly, C. V.; Wakefield, D. L.; Holowka, D. A.; Craighead, H. G.; Baird, B. A. *ACS Nano* **2014**, *8*, 7392-7404.

(33) Machan, R.; Jurkiewicz, P.; Olzynska, A.; Olsinova, M.; Cebecauer, M.; Marquette, A.; Bechinger, B.; Hof, M. *Langmuir* **2014**, *30*, 6171-6179.

(34) Thompson, N. L.; Axelrod, D. *Biophys. J.* **1983**, *43*, 103-114.

(35) Gutt, C.; Ghaderi, T.; Tolan, M.; Sinha, S. K.; Grubel, G. *Phys. Rev. B Condens. Matter Mater. Phys.* **2008**, *77*, 094133/094131-094133/094110.

(36) Sikharulidze, I.; Dolbnya, I. P.; Madsen, A.; de Jeu, W. H. *Opt. Commun.* **2005**, *247*, 111-124.

(37) R.Lakowicz, J.;*Topics in Fluorescence Spectroscopy*; Plenum Press, 1991; Vol. Volume 1.

(38) Sly Krystal, L.; Nguyen Trang, T.; Conboy John, C. *Opt Express* **2012**, *20*, 21953-21967.

(39) Zhao, X.; Goh, M. C.; Subrahmanyan, S.; Eisenthal, K. B. *J. Phys. Chem.* **1990**, *94*, 3370-3373.

(40) Yan, E. C. Y.; Eisenthal, K. B. *J. Phys. Chem. B* **2000**, *104*, 6686-6689.

(41) Sly, K. L.; Mok, S.-W.; Conboy, J. C. *Anal. Chem.* **2013**, *85*, 8429-8435.

(42) Hansen, R. L.; Harris, J. M. *Anal. Chem.* **1998**, *70*, 2565-2575.

(43) Thompson, N. L.; Burghardt, T. P.; Axelrod, D. *Biophys. J.* **1981**, *33*, 435-454.

(44) Kriech, M. A.; Conboy, J. C. *J. Opt. Soc. Am. B: Optical Physics* **2004**, *21*, 1013-1022.

(45) Goldsmith, P. F. *Quasioptical Systems: Gaussian Beam Quasioptical Propagation and Applications*; IEEE Press, 1998.

CHAPTER 6

INVESTIGATION OF SMALL MOLECULE-MEMBRANE KINETICS USING SECOND HARMONIC CORRELATION SPECTROSCOPY

Reprinted (adapted) with permission from Sly, K. L.; Mok, S.-W.; Conboy, J. C. *Anal. Chem.* **2013**, *85*, 8429-8435.

6.1 Introduction

In Chapter 3 SH spectroscopy was used to determine the binding kinetics and thermodynamics of proteins adsorbing to a biotinylated DOPC lipid bilayer using a conventional binding isotherm. Since the protein concentrations were in the low nM range and required data for several protein concentrations, collection of the binding isotherm required a significant amount of time to reach binding saturation and a significant amount of analyte. In this chapter the method of SHCS, which was developed in Chapter 5, is shown to provide equivalent information on surface binding kinetics and thermodynamics as conventional binding isotherms, but with the advantage of requiring less time and analyte as only one analyte concentration is needed to accurately determine the binding kinetics.

As mentioned in Chapter 5, SHCS is a statistical method that uses the local

fluctuations of the measured SH signal to determine the binding kinetics and thermodynamics of molecules at a surface, similar to photon correlation spectroscopy and FCS. Also noted in Chapter 5, FCS is the one of the most recognized forms of correlation spectroscopy, where fluctuations in the fluorescence signal from a sample of fluorescent molecules are used to characterize the correlated molecular processes that give rise to these fluctuations.[1] Most notably, FCS has been used to analyze lipid and protein diffusion,[2,3] protein aggregation,[4,5] simulated muscle contractions,[6] and surface binding kinetics of fluorescently labeled biomolecules.[7-13] For example, the reversible binding of fluorescently labeled IgG to albumin-coated surfaces and planar supported lipid bilayers (PSLB) doped with Fc receptors,[7,8] rhodamine 6G association to C18 functionalized surfaces,[9,10] and DNA hybridization at a water/glass interface have all be investigated using FCS.[13] In these studies the temporal fluctuations in the fluorescence signal were measured from a small observation volume created using total internal reflection and correlated to obtain information about the dynamics of interfacial binding. The properties of FCS, namely its incoherent nature and contributions from diffusion of molecules in solution, were discussed in Chapter 5 and shown to drastically affect the resulting collection and interpretation of the correlation function. Specifically, fluorescence correlation data are complicated by fluorescence arising from species in solution, background fluorescence, and photobleaching. These contributions to the measured correlation function confound the analysis of the surface dynamic processes.[14] Small solution volumes and low analyte concentrations, down to single-molecule detection level, have been used to circumvent these issues, but the barrier to a meaningful correlation function then becomes the time required to collect enough dynamic molecular

events.[14]

Chapter 5 describes how the application of correlation spectroscopy to a label-free, surface specific and coherent technique such as SHG would eliminate observable fluctuations from molecular diffusion in solution and ameliorate problems associated with the degradation of fluorophores without having to necessarily reduce the number of molecules in the observation area. In this sense SHCS was shown to be more akin to DLS and XPCS than FCS; however the much larger coherence area observable in SHCS compared to DLS or XPCS makes limiting the detection area even more unnecessary. For SHCS the only contributions to the measured temporal fluctuations in the signal will arise from surface associated species, given the time interval is much longer than the time constant for rotational diffusion and the surface binding dynamics are much faster than translational diffusion. This greatly simplifies the correlation function of SHCS and eliminates obstacles due to fluorescent molecules in bulk solution as shown in Chapter 5. In the previous chapter it was mentioned that there have been a few instances where SHCS had been implemented to determine the translational and rotational diffusion coefficients of large dye molecules[15-17] and clay particles;[18] however, SHCS has yet to be utilized to determine the binding kinetics of surface biomolecular interactions. As such, in this chapter SHCS is used to ascertain the binding kinetics and thermodynamics of a small molecule associating with a PSLB for the first time.

To demonstrate the feasibility of SHCS to effectively determine the binding kinetics of a molecule to a surface, the SHG active small molecule, SBN, associating with a DOPC PSLB is examined. The results obtained from SHCS are compared to a classical binding isotherm experiment to verify the accuracy of the kinetic and

thermodynamic values retrieved from the SHCS analysis. Using SHCS, both the adsorption and desorption rates are simultaneously determined using only one steady-state concentration in a much shorter time period as compared to the conventional isotherm study. Thus, SHCS provides a more efficient and comprehensive method for studying molecular interactions at a surface without the need for an exogenous label.

6.2 SHCS Theory

The SHCS theory and correlation function describing surface biomolecular interactions is detailed in Chapter 5 and will be used for the study presented in this chapter. As mentioned in Chapter 5, it is beneficial to have a high SH intensity and as shown in Chapter 2 the SH intensity can be enhanced when the incident, ω, or SH, 2ω, frequency is resonant with an electronic transition of a molecule at the interface. In this chapter a fundamental wavelength of 532 nm is used such that the resulting SH wavelength is 266 nm, which is in resonance with the electronic transition of the small molecule SBN (shown in Figure 6.1). The signal enhancement from this resonance also has the added benefit of allowing detection down to nM concentrations of SBN.[23,24]

The small molecule SBN, investigated in this study, has previously been shown to reversibly bind to a lipid bilayer.[19] Due to the reversible binding of SBN to a lipid bilayer and the finite number of binding sites on the PSLB, typical bimolecular reversible binding at a surface can be assumed.[19] As such, the correlation function developed in Chapter 5 and expressed in Equation 5.17 can be used to analyze the SHCS data obtained in this study.

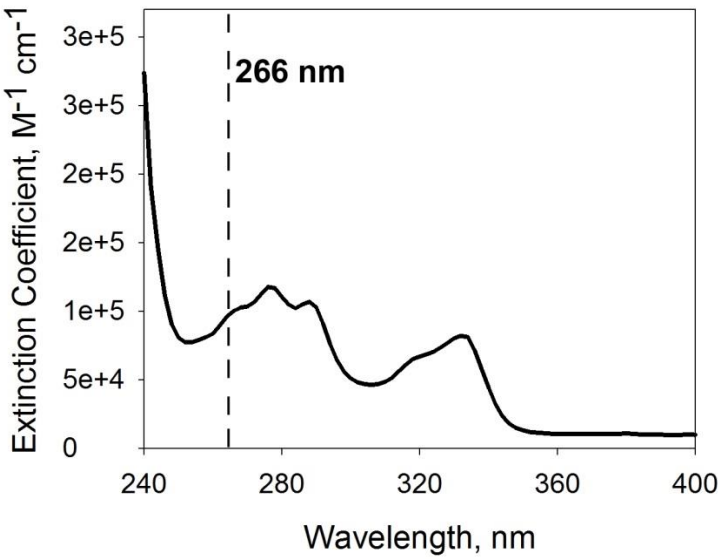

Figure 6.1. Extinction coefficient spectra of SBN.

6. 3 Experimental Design

6.3.1 Materials

DOPC from Avanti Polar Lipids and SBN from Sigma-Aldrich were both used as received. Other materials used in this study, such as the water, PBS buffer and fused silica substrates were described in detail in section 3.2.1. SBN was dissolved in PBS pH 7.4 to the desired working concentrations (0.43 nM to 20 μM for the isotherm studies and 55 μM for the autocorrelation studies). The PSLBs used in this study were formed using vesicle fusion as described in section 3.2.3.

6.3.2 SHG Measurements

The counter-propagating SHG setup used for these experiments has been described in detail in Chapter 2.[20] In this chapter, the second harmonic output (532 nm) of a Nd:YAG laser (Continuum, Surelite II, 20 Hz, 7ns pulse) was directed towards a prism/water interface under total internal reflection. The laser intensity at the sample was 24 mJ/pulse and the beam size was ~ 1 mm^2 in diameter. The reflected beam was steered back on itself to overlap spatially and temporally with the incident beam, resulting in an SH emission at 266 nm along the surface normal. Two notch filters (Semrock) were used to allow only light from the SHG signal through before collection by a solar-blind photomultiplier tube (Hamamatsu).

6.3.3 SHCS Measurements

Autocorrelation experiments of SBN association to a DOPC bilayer were performed using a concentration well above the SBN saturation concentration, 55 μM,

after a steady-state response had been reached. Single pulse data collection was recorded so that the time interval was dictated by the 20 Hz laser (50 msec.). Each data set was collected for 100 s such that there were 2,000 data points. For one experiment five data sets were consecutively collected totaling 10,000 data points. Twenty-five data sets from 5 separate experiments were each cross-correlated with itself and then averaged to form the correlation function.

6.3.4 Adsorption Isotherm Measurements

For the standard binding isotherm of SBN adsorption to a DOPC bilayer, three independent binding experiments and three control experiments were conducted. For these experiments, increasing concentrations of SBN ranging from 0.43 nM to 20.02 μM were injected and allowed to reach equilibrium between the bulk solution and bilayer. To compensate for the bulk SBN depletion, an injection of the same SBN concentration was made every 5 to 10 mins until a steady-state response was reached. Typically, the lowest concentrations required between 1 to 2 hrs to reach equilibrium. The SH intensity was recorded using time averaging of 100 samples per data point at 10 min intervals for 3 to 5 mins to allow kinetic measurements to be made as a function of time. Isotherm measurements were made using only the SH intensity collected at steady-state equilibrium for each SBN concentration. To compare multiple data sets, a two-point normalization to a 10 mM KOH solution and a solution of PBS pH 7.4 was performed on the measured SH intensity, followed by subtraction of the background signal before addition of SBN.

6.4 Results and Discussion

6.4.1 Binding Kinetics of SBN Association to DOPC Using SHCS

The SH signal collected for every pulse of the 20Hz laser as a function of time for a bulk solution concentration of 55 μM SBN intercalating into a DOPC bilayer is shown in the inset of Figure 6.2A. The fluctuations in the SH signal primarily arise from uncorrelated photon shot noise, but some of the fluctuations arise from correlated dynamic molecular events occurring at the surface. To extract the correlated events, the fluctuations in the SH signal were autocorrelated. The measured fluctuations from the mean SH signal were assumed to be linear with the surface density of molecules, N, as discussed in Chapter 5. Analysis of the square root of the SH intensity deviations (data not shown) confirms this assumption to be accurate, and in fact produces the same autocorrelation function. The normalized autocorrelation, $G(\tau)$, from 25 data sets of SBN intercalating into a DOPC bilayer is shown in Figure 6.2A, where every 10^{th} data point is shown for ease of visualization. The first point of the correlation function has been removed as it contains the contributions from photon shot noise.[10] Autocorrelation was also performed on 20 data sets of a pure DOPC bilayer in order to verify there was indeed no correlation in the SH signal obtained from the bilayer alone or from photon shot noise on the time scale of the molecular dynamic events on the surface, as this would contribute to the correlation seen for the association of SBN to the DOPC bilayer. The resulting correlation function from the pure DOPC bilayer is shown in Figure 6.2B with the raw collected SH signal fluctuations shown in the inset.

The DOPC correlation function was normalized to the magnitude of the correlation function obtained for SBN associating to DOPC in order to compare their

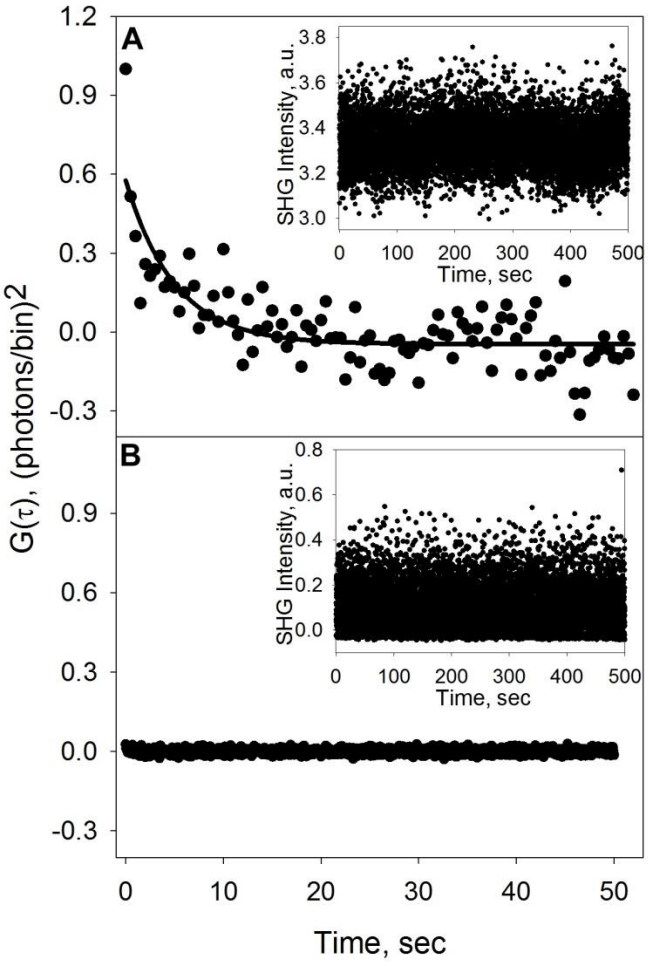

Figure 6.2. Autocorrelation data for A) SBN intercalating into a DOPC bilayer with fit to Eq. 6.7 indicated by the solid line and B) a pure DOPC bilayer normalized to the correlation function shown in A for comparison. Insets are representative examples of the measured fluctuations in SH signal that were used for the autocorrelation analysis.

relative magnitudes. No correlation from the DOPC bilayer or from photon shot noise was observed. This means the observed autocorrelation in Figure 6.2A is solely due to the surface binding kinetics of SBN to DOPC. The autocorrelation data of SBN intercalating into a DOPC bilayer, Figure 6.2A, were fit to Equation 5.17 with the parameters of N_s, k_{on}, and k_{off} and the results are given in Table 6.1. The adsorption and desorption rates from the nonlinear least-squares regression fit of Equation 5.17 are $2.7 \pm 0.1 \times 10^3\ M^{-1}s^{-1}$ and $9.0 \pm 4 \times 10^{-4}\ s^{-1}$, respectively. Using Equation 5.12 the equilibrium binding constant, K_0, is calculated to be $3.0 \pm 1.3 \times 10^6\ M^{-1}$. The large error seen in the predicted desorption rate is due to the high degree of correlation between the fitting parameters, N_s and k_{off}. To decouple the fitting parameters correlation data for multiple SBN concentrations could be measured and globally fit to obtain the k_{on}, and k_{off} or an independent desorption of SBN from the DOPC bilayer can be obtained to determine k_{off}. Here, the desorption of SBN from a DOPC bilayer was monitored over time after flushing the flowcell with excess PBS buffer (data shown in Figure 6.3). The resulting measured desorption rate is $4.0 \pm 1.4 \times 10^{-4}\ s^{-1}$. This rate determined from the desorption of SBN from the DOPC bilayer is statistically the same as the rate determined using the normalized correlation function in Equation 5.17, as well as the calculated K_0 of $6.8 \pm 2.4 \times 10^6\ M^{-1}$. The good agreement between the independently determined k_{off} value and that determined from SHCS demonstrates the ability of SHCS to accurately determine the adsorption and desorption rates simultaneously for molecules associating to a surface. Since these experiments were designed to show the feasibility of SHCS to determine surface binding kinetics, only one concentration well above the detection limit was used. However, a rough estimate of the sensitivity of SHCS can be made for the data

Table 6.1. Measured binding kinetics for SBN association to DOPC using SHCS and a typical binding isotherm including the surface adsorption rate (k_{on}), desorption rate (k_{off}) and equilibrium binding constant (K_0).

	$\boldsymbol{k_{on}}(\times 10^3 s^{-1}M^{-1})$	$\boldsymbol{k_{off}}(\times 10^{-4} s^{-1})$	$\boldsymbol{K_a}(\times 10^6 M^{-1})$
SHCS	2.7 ± 0.1	9 ± 4	3.0 ± 1.3
Isotherm	1.4 ± 0.4	6 ± 1	2.6 ± 0.2

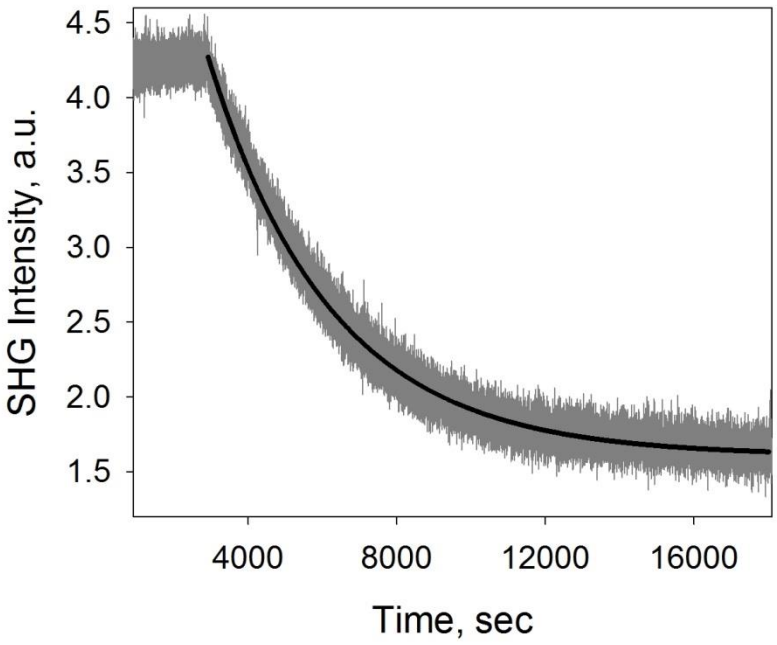

Figure 6.3. Desorption of SBN from a DOPC bilayer with a fit to an exponential decay indicated by the solid black line.

using the known sensitivity of the PMT detector, the measured background signal (before SBN has been added), the incident laser power at the surface and the known maximum surface excess of SBN, $2.6 \pm 0.3 \times 10^{13}\ molc \cdot cm^{-2}$ published by Conboy and Kriech.[19] The calculated limit of detection for SBN is 10 ± 1 femtomoles. This limit of detection is on the same order of magnitude as that obtained by Conboy and Kriech for SH spectroscopy.[19] It is important to remember this is only an approximation and as mentioned before the sensitivity of SHCS has not fully been investigated. Methods to improve the signal-to-noise ratio will significantly lower the limit of detection, and were discussed in Chapter 5.

The surface binding kinetics obtained here using SHCS were also compared to those obtained by Kriech and Conboy.[19] Although the adsorption rate, $5.7 \pm 3.8 \times 10^{3}\ M^{-1}$, reported by Kriech and Conboy is on the same order of magnitude as the adsorption rate obtained using SHCS, the desorption rate obtained using both SHCS and a simple desorption experiment is two orders of magnitude lower than the previously reported rate of $2.1 \pm 3.8 \times 10^{-2}\ s^{-1}$.[19] The discrepancy in k_{off} makes the calculated K_0 value obtained in the current study an order of magnitude higher than the value, $3.0 \pm 0.1 \times 10^{5}\ M^{-1}$, reported by Kriech and Conboy.[19] There are a few experimental differences, such as the type of lipid used and the incubation time allotted for SBN to bind to the PSLB, which could explain some of the difference between the k_{off} reported here and the k_{off} reported by Kriech and Conboy. However, the primary source for the discrepancy between the desorption values is most likely related to the substantial decrease in the limit of detection (~2 orders of magnitude smaller) of the SHG spectroscopy set up used here. The calculated limit of detection of the SHG apparatus

used in this chapter is 0.040 ± 0.005 femtomoles compared to 4.5 femtomoles reported by Kriech and Conboy.[19] The lower limit of detection seen here is a result of our notch filters having ~60% higher transmission efficiency at the SH wavelength of 266 nm and higher rejection in the visible region of the spectrum than those used by Kriech and Conboy. The lowest solution concentration of SBN that was detectable in this chapter was 43 nM (shown in Figure 6.5 inset), whereas Kriech and Conboy were only able to detect as low as 1 μM.[19] The ability to detect a lower concentration than 1 μM in the case of SBN associating to DOPC is extremely important as the resulting fit to the binding isotherm is drastically affected. It is important to note that the deviation from a linear response at very low bulk concentrations (< 50 nM) seen in the inset of Figure 6.5 is a result of approaching the limit of detection and not a deviation from a Langmuir isotherm as is apparent in the complete isotherm shown in Figure 6.5. Since 1 μM is at the very end of the linear region of the isotherm where the adsorption and desorption rates are highly dependent on the slope, there are not enough data to adequately determine the binding kinetics. In order to obtain more accurate binding kinetics, lower concentrations within the linear region of the binding isotherm must be obtained, as is possible in these studies.

6.4.2 Binding Kinetics of SBN Association to DOPC Using an SHG Binding Isotherm

In order to have a more accurate comparison for the SBN binding kinetics obtained using SHCS, an independent binding isotherm was obtained. The data were collected as a function of time at 10 min intervals for bulk SBN concentrations ranging

from 0.5 μm to 20.02 μm. To ensure that steady-state equilibrium had been reached at each concentration, multiple injections of the same concentration were made until there was no additional increase in SH signal. Although much lower concentrations (down to 43 nM) could be detected, it was unnecessary to start at such a low concentration as the concentration of 0.5 μM gave enough data in the linear region of the binding isotherm to obtain an accurate fit. The adsorption and desorption rates of SBN intercalating into a DOPC bilayer can be determined by assuming a Langmuir binding model where the SBN adsorption rate is first-order with respect to both the bulk SBN concentration, C_{bulk}, and the fraction of the unbound binding sites, (1-θ), and the desorption rate of SBN is first order with respect to the fraction of bound SBN, θ. The rate of change in the bound SBN is then given by Equation 3.13. The fraction of bound SBN, θ, is taken as the measured $\sqrt{I_{SHG}}$ divided by measured SH intensity at the saturation concentration, $\sqrt{I_{SHG}^{Max}}$. The SHG data for SBN intercalating into a DOPC bilayer in terms θ versus time for the concentration range of 0.50 μM to 20.02 μM are plotted in Figure 6.4. Since the SHG isotherm data were collected by consecutively increasing the bulk SBN concentration until saturation was reached in a single experiment without any desorption step in between consecutive concentrations, the initial time of each concentration was set to zero by setting the initial fraction of bound SBN equal to the calculated θ for the previous SBN concentration at saturation, as shown in Figure 6.4. The adsorption and desorption rate of the data were determined by simultaneously fitting all data in Figure 6.4 to Equation 3.14 as the same boundary conditions were used in this study as the one presented in Chapter 3.

The adsorption and desorption rates obtained from the nonlinear least-squares

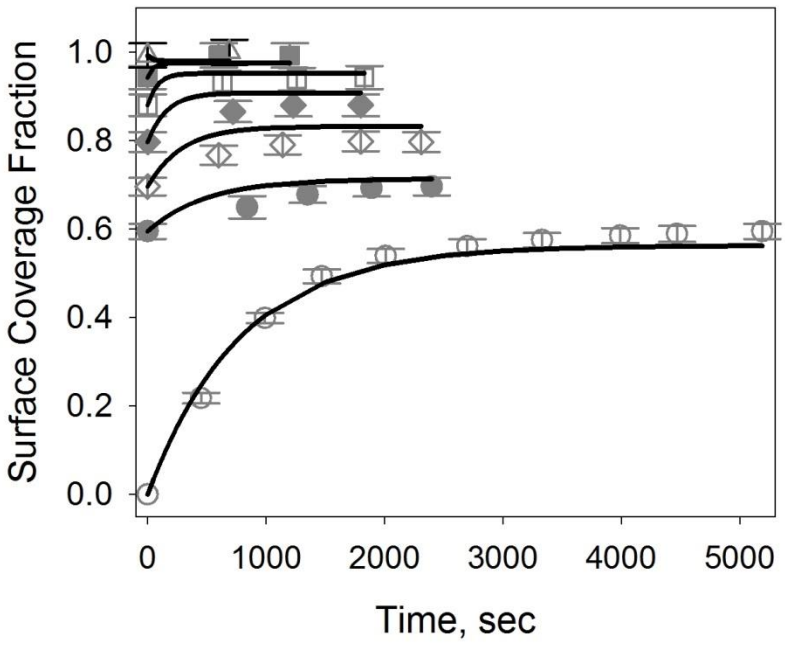

Figure 6.4. Fraction of surface coverage, θ, as a function of time for SBN intercalating into a DOPC bilayer measured at the following SBN bulk concentrations: 0.5 μM (open circles), 1.01 μM (closed circles), 2.01 μM (open diamonds), 4.0 μM (closed diamonds), 8.05 μM (open squares), 16.06 μM (closed squares), and 20.02 μM (open triangles). The solid lines represent the global fits to Eq. 3.14.

regression fit to Equation 3.14 are $1.4 \pm 0.4 \times 10^3\ s^{-1}M^{-1}$ and $5.6 \pm 1 \times 10^{-4}\ s^{-1}$, respectively, giving a K_0 of $2.6 \pm 0.2 \times 10^6\ M^{-1}$ (shown in Table 6.1). The values for k_{on}, k_{off}, and K_0 obtained using the kinetic isotherm data are in good agreement with those obtained using SHCS.

Next, a thermodynamic equilibrium binding isotherm was obtained by taking only the SH intensity value for each concentration at steady-state equilibrium (the last data point for each concentration in Figure 6.4). The thermodynamic binding isotherm obtained for SBN intercalating into a DOPC bilayer is shown in Figure 6.5. The SH intensity increases with increasing concentration of SBN until it reaches saturation of the binding sites in the PSLB. The SH intensity is normalized and the errors are from 3 separate experiments. Assuming a Langmuir binding model, the SH signal can be expressed by Equation 3.9. The equilibrium binding constant, K_0, determined from the fit to Equation 3.9 is $2.4 \pm 0.2 \times 10^6\ M^{-1}$. This value is in good agreement with the K_0 obtained using SHCS.

6.4.3 Comparison Between SHCS and SHG Binding Isotherms

The good agreement between the results obtained from SHCS and those measured via a classic adsorption isotherm, demonstrates the validity of using SHCS to determine the binding kinetics of molecules at a surface. Additionally, the time required to collect the SHCS data was much shorter than the time required to collect the binding isotherm data. For example, the autocorrelation data collection took less than 2 hrs, whereas one binding isotherm of SBN took 6 hrs to complete. Moreover, multiple injections of SBN were not necessary over the course of the collection of the SHCS data as compared to the

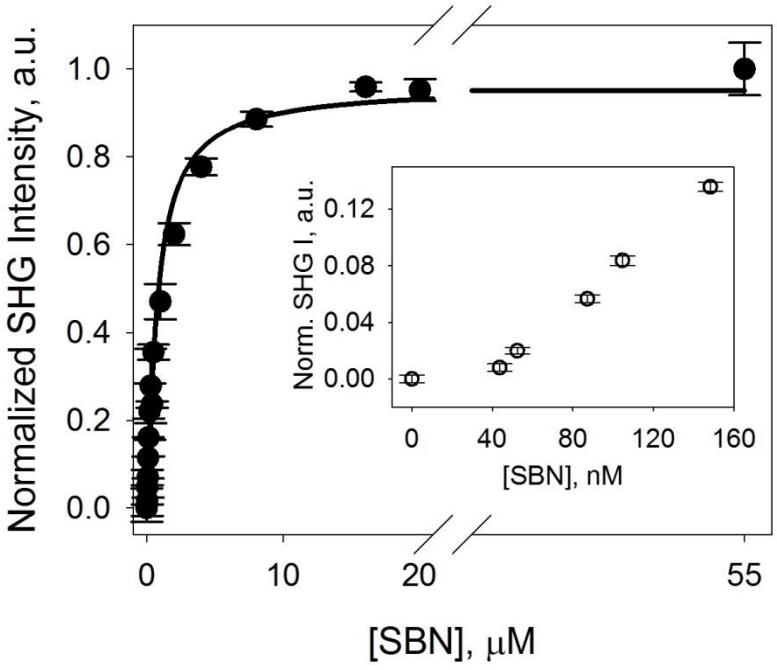

Figure 6.5. SH intensity of SBN intercalated into a DOPC bilayer versus bulk SBN concentration. The solid line is the fit to the Langmuir model (Equation 3.9) and the error bars represent the standard deviation from the SHG measurement. Inset is an enlargement of the bulk SBN concentrations in the nM region.

isotherm data where an injection was made every 10 mins to compensate for bulk SBN depletion and to allow kinetic information to be determined. Another advantage of SHCS is the simultaneous determination of both the adsorption and desorption rates using only a single concentration of analyte. It is true that determining the desorption rate in a separate experiment provides a statistically better fit to the correlation data; however, since the desorption rate determined separately was within error of the desorption rate from SHCS, it is still possible to determine both the adsorption and desorption rate using a single analyte concentration with SHCS given N_s can be approximated. Alternatively, if additional SBN concentrations were also examined using SHCS, a global fit to all concentrations would provide a statistically better fit to the correlation data and more accurate kinetic information could be obtained without requiring the desorption rate to be determined separately. In addition to the advantages over conventional isotherm studies, SHCS also offers several advantages over the more commonly used FCS method. The most obvious advantage is that no exogenous label is required to obtain the data. This eliminates many obstacles seen with FCS, such as problems associated with photobleaching, and the unavoidable contribution from solution phase species to the observed fluctuations. In addition, the ability of SHCS to only detect the molecules bound to the surface simplifies the correlation function used to retrieve the binding kinetics as compared to FCS because diffusion of molecules in solution can be neglected, which leaves only the surface binding kinetics of molecules contributing to the fluctuations seen in the SH signal. These advantages make SHCS an attractive and efficient method to directly determine the binding kinetics of molecules at a surface.

6.5 Summary

In this chapter the binding kinetics of SBN intercalating into a DOPC planar supported lipid bilayer were investigated using both a traditional binding isotherm and SHCS. The adsorption and desorption rates, as well as the equilibrium binding constant, determined using both methods were statistically identical within the 99% confidence interval. These results demonstrate the validity of using the surface specific, label-free and coherent method of SHCS to examine biomolecular interactions at a surface. Although the desorption rate was obtained *a priori* in order to decouple the autocorrelation fitting parameters and reduce the error in the resulting values, it is not wholly necessary. As mentioned earlier, collection of autocorrelations for several SBN concentrations could also provide the k_{on}, and k_{off} as well as provide any dependence the binding kinetics might have on bulk concentration. This approach is more thoroughly discussed in Chapter 7. The lower total analyte quantity required and the reduced time to obtain the surface binding kinetics makes SHCS an attractive analytical tool for many bioanalytical systems where analyte and time are often scarce. Moreover, the surface specificity, label-free nature, and large coherence length of SHCS eliminate some of the challenges seen in FCS due to fluorophores and diffusion of molecules in bulk solution. Since the only contribution to the fluctuations in SH is from surface associated molecules, SHCS data analysis is greatly simplified. The simplicity and efficiency of SHCS makes it a new and valuable technique to directly and precisely ascertain the binding kinetics of molecules at a surface without a label.

6.6 References

(1) R.Lakowicz, J.;*Topics in Fluorescence Spectroscopy*; Plenum Press, 1991; Vol. Volume 1.

(2) Fahey, P. F.; Koppel, D. E.; Barak, L. S.; Wolf, D. E.; Elson, E. L.; Webb, W. W. *Science* **1977**, *195*, 305-306.

(3) Andries, C.; Guedens, W.; Clauwaert, J.; Geerts, H. *Biophys. J.* **1983**, *43*, 345-354.

(4) Palmer, A. G., III; Thompson, N. L. *Proc. Natl. Acad. Sci. U. S. A.* **1989**, *86*, 6148-6152.

(5) Petersen, N. O.; Johnson, D. C.; Schlesinger, M. J. *Biophys. J.* **1986**, *49*, 817-820.

(6) Borejdo, J. *Biopolymers* **1979**, *18*, 2807-2820.

(7) Lieto, A. M.; Cush, R. C.; Thompson, N. L. *Biophys. J.* **2003**, *85*, 3294-3302.

(8) Thompson, N. L.; Axelrod, D. *Biophys. J.* **1983**, *43*, 103-114.

(9) Hansen, R. L.; Harris, J. M. *Anal. Chem.* **1998**, *70*, 4247-4256.

(10) Hansen, R. L.; Harris, J. M. *Anal. Chem.* **1998**, *70*, 2565-2575.

(11) Bismuto, E.; Gratton, E.; Lamb, D. C. *Biophys. J.* **2001**, *81*, 3510-3521.

(12) McCain, K. S.; Schluesche, P.; Harris, J. M. *Anal. Chem.* **2004**, *76*, 930-938.

(13) Ruckstuhl, T.; Krieg, A. *Anal. Chem.* **2005**, *77*, 2656-2661.

(14) Maiti, S.; Haupts, U.; Webb, W. W. *Proc. Natl. Acad. Sci. U. S. A.* **1997**, *94*, 11753-11757.

(15) Gassin, P.-M.; Martin-Gassin, G.; Benichou, E.; Brevet, P.-F. *J. Phys. Chem. C* **2014**, *118*, 1135-1141.

(16) Zhao, X.; Goh, M. C.; Subrahmanyan, S.; Eisenthal, K. B. *J. Phys. Chem.* **1990**, *94*, 3370-3373.

(17) Zhao, X.; Eisenthal, K. B. *J. Chem. Phys.* **1995**, *102*, 5818-5826.

(18) Yan, E. C. Y.; Eisenthal, K. B. *J. Phys. Chem. B* **2000**, *104*, 6686-6689.

(19) Kriech, M. A.; Conboy, J. C. *Appl. Spectrosc.* **2005**, *59*, 746-753.

(20) Kriech, M. A.; Conboy, J. C. *J. Opt. Soc. Am. B: Optical Physics* **2004**, *21*, 1013-1022.

CHAPTER 7

DETERMINATION OF MULTIVALENT PROTEIN-LIGAND BINDING KINETICS USING SECOND HARMONIC CORRELATION SPECTROSCOPY

Reprinted (adapted) with permission from Sly, K. L. and Conoby, J.C. *Anal. Chem.* ***2014,*** *85,* 11045-1105.

7.1 Introduction

In Chapter 6, SHCS accurately detected the binding kinetics of the small molecule SBN intercalating into a DOPC bilayer. This simple monovalent system demonstrated the potential of using SHCS to examine surface binding kinetics for a single analyte concentration. To further probe the sensitivity and scope of SHCS, in this chapter a more complex binding system involving multivalent protein-ligand interactions at the surface of PSLBs is investigated using SHCS. As mentioned in Chapter 3, the binding kinetics of multivalent protein-ligand interactions often show a dependence on the bulk protein concentration. The ability of SHCS to examine the surface binding kinetics for a single analyte concentration allows multivalent protein-ligand interactions to be examined in more detail. As such, in this chapter the binding kinetics of two multivalent protein-ligand pairs for several protein concentrations are determined using SHCS.

Multivalent protein binding interactions have attracted much attention in biomolecule detection, biological separations, biosensors and immunological assays.[1-6] Multivalent protein-ligand interactions have shown stronger binding, reduced non-specific interactions, and increased aggregation on surfaces relative to monovalent interactions.[4,5,7,8] Multivalent protein-carbohydrate interactions in particular have a significant biological role in cell trafficking and recognition,[9] pathogen attachment and uptake,[1,10] and tumor cell differentiation based on glycolipid/glycoprotein expression.[11,12] Although the diverse cellular and analytically beneficial binding properties have led to much research on multivalent protein-ligand interactions, there is still much that is not understood about their complex binding properties, especially at surfaces.[4]

Most multivalent protein-carbohydrate interactions continue to be analyzed with simple binding models that operate under the assumption that binding is reversible and each binding event occurs independently without ligand-ligand or protein-protein interactions.[4,13] Many studies have shown the interactions between multivalent proteins and carbohydrates are indeed cooperative in nature[7,8] with strong ligand-ligand and/or protein-protein interactions that affect the apparent binding affinity. Only a few studies have examined the binding affinities as a function of ligand density[7] and even fewer studies have investigated the dependence of the binding affinity on protein concentration.[14] These previous studies suggest that multivalent protein-carbohydrate interactions are far more intricate than simple binding models alone can predict. The ability to more efficiently and precisely measure the binding kinetics of these multivalent protein-carbohydrate interactions will provide further understanding of the binding properties of these complex interactions. Such information would allow for more

effective design of biosensors and drugs that utilize multivalent protein-ligand interactions. Two proteins that can be used as archetypes to examine the influences of protein concentration, cooperative behavior, and electrostatics on the complex binding properties of multivalent protein-ligand interactions are cholera toxin (CT) and peanut agglutinin (PnA). CT and PnA are both commonly used in biosensors and medical diagnostics due to their highly specific interaction with the most abundant ganglioside in cell membranes, GM_1, making further investigation of the binding properties of these multivalent interactions particularly biologically valuable.

CT, a pathogen secreted from the bacterium *Vibrio Cholerae*, is an AB_5 cytotoxin composed of a central A subunit surrounded by five identical B subunits that form a pentameric ring.[7] It is the CT B subunit (CTb) that is responsible for binding to the cell surface via the pentasaccharide moiety of the ganglioside GM_1.[15] Following the attachment of the B subunits to the cell membrane, the toxic A subunit enters the cell and causes an elevated level of cAMP in the small intestines that leads to fluid loss.[22] A myriad of techniques including fluorescence,[2,3,7] SPR,[16,17] ELISA,[1] and differential scanning calorimetry,[8] have been implemented to examine the specific binding kinetics of the CTb-GM_1 interaction. Although most of the studies have shown CTb exhibits almost no nonspecific interactions to membranes without GM_1, the reported specific binding affinities range from 10^6 M^{-1} to 10^{11} M^{-1}.[2,3,7,16,17] Some of this disparity may be attributed to experimental differences such as ligand density, incubation time, and mass transport limitations. Several studies have found the Hill-Waud model, a cooperative binding model that accounts for cooperative behavior between ligand molecules, to more accurately describe the CTb-GM_1 interactions as compared to the more common

Langmuir model.[2,7] However, many studies which examine the CTb-GM_1 at low nM concentrations in order to determine the cooperative behavior require extremely long incubation periods to obtain an accurate steady-state response. As such, inconsistent and lower binding affinities are often measured because the data obtained was limited by mass transport.[18] A method that can measure CTb binding to GM_1 for several CTb bulk concentrations after steady-state equilibrium has been reached would eliminate mass transport effects and provide the binding kinetics as a function of bulk CTb concentration.

Similar to CTb, the multivalent carbohydrate binding lectin PnA has been extensively used in bioanalytical assays; however, its binding properties to various carbohydrate moieties are usually only qualitatively examined and have been less frequently quantified. Peanut agglutinin (*arachis hypogaea* agglutinin) is a tetrameric lectin that binds specifically to terminal D-galactosyl groups.[6,19] This carbohydrate-free protein is known for its anti-T activity and is routinely used in serology to monitor polyagglutinability.[6,20,21] Its high specificity for galactosyl groups with a decrease in affinity from Galβ1,3GalNAc to $GalNH_2$ to Gal, has made PnA a useful aid in characterizing the specific glycoprotein/glycolipid expression on the cell surface of malignant cancer cells.[6,12] The widespread use of PnA as a biochemical tool for carbohydrate separation has made it the subject of much research.[4,13,19] Techniques such as carbon NMR,[19,22] ELISA,[5,23] fluorescence,[20] and ultraviolet difference spectroscopy[24] have been used to determine the binding properties of PnA to various carbohydrate groups, gangliosides, and glycolipids. However, very few of these studies have moved beyond the traditional Langmuir binding model used to determine the thermodynamic

binding affinity for monovalent interactions and, to the authors' knowledge, there is no study on the dependence of the binding kinetics on bulk PnA concentration. While previous studies have shown the highly specific nature of the PnA-GM_1 interaction, investigating the binding kinetics of PnA to GM_1 as a function of PnA concentration would provide additional valuable information on the intricate binding properties of this multivalent binding complex.

In this chapter the multivalent interactions of CTb and PnA to GM_1 doped into a PSLB are investigated using SHCS. PSLBs were chosen as the binding platform as they mimic the native cell surface where GM_1 is present, reduce nonspecific binding and allow precise control over the GM_1 density.[25] The SHCS technique used for these studies offers the advantage of determining the binding kinetics at individual protein concentrations using minimal analyte and, most importantly, under steady-state equilibrium to reduce mass transport effects. SHCS has previously been used to determine the diffusion of large dye molecules and amphiphilic head groups of long hydrocarbon chains.[26-28] In Chapter 6 SHCS was used to accurately determine the binding kinetics of the small molecule SBN intercalating into a PSLB.[29] The study presented in this chapter is the first to extend the SHCS technique to the detection and investigation of protein binding at a surface. Using SHCS to measure the binding kinetics separately for several bulk protein concentrations, as well as examining the cooperative and electrostatic contributions of these multivalent protein-ligand interactions, provides additional insight for their use in biosensors, medical diagnostics and drug development.

7.2 Experimental Design

7.2.1 Materials

DOPC, Rh-DOPE and GM_1 from ovine brain were purchased from Avanti Polar Lipids and used as received. The structure of DOPC is shown in Figure 3.1, Rh-DOPE is shown in Figure 4.3 and the structure of GM_1 is shown in Figure 7.1. Immunoglobulin G from Rabbit serum (IgG), Cholera Toxin B Subunit from *Vibrio cholera* (CTb), and *arachis hypogaea* from peanut agglutinin (PnA) were obtained from Sigma-Aldrich. The water, PBS buffer, and fused silica prisms are the same as described in section 3.2.1. Both CTb and PnA were dissolved in PBS pH 7.4 to the desired working concentrations (0.22 nM to 240 nM for CTb and 0.43 μM to 12.02 μM for PnA).

7.2.2 PSLB Formation

The DOPC lipids used in these experiments were dissolved in chloroform and doped with GM_1 that had been dissolved in a 1:1 chloroform:methanol mixture. The GM_1 density was chosen such that there would be a monolayer of protein at the surface when the binding sites had been saturated (1 mol % for CTb and 5 mol % for PnA). PSLBs of GM_1 doped DOPC were formed on a silica prism using vesicle fusion as described in section 3.2.3. Excess PBS was flushed through the flowcell to remove any unbound lipids in solution. To screen any possible defects on the bilayer and prevent nonspecific binding of the proteins, the PSLBs were incubated with IgG for 30 mins and then rinsed with PBS to remove any unbound IgG in solution.

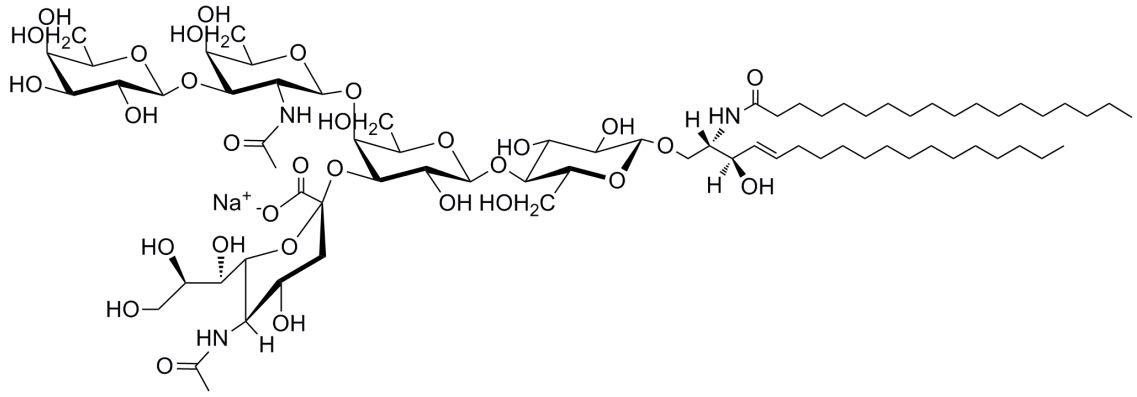

Figure 7.1. Chemical structure of GM_1 ganglioside.

7.2.3 SHG Measurements

Counter-propagating SHG was used for these experiments and is described in detail in Chapter 2. The second harmonic output used in this chapter is the same as that described in section 6.3.3 with the same energy per pulse, beam diameter, notch filters and detector. The SH intensity is described by Equations 2.15 and 2.16, which illustrate the possible enhancement in SH intensity when the incident (ω) or SH (2ω) frequency is resonant with an electronic transition of a molecule at the surface. With this resonant enhancement, very low concentrations of molecules at the surface can be detected using SH spectroscopy. This means that if the analyte being detected has an electronic transition at the frequency of the SH light there will be a lower limit of detection (LOD) and increased sensitivity.[30] Here, a fundamental wavelength of 532 nm is used such that the resulting SH wavelength is 266 nm, which is in resonance with the electronic transition of the tryptophan and tyrosine residues in the proteins used in this chapter (shown in Figure 7.2). The signal enhancement from this resonance allows detection down to low nM concentrations of CTb and μM concentrations of PnA, giving LODs of 0.20 ± 0.03 fg/cm^2 and 9.1 ± 1.2 pg/cm^2, respectively. These LODs are similar to those reported using fluorescence and lower than those reported using QCM to monitor the binding of these proteins to immobilized ligand surfaces.[7,13]

7.2.4 SHCS Data Collection

SHCS has been described in detail in Chapter 5. Similar to Chapter 6, the fluctuations in the SH signal are measured as a function of time and autocorrelated to determine the reaction rate of the surface binding kinetics occurring within the detection

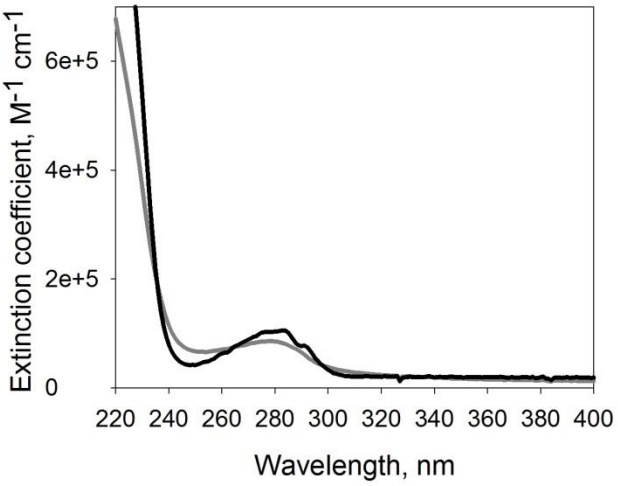

Figure 7.2. Extinction coefficient spectra of CTb (gray) and PnA (black).

area. SHCS data were collected for the proteins associating to GM_1 doped into a DOPC bilayer at three separate bulk protein concentrations after steady-state equilibrium had been reached. Data were collected for every pulse of the laser so that the time interval between data points was dictated by the 20 Hz (50 ms) repetition rate of the laser. The fast Fourier transform multiplied by its complex conjugate was determined for 20 data sets each consisting of 5,000 data points. Once averaged the inverse Fourier transform was performed to obtain the correlation time constant of the data. To extrapolate the reaction rate, including the adsorption and desorption rate, for the binding kinetics of CTb-GM_1 and PnA-GM_1, the normalized correlation function for a typical reversible biomolecular interaction described in Equation 5.17 was used.

7.2.5 SHG Adsorption Isotherm Data Collection

Binding isotherms of the proteins associating to GM_1 doped in DOPC bilayers were performed in duplicate for CTb and triplicate for PnA. Any changes in the laser power between experiments were compensated for by performing a two-point normalization to a 10 mM KOH solution and a solution of PBS pH 7.4, followed by subtraction of the background SH intensity before any protein was added. The SH intensity was monitored over time as increasing concentrations of the proteins were injected and allowed to reach equilibrium between the bulk solution and bilayer. The depletion of the bulk protein concentration as proteins bound to the surface was offset by injecting a fresh solution of the same protein concentration every 10 mins until a steady-state response was reached. For the lowest concentration of CTb it required up to 14 hrs to reach steady-state equilibrium. Since the lowest concentration of PnA was in the μM

range the time required to reach equilibrium was shortened to 2 hrs. Each data point collected was averaged for 100 samples and integrated using a boxcar. To prevent damage to the bilayer from exposure to the laser, the SH intensity was recorded at 5-10 min intervals for 2-3 mins and then blocked. The thermodynamic equilibrium binding constant was determined from an isotherm consisting of only the SH intensity collected at steady-state equilibrium for each protein concentration.

7.2.6 Hill-Waud Adsorption Isotherm Equation

The SH intensity is proportional the sum of the real and imaginary portions of the resonant susceptibility tensor as shown in Equation 3.2. If there are multiple identical binding sites and ligand-ligand interactions, the surface adsorption of the protein is described by the Hill-Waud model where the surface density N in equation 3.2 is given by,

$$N = \frac{N_{max} K_0^n [P]^n}{1 + K_0^n [P]^n}, \tag{7.1}$$

where N_{max} is the maximum surface density at saturation, K_0 is the equilibrium binding constant, $[P]$ is the bulk protein concentration, and n is the Hill coefficient, which describes the affinity of the protein for its ligand when another ligand is already bound. When $n > 1$ there is an increase in the affinity of the protein for its ligand once another ligand is bound (positive cooperativity) and when $n < 1$ there is a decrease in the affinity of the protein for its ligand once another ligand is bound (negative cooperativity).[7]

Using the relationship between the surface density and the SH intensity, $I_{SHG} \propto N^2$, and subtracting the background SH intensity, $I_{SHG}^{background}$, designated as A, the SH intensity from the adsorption of a protein in terms of the Hill-Waud model can be

expressed by the following:

$$I_{SHG} - I_{SHG}^{background} \propto 2B\sqrt{I_{SHG}^{background}}\left(\frac{\sqrt{I_{SHG}^{max}}K_a^n[P]^n}{1+K_a^n[P]^n}\right) + (B^2 + C^2)\left(\frac{\sqrt{I_{SHG}^{max}}K_a^n[P]^n}{1+K_a^n[P]^n}\right)^2. \quad (7.2)$$

Since the SH signal is on resonance with an electronic transition of CTb and PnA (Figure 7.2), B is much smaller than the imaginary portion of the resonant susceptibility tensor, making (B^2 + C^2) much greater than the cross-term $2B\sqrt{I_{SHG}^{background}}$.[31] Additionally, ($B^2$ + C^2) relates to the surface density of molecules and can therefore be combined with $\sqrt{I_{SHG}^{max}}$. Using these simplifications, the SH intensity in terms of the Hill-Waud model is expressed as,

$$I_{SHG} \propto \left(\frac{\sqrt{I_{SHG}^{max}}K_a^n[P]^n}{1+K_a^n[P]^n}\right)^2. \quad (7.3)$$

7.3 Results and Discussion

7.3.1 Binding Kinetics of CTb-GM_1 Using SHCS

The binding affinity for CTb and PnA binding to GM_1 were examined as a function of bulk protein concentration using SHCS. After an appropriate incubation time for a steady-state response to be reached the SH signal was collected for every pulse of a 20 Hz laser as a function of time for 3 bulk concentrations of CTb (0.5 nM, 13 nM, and 240 nM) binding to a 1 mol% GM_1 doped DOPC lipid bilayer (data shown as insets of Figures 7.3A, 7.4A, and 7.5A). The SH signal was cross-correlated with itself to extract

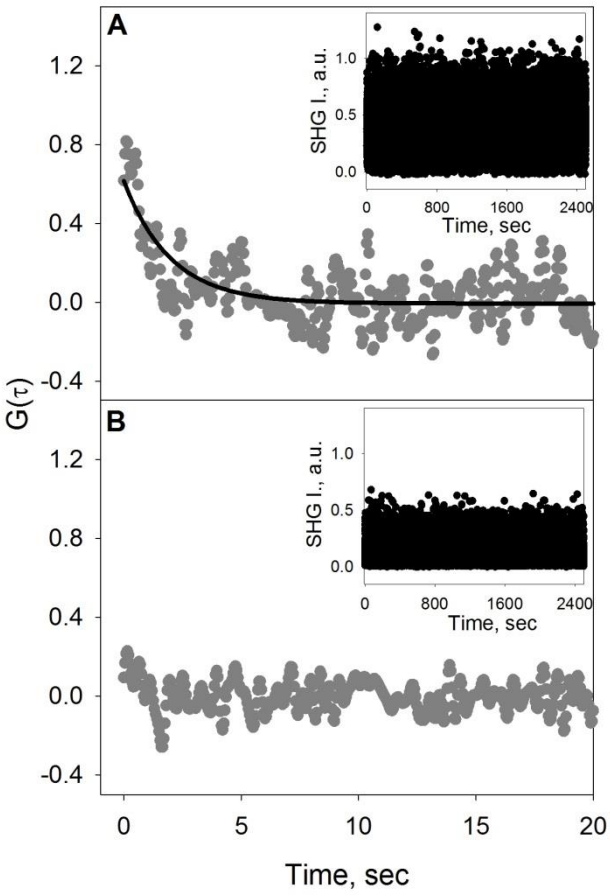

Figure 7.3. Autocorrelation data for 0.5 nM CTb binding to (A) 1 mol % GM_1 doped into a DOPC bilayer (B) a pure DOPC bilayer. The solid black line represents the fit to Equation 5.17. The nonspecific CTb correlation function in (B) has been normalized to the specific binding autocorrelation data in (A).

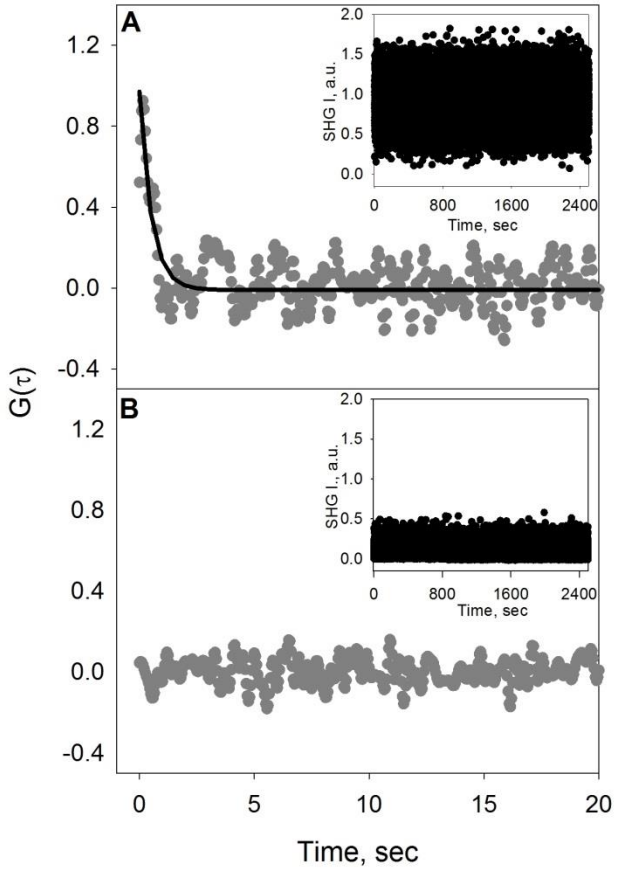

Figure 7.4. Autocorrelation data for 13 nM CTb binding to (A) 1 mol % GM_1 doped into a DOPC bilayer (B) a pure DOPC bilayer. The solid black line represents the fit to Equation 5.17. The nonspecific CTb correlation function in (B) has been normalized to the specific binding autocorrelation data in (A).

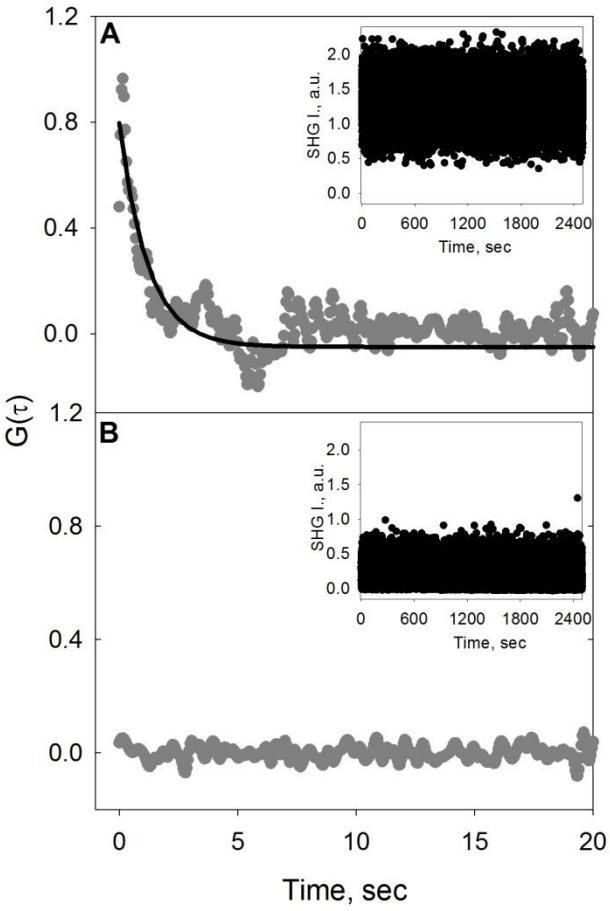

Figure 7.5. Autocorrelation data for 240 nM CTb binding to (A) 1 mol % GM_1 doped into a DOPC bilayer (B) a pure DOPC bilayer. The solid black line represents the fit to Equation 5.17. The nonspecific CTb correlation function in (B) has been normalized to the specific binding autocorrelation data in (A).

the correlated molecular binding kinetics. As most of the fluctuations seen in the SH signal are uncorrelated noise, these high frequency contributions (filtered at 15 times the Nyquist limit) and the first point of the autocorrelation were removed.[32] The resulting normalized correlation data, $G(\tau)$, from the average of 20 data sets for each of the 3 CTb concentrations binding to a 1 mol% GM_1 doped DOPC lipid bilayer are shown in Figures 7.3A, 7.4A and 7.5A. SHCS data were also collected for the nonspecific binding of CTb where each of the 3 CTb concentrations was exposed to a DOPC bilayer that did not contain GM_1. The normalized correlation data of 20 averaged data sets are shown for each of the 3 CTb concentrations binding to a pure DOPC bilayer in Figures 7.3B, 7.4B, and 7.5B. To allow comparison between the noise of the specific and nonspecific correlation data, the time zero point of the autocorrelation of the nonspecific binding of CTb was normalized to the time zero point of the correlation data of the specific binding of CTb to a 1 mol% GM_1 doped DOPC bilayer for each of the respective CTb concentrations. It is important to note that before normalization the magnitude of the noise of the nonspecific binding correlation data remained the same for all three nonspecific correlation data as the mean SH intensity is the same with no apparent increase in signal as protein is added. It is apparent from the nonspecific autocorrelation data that there is no appreciable nonspecific binding as there is no correlation seen, meaning the correlated events giving rise to $G(\tau)$ in Figures 7.3A, 7.4A, and 7.5A all arise from the specific binding interactions between CTb and 1 mol% GM_1. The lack of correlated events in Figures 7.3B, 7.4B, 7.5B when GM_1 is not present in the bilayer also emphasizes that correlated proportional noise from the laser and/or vibrations from the optics are not contributing to the observed correlations seen in Figures 7.3A, 7.4A, and

7.5A as these contributions would be seen in the nonspecific correlation data if they were present.[33,34] Additionally, in Chapter 6 the specific correlation function of SBN intercalating into a DOPC bilayer displayed a much longer time constant (~6 times) than seen here, which would presumably be the same if the same source (laser or optics) were contributing to the correlated events.[29] In Chapter 6 it was also shown that the correlation function of a pure DOPC bilayer without addition of any molecule displayed no correlated events, further demonstrating the absence of correlated proportional noise or correlated noise from the bilayer.[29]

SHCS has previously been used to measure the translational and/or rotational diffusion of dye molecules and hydrocarbon chain substituted amphiphiles on surfaces.[26-28] In order to rule out the possibility of rotational and translational motion on the observed dynamics presented in Figures 7.3A, 7.4A and 7.5A, the time scale of such events was considered for the experimental conditions used in this chapter. For example, an FCS study of the rotational diffusion of antimicrobial peptides found that the correlation function time constant was nanoseconds.[35] This is much faster than the 50 ms time interval used in this chapter, meaning the correlation data collected here are insensitive to these fast dynamics as described in detail in Chapter 5. In another FCS study the translational diffusion of CTb bound to GM_1 doped lipids was investigated and the correlation function time constant of 6 ms was reported for a spot size of 50 nm.[36] Using fluorescence recovery after photobleaching (FRAP) Kelly and coworkers determined the diffusion coefficient of CTb in a lipid bilayer to be 0.12 ± 0.03 $\mu m^2/sec$.[36] Assuming Brownian diffusion, CTb would be expected to take a time, t, to diffuse a mean squared distance, r, according to $t = r^2/4D$. For the spot size used in this chapter of ~ 1

mm^2 it would take CTb approximately 2.5×10^6 sec to diffuse through the illumination area. Consequently, this much slower rate compared to the binding kinetics observed in Figures 7.3A, 7.4A, and 7.5A would not contribute to the correlation data presented here.

The correlation data for the specific binding of CTb to 1 mol% GM_1 doped into a DOPC bilayer were fit to Equation 5.17 with the parameters k_{on}, k_{off}, and N_c. The results of the nonlinear least squares regression of the data in Figures 7.3A, 7.4A, and 7.5A to Equation 5.17 are shown in Table 7.1. The measured adsorption rate decreased with increasing protein concentration from $1.0 \pm 0.1 \times 10^9\ M^{-1}s^{-1}$ when only 0.5 nM CTb is present to $1.5 \pm 0.01 \times 10^8\ M^{-1}s^{-1}$ for 13 nM CTb to $3.5 \pm 0.2 \times 10^6\ M^{-1}s^{-1}$ for 240 nM CTb. The decrease in the adsorption rate with increasing CTb concentration seen in the SHCS data might be explained in terms of electrostatics using the electrostatic map of CTb shown in Figure 7.6. The binding plane surface of CTb is positively charged and would be greatly attracted to the negatively charged terminal sialic acid of GM_1, leading to the rather fast adsorption rate seen here for low concentrations of CTb. However, as more CTb is bound to the surface, the neutral top plane of bound CTb would be exposed to incoming CTb molecules and essentially screen the negatively charged sialic acids at the membrane surface. The attraction between the negative sialic acid and the binding plane of CTb would lessen as more CTb binds, which would lead to a slower rate of adsorption as the concentration of CTb increased.

The results seen for the 240 nM CTb-GM_1 interaction are similar to the k_{on} value reported in an SPR study by Kuziemko and coworkers ($1.27 \times 10^6\ M^{-1}s^{-1}$)[16] where the binding of 120 nM – 240 nM CTb to a 5 mol % GM_1 doped lipid bilayer was investigated, suggesting that SHCS can accurately predict the adsorption rate for the

Table 7.1. Measured binding kinetics for CTb binding to a GM_1 doped DOPC bilaer using SHCS including the adsorption rate (k_{on}), desorption rate (k_{off}), and equilibrium binding affinity (K_0).

	[CTb] (nM)	k_{on} *(×* 10^8 $M^{-1}s^{-1}$*)*	k_{off} *(×* 10^{-5} s^{-1}*)*	K_0 *(×* 10^{12} M^{-1}*)*
SHCS	0.5	10 ± 1	3.6 ± 0.5	28 ± 5
	13	1.50 ± 0.01	3.2 ± 0.4	4.7 ± 0.7
	240	0.035 ± 0.002	2.5 ± 0.2	0.14 ± 0.01

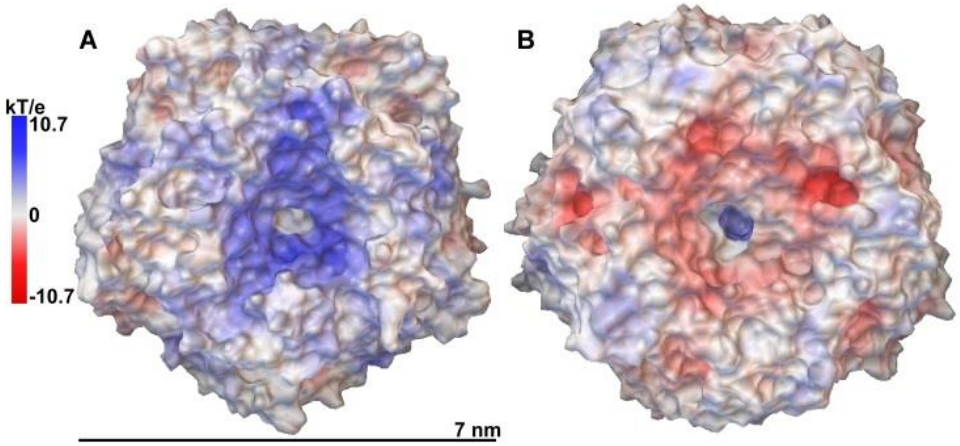

Figure 7.6. Electrostatic potential map of CTb (PDB: 1PZJ) calculated in Python Molecular Viewer from Scripps MGL tools assuming a 150 mM salt concentration[37] for the binding plane (A) and top plane (B) where red indicates negative potential, white is neutral and blue is indicative of positive potential.

CTb-GM_1 complex. It is important to note that the authors' in the SPR study took extreme precaution to make sure mass transport did not limit or affect the binding kinetics and as such collected their CTb-GM_1 binding data under steady-state conditions.[16] The SHCS was not only collected after steady-state equilibrium had been reached (up to 16 hrs at 0.5 nM CTb), but also the SHCS analysis of the kinetics is inherently minimally affected by mass transport as the diffusion of the protein molecules to the surface occurs at a much longer time scale (10^{-8} cm^2 s^{-1})[38] compared to the binding kinetics. As has been done in FCS, the difference in time scale can be used to separate out the contributions from binding kinetics and diffusion.[39-41] The SHCS data and the data collected by Kuziemko and coworkers produce similar adsorption rates as both were collected under steady-state conditions where mass transport did not affect the measured binding kinetics.

The desorption rate for CTb concentrations of 0.5 nM, 13 nM, and 240 nM obtained from the fit to Equation 5.17 were $3.6 \pm 0.5 \times 10^{-5}\ s^{-1}$, $3.2 \pm 0.4 \times 10^{-5}\ s^{-1}$, and $2.5 \pm 0.2 \times 10^{-5}\ s^{-1}$, respectively. The desorption rates were all in good agreement with each other and did not significantly change with CTb concentration. To further verify the SHCS results a desorption experiment for all 3 CTb concentrations was performed by flowing excess PBS buffer through the flowcell and monitoring the SH intensity over time (data shown in Figure 7.7). It is important to note that the slight shift in the desorption data are a result of an electronic baseline shift and not from the desorption of CTb from GM_1. The desorption rate of CTb from GM_1 was found to remain relatively constant with increasing CTb concentration from $3.07\pm 0.02 \times 10^{-5}\ s^{-1}$ at 0.5 nM CTb to $3 \pm 1 \times 10^{-5}\ s^{-1}$ at 13 nM to $3.6 \pm 0.8 \times 10^{-5}\ s^{-1}$ at 240 nM. Additionally, all desorption

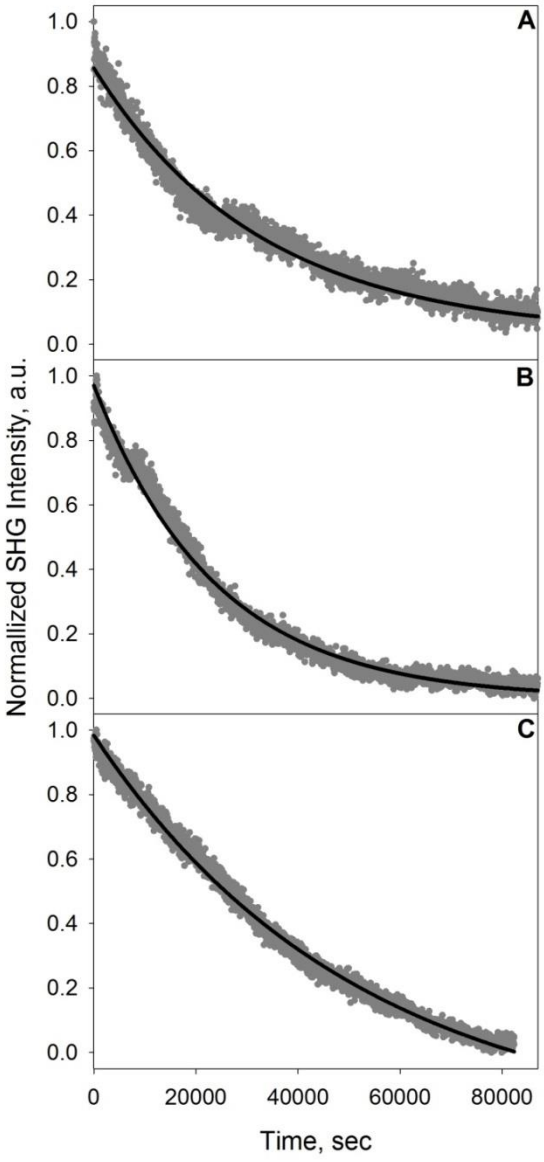

Figure 7.7. SH intensity vs. time of the desorption of CTb bulk concentration 0.5 nM (A), 13 nM (B), and 240 nM (C). Solid lines are the fits to an exponential decay.

rates are close to those predicted using SHCS. The good agreement of the SHCS desorption rates and those obtained through a separate desorption experiment confirm the ability of SHCS to predict accurate binding kinetics for surface protein-ligand interactions. To further verify the predicted k_{on} obtained using SHCS and to decouple the closely related fitting parameters of Equation 5.17, the values obtained from the separate desorption experiment were fixed as k_{off} in 5.17 and the nonlinear regression was run with only two parameters, k_{on} and N_s. The results produced the same values (within error) for k_{on} and N_s as those shown in Table 7.1, which were determined for the three parameter fit, albeit with smaller error. Thus, although it is not wholly necessary to determine the desorption rate separately to obtain accurate binding kinetics using SHCS, it does lower the error and is a simple way to confirm the SHCS predicted binding kinetics, especially when N_s can only be approximated.

The equilibrium binding affinity was calculated from the adsorption and desorption rates determined from the SHCS data in Figures 7.3A, 7.4A, and 7.5A using Equation 5.12 and the results are shown in Table 7.1. The K_0 decreased with increasing CTb concentration from $2.8 \pm 0.5 \times 10^{13}\ M^{-1}$ at 0.5 nM CTb to $4.7 \pm 0.7 \times 10^{12}\ M^{-1}$ at 13 nM CTb to $1.4 \pm 0.1 \times 10^{11}\ M^{-1}$ at 240 nM CTb. The K_0 determined here for 240 nM CTb binding to GM_1 is in good agreement with the SPR study by Kuziemko and coworkers for the CTb-GM_1 interaction conducted under steady-state equilibrium for the CTb concentration range of 120 nM to 240 nM, $2.6 \times 10^{11}\ M^{-1}$ ($K_d = 4.61 \times 10^{-12}\ M$),[16] suggesting that the SHCS measured binding kinetics are true steady-state equilibrium values. Additionally, similar concentration dependent protein-ligand binding kinetics have been reported in the literature. For example, at low wheat germ agglutinin (WGA)

protein concentrations (20pM to 10 μM) WGA experienced a much higher affinity for its ligand than at higher WGA concentrations (5- 200 μM).[4,42] This is consistent with the results seen here obtained via SHCS where the lowest CTb concentration has the highest binding affinity for GM_1. The good agreement with steady-state literature binding kinetic values and previously reported binding affinity trends demonstrates SHCS can be used to accurately measure multivalent protein-ligand interactions at the surface with negligible mass transport affects.

7.3.2 Binding Kinetics of CTb-GM_1 Using an SHG Adsorption Isotherm

To further examine the CTb – GM_1 complex, a steady-state equilibrium isotherm was collected for the CTb bulk concentration range of 0.22 nM to 13 nM and data are shown in Figure 7.8 (solid circles). Each concentration was allowed to reach steady-state equilibrium before the next concentration was equilibrated with the surface. The data collection took a total of 49 hrs to complete as the lower concentrations took between 12-14 hrs to reach steady-state equilibrium. Nonspecific binding of CTb to a pure DOPC bilayer was also examined and plotted in Figure 7.8 (open circles). It is apparent from the data in Figure 7.8 that there is negligible nonspecific binding observed over the entire CTb concentration range examined, which is consistent with the data determined using SHCS. A study by Shi and coworkers where the binding of CTb to 1 mol % GM_1 doped into a lipid bilayer was examined using fluorescence found the CTb-GM_1 interaction fit best to the Hill-Waud cooperative model.[7] As such, the data in Figure 7.8 (solid circles) were fit to both the Langmuir model (Equation 3.9) and the Hill-Waud model (Equation 7.3). The data in Figure 7.8 were found to statistically fit best to the Hill-Waud model

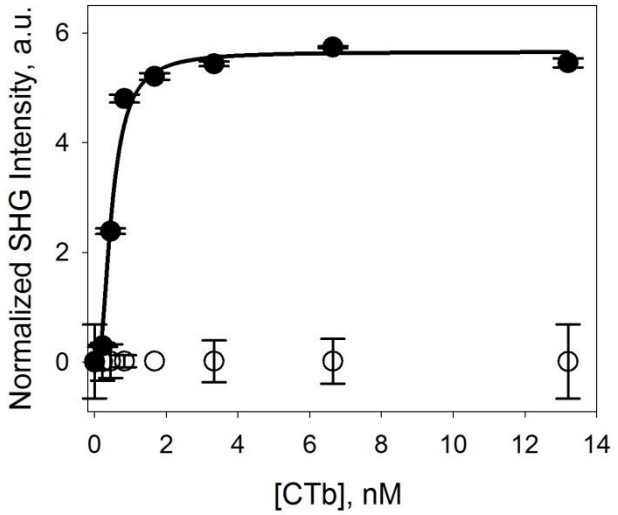

Figure 7.8. SH intensity versus bulk CTb concentration binding to 1 mol% GM_1 doped into a DOPC bilayer recorded at steady-state equilibrium (solid circles) and to a pure DOPC bilayer (open circles). The solid line represents the fit to the Hill-Waud binding model. The error bars represent the standard deviation from two independent experiments.

using an *f*-test analysis. The resulting K_0 was $3.2 \pm 0.3 \times 10^9\ M^{-1}$ with a Hill coefficient of 2.0 ± 0.5. These results indicate that there is a positive cooperative interaction between ligand molecules and that once one ligand is bound there is an increased affinity for the protein to bind to the neighboring ligand molecules. Although both the K_0 and n determined here are statistically the same as those reported by Shi and coworkers, $K_0 = 3.2 \pm 0.7 \times 10^9\ M^{-1}$ ($K_d = 0.31 \pm 0.05 \times 10{-}^9\ M$) and $n = 1.9$,[7] the K_0 is much lower than that obtained using SHCS. This discrepancy between the isotherm data and the SHCS data most likely is due to the influence of mass transport on the binding kinetics obtained from the isotherm data of CTb binding to GM_1. Although CTb was allowed to incubate with the surface for an extended period of time (up to 12 hrs) and the bulk protein solution was replaced every 5 to 10 mins, true steady-state equilibrium is likely to have not been obtained, especially at the lowest CTb concentrations were small changes in signal were harder to distinguish. It is true that continuous flow would reduce mass transport effects even more; however, given the incubation time required at the lower CTb concentrations and the amount of analyte needed, such an experiment would be unreasonable in terms of the time required to perform the analysis and the cost of materials. Furthermore, a similar mass transport investigation has already been performed by Kuziemko et al. at higher CTb concentrations and has shown the binding kinetics are drastically affected by flow rate. In the work presented by Kuziemko and coworkers, which reported the same binding kinetics as SHCS for 240 nM CTb, multiple flow rates were investigated and an optimal flow rate was chosen such that the binding kinetics of CTb to GM_1 showed no limitation on mass transport.[16] The good agreement between the steady-state equilibrium results obtained by Kuziemko and coworkers and those obtained

using SHCS, suggests that the SHCS data are void of mass transport effects and provide more precise results for the binding of CTb to GM_1 as compared to the isotherm study, which is likely mass transport limited. Additionally, as mentioned earlier, SHCS has the ability to determine the binding kinetics without contributions from diffusion even when collection is not done under true steady-state equilibrium conditions as these two events occur at different time scales and will appear as two separate decays in the correlation data.[39,41]

7.3.3 Binding Kinetics of PnA-GM_1 Using SHCS

In addition to the CTb-GM_1 binding study, SHCS was also used to determine the binding kinetics of the multivalent binding protein, PnA, to 5 mol % GM_1 doped into a DOPC lipid bilayer. The data collected for PnA concentrations of 0.43 μM, 3 μM, and 12 μM binding to a 5 mol % GM_1 doped DOPC bilayer are shown in the insets of Figure 7.9A, 7.10A and 7.11A. The normalized correlation data obtained from the average of 20 data sets are shown for each of the 3 PnA concentrations in Figures 7.9A, 7.10A and 7.11A. As before, the first point of the correlation data and high frequency contributions (15 times the Nyquist limit) have been removed as they contain the contributions from the photon shot noise of the detection system. Autocorrelation was also performed on the average of 20 data sets for the PnA concentrations 0.43 μM, 3 μM, and 12 μM binding to a pure DOPC bilayer without the ligand GM_1, shown in the insets of Figures 7.9B, 7.10B and 7.11B. The normalized correlation data of the nonspecific binding of PnA to DOPC are shown in Figures 7.9B, 7.10B and 7.11B. The nonspecific autocorrelation data were normalized to the corresponding specific autocorrelation data to allow comparison of the

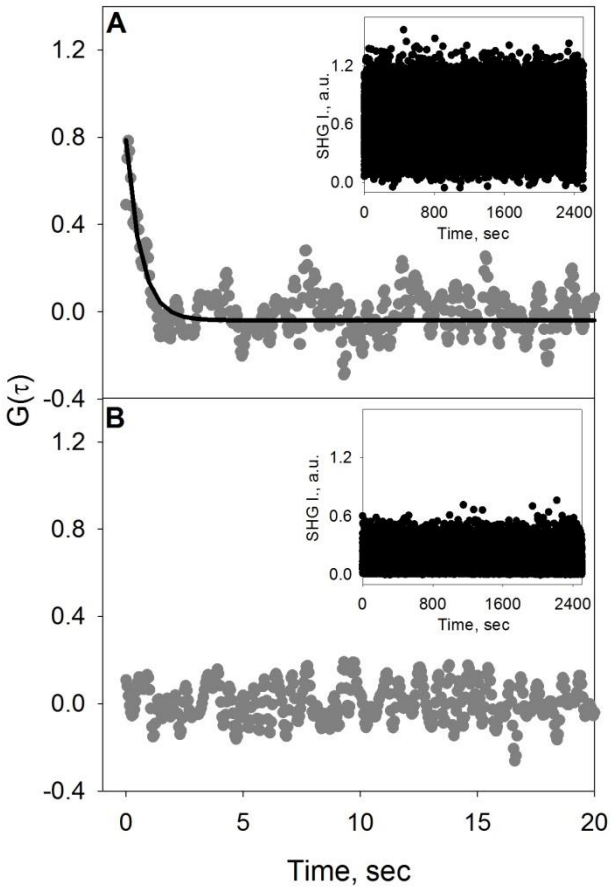

Figure 7.9. Autocorrelation data for 0.43 μM PnA binding to (A) 5 mol % GM_1 doped into a DOPC bilayer and (B) a pure DOPC bilayer. Solid black line is the fit to Equation 5.17. The nonspecific PnA correlation function (B) was normalized to the specific binding correlation function (A).

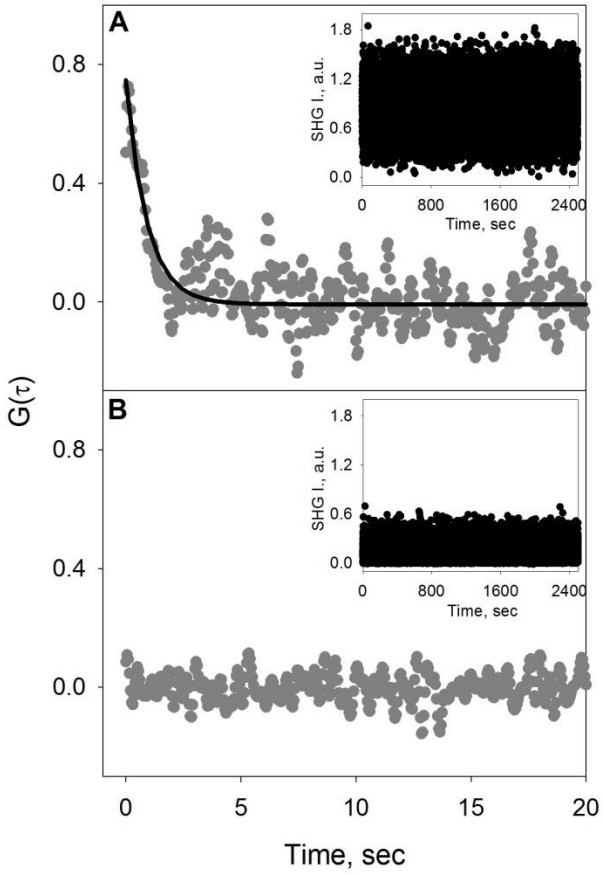

Figure 7.10. Autocorrelation data for 3 μM PnA binding to (A) 5 mol % GM_1 doped into a DOPC bilayer and (B) a pure DOPC bilayer. Solid black line is the fit to Equation 5.17. The nonspecific PnA correlation function (B) was normalized to the specific binding correlation function (A).

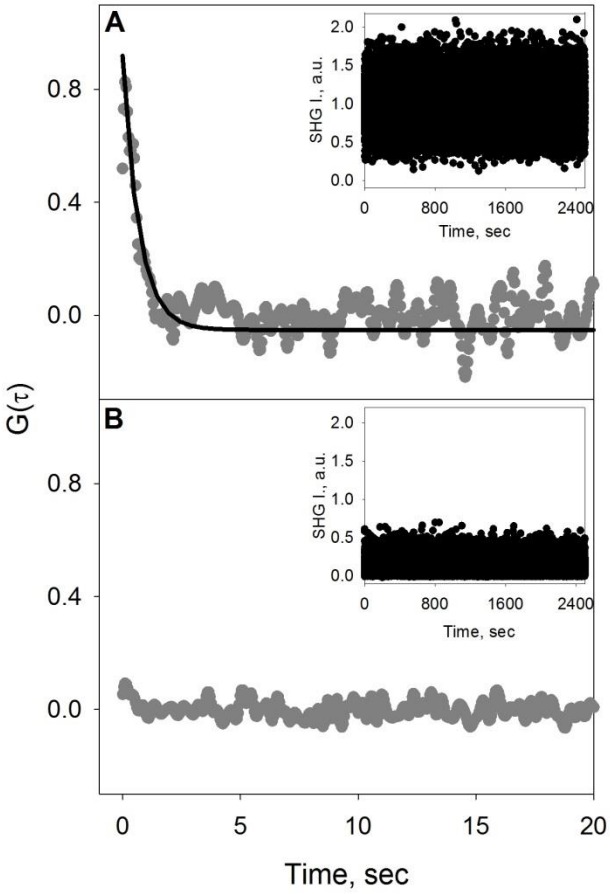

Figure 7.11. Autocorrelation data for 12 μM PnA binding to (A) 5 mol % GM_1 doped into a DOPC bilayer and (B) a pure DOPC bilayer. Solid black line is the fit to Equation 5.17. The nonspecific PnA correlation function (B) was normalized to the specific binding correlation function (A).

relative magnitudes of the specific and nonspecific correlation functions. Here again, noting that before normalization the noise of all three nonspecific correlation data were relatively the same and oscillated about the same mean SH intensity. There is no correlation seen in Figures 7.9B, 7.10B and 7.11B, suggesting that there is negligible nonspecific binding of PnA to a pure DOPC bilayer for all PnA concentrations studied. As such, the correlated events seen in the data shown in Figures 7.9A, 7.10A and 7.11A are solely from the specific binding of PnA to 5 mol % GM_1.

The normalized autocorrelation data of the specific binding of PnA to 5 mol% GM_1 doped into a DOPC bilayer for the 3 bulk PnA concentrations were fit to Equation 5.17 with the fitting parameters k_{on}, k_{off} and N_s and the results from the nonlinear least-squares regression are shown in Table 7.2. The measured adsorption rates decreased from $3.7 \pm 0.3 \times 10^6\ M^{-1}s^{-1}$ to $3.9 \pm 0.3 \times 10^5\ M^{-1}s^{-1}$ to $1.1 \pm 0.1 \times 10^5\ M^{-1}s^{-1}$ as the bulk PnA concentration decreased from 0.43 μM to 3 μM to 12 μM. The desorption rates $1.0 \pm 0.2 \times 10^{-3}\ s^{-1}$, $2.2 \pm 0.2 \times 10^{-3}\ s^{-1}$, $2.7 \pm 0.2 \times 10^{-3}\ s^{-1}$ for the bulk PnA concentrations 0.43 μM, 3 μM, and 12 μM, respectively, did not change (within experimental error) with increasing PnA concentration. The concentration dependent binding kinetics seen for PnA-GM_1 are similar to that seen for the CTb-GM_1 study discussed earlier and can similarly be explained in terms of high affinity binders at low concentrations as well as electrostatics. PnA (pI ~ 6)[43] has a slightly negative charge at neutral pH and GM_1 contains a negatively charged terminal sialic acid that could repel the PnA molecules. The electrostatic repulsion between the negatively charged PnA molecules and the negatively charged immobilized GM_1 could cause a reduction of the rate of additional protein molecules binding to the surface and lead to the slower adsorption rate observed

Table 7.2. Measured binding kinetics for PnA binding to a GM_1 doped DOPC bilayer using SHCS including the adsorption rate (k_{on}), desorption rate (k_{off}), and equilibrium binding affinity (K_0).

	[PnA] (μM)	k_{on} *(×* 10^5 $M^{-1}s^{-1}$*)*	k_{off} *(×* 10^{-3} s^{-1}*)*	K_0 *(×* 10^8 M^{-1}*)*
SHCS	0.43	37 ± 3	1.0 ± 0.2	37 ± 8
	3.0	3.9 ± 0.3	2.2 ± 0.2	1.7 ± 0.2
	12.2	1.1 ± 0.1	2.7 ± 0.2	0.41 ± 0.05

at higher PnA concentrations.

In addition to the adsorption and desorption rates, the equilibrium binding affinity, K_0, was calculated for each PnA concentration using Equation 5.12 and the results are shown in Table 7.2. The highest K_0, $3.7 \pm 0.8 \times 10^9\ M^{-1}$, was observed for the 0.43 μM PnA-GM1 interaction, followed by $1.7 \pm 0.2 \times 10^8\ M^{-1}$ for 3 μM PnA and $4.1 \pm 0.5 \times 10^7\ M^{-1}$ for 12 μM PnA. This decrease in K_0 with increasing PnA concentration suggests that the electrostatic repulsion between the negatively charged PnA molecules and the negatively charged immobilized GM_1 reduce the binding affinity at higher PnA concentrations. The K_0 values obtained using SHCS are much higher than those typically reported for PnA binding to GM_1.[6,13] In a study that monitored the binding of PnA to a 4.8 mol% GM_1 doped lipid bilayer on the surface of a gold electrode using QCM, the K_0 ($8.3 \times 10^5\ M^{-1}$) was found to be 3–4 orders of magnitude smaller than that found using SHCS.[13] However, in the QCM study the K_0 was determined using a typical binding isotherm for the bulk PnA concentration range of ~0.25 μM to 6 μM.[13] For a more direct comparison a similar binding isotherm was collected here for PnA binding to a 5 mol % GM_1 doped DOPC lipid bilayer using SH spectroscopy.

7.3.4 Binding Kinetics of PnA-GM_1 Using an SHG Adsorption Isotherm

The SH signal was monitored over time and increased as the bulk PnA concentration increased from 0.22 μM to 12.2 μM, shown in Figure 7.12 (triangles). To keep the experimental parameters the same as those in the QCM study multiple injections were not made and each protein concentration was allowed to only incubate for ~30 min. Due to the slightly negative charge of PnA at pH 7.4 (pI ~ 6)[43] the data in Figure 7.12

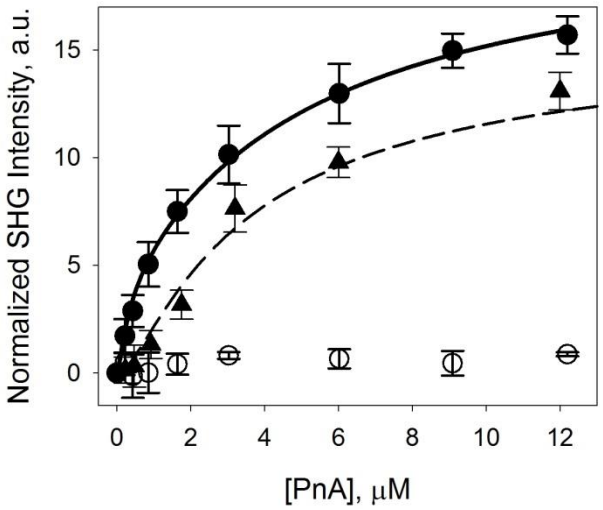

Figure 7.12. SH intensity versus bulk PnA concentration binding to 5 mol% GM_1 doped into a DOPC bilayer recorded at steady-state equilibrium (solid circles), at non steady-state equilibrium (triangles), and to a pure DOPC bilayer (open circles). Lines represent the fits to the Frumkin binding model (solid) and Langmuir model (dashed). The error bars represent the standard deviation from three independent experiments.

were fit to the Frumkin model, which accounts for any electrostatic interactions between charged protein molecules, as well as the typical Langmuir model (Equation 3.9). An *f*-test was performed to determine which model statistically fit best to the data with a confidence level of 95%. The Frumkin model has been previously expressed in terms of SH intensity and can be written as,[44]

$$I_{SHG} \propto \left(\frac{\sqrt{I_{SHG}^{max}} K_a[P] exp^{(2g\sqrt{I_{SHG}}/RT)}}{1 + K_a[P] exp^{(2g\sqrt{I_{SHG}}/RT)}} \right)^2 . \quad (7.4)$$

The above equation is similar to the Langmuir model with the additional electrostatic term *g*. The *g* coefficient describes the electrostatic interactions between the charged protein molecules on the surface, where $g < 0$ indicates a repulsive electrostatic interaction between protein molecules and $g > 0$ indicates an attractive electrostatic protein-protein interaction.[44] The nonequilibrium, single solution isotherm in Figure 7.12 (triangles) was found to statistically fit best to the Langmuir model (Equation 3.9). The K_0 determined from the nonlinear least squares fit to Equation 3.9 for PnA binding to a 5 mol % GM_1 doped DOPC bilayer was found to be $5.4 \pm 0.7 \times 10^5\ M^{-1}$. This K_0 is similar to that reported by Jansoff and coworkers for the QCM study,[13] but still 2 to 3 orders of magnitude lower than that measured by SHCS.

Since the previous isotherm is most likely mass transport limited, an isotherm collected under quasi-continuous flow for PnA binding to a 5 mol % doped DOPC bilayer was also determined. To account for the depletion of bulk protein concentration as PnA molecules bound to the surface, multiple injections were made every 5-10 mins at each PnA concentration measured ranging from 0.22 μM to 12.2 μM until a steady-state

equilibrium had presumably been reached, data shown in Figure 7.12 (solid circles). A discrepancy between the isotherm collected with a single solution of PnA and that collected using a quasi-continuous flow is particularly apparent at lower PnA concentrations (Figure 7.12). This suggests that the single solution isotherm data were indeed not collected under steady-state conditions, and therefore gave an underestimated K_0 value. The data in Figure 7.12 (solid circles) were fit to both Equation 3.9 (Langmuir model) and Equation 7.4 (Frumkin model) and found to statistically fit best to the Frumkin model. The determined K_0 from the nonlinear least-squares fit to Equation 7.4 was $3.0 \pm 0.2 \times 10^6\ M^{-1}$ with a g value of -536 ± 50 J/mol. This K_0 is ~6 times greater than that seen for the isotherm not conducted under steady-state conditions as well as that reported by Jansoff and coworkers.[13] Although this K_0 is still ~ 1 order of magnitude lower than that obtained for the highest PnA concentration (12 μM) using SHCS, the difference in the K_0 values obtained from the quasi-continuous flow isotherm and the single injection isotherm illustrates the tremendous importance of allowing low protein concentrations sufficient incubation time with the surface in order to reach steady-state equilibrium, which in the case of PnA took up to 2 hrs at low concentrations.

To further probe the effects of mass transport on the predicted K_0, separate adsorption and desorption experiments were performed for PnA concentrations of 0.43 μM, 3 μM and 12 μM. The SH intensity was monitored over time as each bulk PnA concentration was adsorbed to 5 mol % GM_1 doped into a DOPC bilayer. After a fresh protein solution was injected to replenish the bulk protein concentration, the SHG intensity was collected every 5-10 mins for 2-3 mins until steady-state equilibrium had been reached (data shown in Figure 7.13A). Once steady-state equilibrium had been

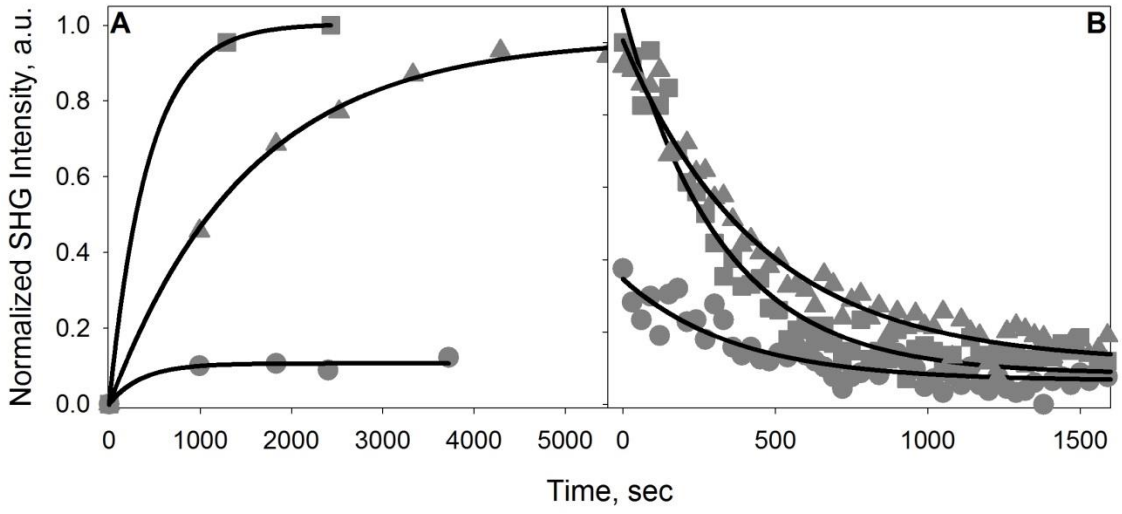

Figure 7.13. SH Intensity vs. time for (A) the adsorption and (B) desorption of PnA under quasi-continuous flow at a bulk protein concentration of 0.43 μM (circles), 3 μM (triangles), and 12 μM (squares). Solid lines are fits to Equation 3.15 (A) and an exponential decay (B).

reached, the PnA was desorbed by flushing a copious amount of buffer over the surface and collecting the SH signal every 15 s (data shown in Figure 7.13B). The adsorption data (Figure 7.13A) were fit to an exponential rise model described in Equation 3.15 while the desorption data (Figure 7.13B) were fit to an exponential decay to obtain k_{off}. The desorption rates for PnA concentrations of 0.43 μM, 3 μM and 12 μM were 2.2 ± 0.7 × 10^{-3} s^{-1}, 2.4 ± 0.1 × 10^{-3} s^{-1}, and 4.1 ± 1.2 × 10^{-3} s^{-1}, respectively. Using these desorption rates and the calculate rate from the fits to data in Figure 7.13A to Equation 3.15, the adsorption rates for PnA concentrations of 0.43 μM, 3 μM and 12 μM were calculated as 1.4 ± 0.5 × 10^{3} $M^{-1}s^{-1}$, 5.8 ± 0.4 × 10^{2} $M^{-1}s^{-1}$, and 1.5 ± 0.4 × 10^{2} $M^{-1}s^{-1}$, respectively. Although the adsorption rates are not identical to those measured using SHCS, all three of the desorption rates are in good agreement with those measured by SHCS. Interestingly, the same inverse relationship between the binding kinetics and PnA concentration is apparent in both the adsorption data and the SHCS data. The discrepancy between the adsorption rates obtained using SHCS and those obtained from monitoring the adsorption over time might be due to experimental design. The data obtained using SHCS are collected after steady-state equilibrium has already been reached. For the adsorption experiment, there is no protein present at time zero and when PnA is first introduced into the flowcell there is not only a "lag time" for the protein molecules to diffuse to the surface,[9] but also depletion of the bulk concentration as PnA binds to GM_1. Although the depletion of the bulk concentration is replenished every 5 mins with a fresh protein solution, this might not be fast enough to exchange the depletion of protein molecules in the interfacial layer near the surface before the protein concentration of the interfacial layer has dropped below the bulk protein concentration.

To validate this hypothesis, the SH intensity from the adsorption of PnA to GM_1 was monitored over time as a continuous flow of protein solution was flowed over the surface at a rate of 3 mL/min (data shown in Figure 7.14). Under continuous flow conditions there is a decrease in the time it takes to reach a steady-state response as compared when multiple injections are made over time. The k_{on} for the continuous flow adsorption were calculated to be $1.4 \pm 0.4 \times 10^4\ M^{-1}s^{-1}$, $1.1 \pm 0.1 \times 10^3\ M^{-1}s^{-1}$, and $8.8 \pm 2.6 \times 10^2\ M^{-1}s^{-1}$ for PnA concentrations 0.43 μM, 3 μM and 12 μM, respectively. The fact that k_{on} increases for each PnA concentration when the fresh protein solution is continuously flowed over the surface as compared to adding fresh protein solution incrementally over time is evidence that mass transport is influencing the measured k_{on}, leading to a lower predicted adsorption rate than what actually exists. Additionally, k_{on} increases by a greater percentage at lower PnA concentrations than at higher PnA concentrations when switching from multiple injections to continuous flow collection, further suggesting the adsorption of PnA is mass transport limited. For the SHCS data, this mass transport effect on the binding kinetics is not present and as a result the calculated binding kinetics are drastically different from those calculated using binding isotherms where there are mass transport effects. The results of PnA-GM_1 adsorption conducted under a continuous flow of varying flow rates suggest that the quasi-continuous flow isotherm in Figure 7.12 is still mass transport limited. As such, the predicted K_0 from the quasi-continuous flow isotherm is still lower than that determined by SHCS.

Despite the mass transport effects on the binding isotherms, one characteristic apparent from the quasi-continuous flow isotherm that was not seen in the single

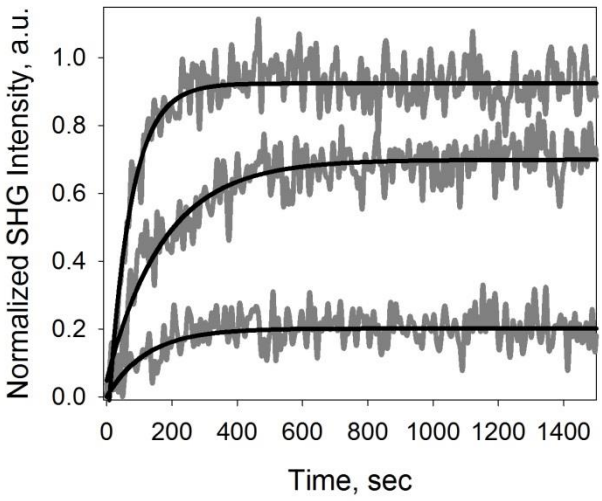

Figure 7.14. SH Intensity vs. time for the continuous flow adsorption of PnA to GM_1 for 0.43 μM (bottom), 3 μM (middle), and 12 μM (top) PnA bulk concentration. Solid lines are fits to Equation 3.15.

injection isotherm is that there is repulsion between the PnA molecules resulting in a better fit to the Frumkin model and a negative *g* value. The large negative *g* value suggests that there is a large electrostatic repulsion between the charged protein molecules at the surface, which could hinder binding and slow the adsorption rate as the concentration of PnA increases. Although this electrostatic repulsion between charged PnA molecules is reasonable considering the negative pI ~ 6 of PnA,[43] the electrostatic potential map was also calculated to further quantify the charge distribution of the surface residues of PnA and is shown in Figure 7.15. Essentially, the entire solution exposed surface of PnA is negative which explains the rather high electrostatic repulsive constant calculated using the Frumkin model. Additionally, the highly negative PnA surface would be repelled by the negative sialic acid terminus on GM_1, which explains the decreasing adsorption rate with increasing PnA concentration as measured by SHCS.

7.3.5 Binding Kinetics of PnA-GM_1 at an Above Saturation PnA Concentration Using SHCS

The importance of incubation time and mass transport limited kinetics was also demonstrated in a lectin iodination study by Emerson and Juliano where PnA binding to the N-acetyl galactose receptors on Chinese hamster ovarian (CHO) cells for the PnA concentration range of 10 to 60 μM was allowed to incubate with the surface for twice the amount of time as the QCM study (at least 1 hr) and a K_0 of $4.5 \pm 1 \times 10^6\ M^{-1}$ was found.[4] Although the obtained K_0 is similar to that obtained in the quasi-continuous flow isotherm, it is important to note that the iodination study was conducted for a much higher PnA concentration range and could contribute to the obtained binding kinetics.

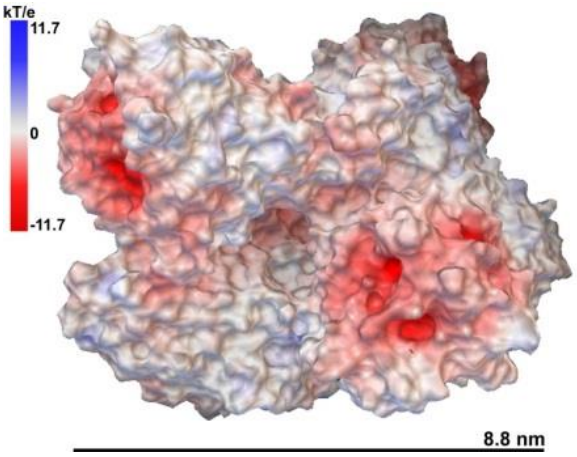

Figure 7.15. The electrostatic potential map of PnA (PDB: 2PEL) calculated in Python Molecular Viewer from Scripps MGL tools assuming a 150 mM salt concentration[37] where red represents negative charges.

In the same iodination study by Emerson and Juliano the interaction of wheat germ agglutinin (WGA) to CHO cell receptors for the bulk WGA concentration range of 5 – 200 μM was investigated and found to have a binding affinity of $1.6 \times 10^6\ M^{-1}$;[4] however, a similar iodination study by Stanley and Carver reported a K_0 of ~ 2 orders of magnitude greater for the bulk WGA concentration range of 20 pM to 10 μM.[42] These 2 iodination studies suggest that the binding affinities of lectins are highly dependent on protein concentration, which is also consistent with the data from the SHCS studies presented here. To compare Emerson and Juliano's results obtained under steady-state equilibrium, SHCS was performed on 60 μM PnA (the highest concentration used by Emerson and Juliano) binding to a 5 mol % GM_1 doped DOPC bilayer. The SHCS data was filtered 15x the Nyquist limit to reduce the proportional noise and were fit to Equation 5.17 with the fitting parameters k_{on}, k_{off} and N_s (data shown in Figure 7.16). The resulting adsorption and desorption rate are $3.1 \pm 0.3 \times 10^4\ M^{-1}s^{-1}$ and $3.7 \pm 0.5 \times 10^{-3}\ s^{-1}$, respectively, giving a K_0 of $8.4 \pm 1.4 \times 10^6\ M^{-1}$. The K_0 obtained for the SHCS of 60 μM PnA-GM_1 is similar to that obtained by Emerson and Juliano. Since Emerson and Juliano allowed PnA to incubate with the surface longer at a much higher concentration as compared to the QCM study, it is likely that the results have minimal mass transport effects and is most likely why the binding constant of the iodination study is consistent with that obtained using SHCS for 60 μM PnA.

The results from this chapter emphasize the tremendous importance of conducting kinetic measurements under steady-state equilibrium conditions. The agreement between the data for 60 μM PnA binding to GM_1 measured by SHCS and the iodination study conducted under conditions minimizing mass transport effects suggests that SHCS

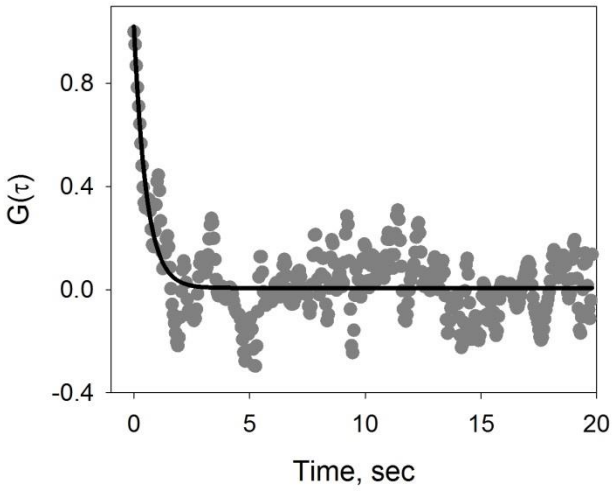

Figure 7.16. Autocorrelation data for 60 μM PnA binding to a 5 mol % GM_1 doped DOPC bilayer with fit to Equation 5.17 indicated by the red line.

measures binding kinetics that are not mass transport limited. The importance of eliminating mass transport was also seen from the comparison of the binding kinetics for CTb binding to GM_1 measured using SHCS and an SPR study where the flow rate was such that data were collected under steady-state conditions. The incubation time was also shown to significantly affect mass transport and the measured binding affinity as seen from the PnA-GM_1 isotherms conducted under different incubation times and flow rates. An inherent advantage of SHCS over the typical binding isotherms used to quantify protein-ligand interactions is that the nature of the SHCS analysis allows the binding kinetics to be determined with negligible mass transport effects as diffusion occurs at a much different time scale, meaning the reported SHCS binding kinetic values are inherently void of mass transport effects. Therefore, the adsorption rate determined using SHCS is not artificially lowered by nonequilibrium conditions and provides an accurate adsorption rate for multivalent protein-ligand interactions at a surface.

7.4 Summary

In this chapter, the binding kinetics of the multivalent protein-ligand interactions between PnA-GM_1 and CTb-GM_1 were investigated using both SHCS and a traditional equilibrium binding isotherm. The adsorption and desorption rates and overall binding affinity for 3 separate protein concentrations were determined using SHCS, while the cooperative binding behavior and electrostatics of the multivalent protein-ligand interactions were investigated using binding isotherms. The results demonstrate the complexity of multivalent protein-ligand interactions and suggest the binding kinetics are dependent on the bulk protein concentration. Due to the extremely high sensitivity of

SHG, a sigmoidal behavior at low PnA concentrations was detectable, suggesting there is an electrostatic repulsion between the charged PnA protein molecules. Both the PnA-GM_1 and CTb-GM_1 studies demonstrate the importance of eliminating the influence of mass transport on the binding kinetics. More importantly, this chapter illustrates that by combining SHCS with conventional isotherm studies, additional information of the complex interactions between multivalent proteins and ligands can be obtained. While a binding isotherm can provide useful information on the electrostatics and cooperative binding behavior of the multivalent protein-ligand interaction, it overlooks the concentration dependence of the binding kinetics. On the other hand, using SHCS to examine the binding kinetics of multivalent protein-ligand interactions at a surface provides extremely valuable information on the binding kinetics as a function of protein concentration. Furthermore, SHCS requires much less time and analyte to determine the binding kinetics for a single concentration as compared to isotherm studies. The results of this chapter provides further understanding of the binding kinetics of two important multivalent protein-ligand interactions, which provides greater insight into what parameters should be considered (protein concentration, mass transport, and cooperative interactions) when using such multivalent protein-ligand complexes in biosensors, immunoassays, and other biomedical diagnostics.

7.5 References

(1) Arosio, D.; Vrasidas, I.; Valentini, P.; Liskamp, R. M. J.; Pieters, R. J.; Bernardi, A. *Org. Biomol. Chem.* **2004**, *2*, 2113-2124.

(2) Moran-Mirabal, J. M.; Edel, J. B.; Meyer, G. D.; Throckmorton, D.; Singh, A. K.; Craighead, H. G. *Biophys. J.* **2005**, *89*, 296-305.

(3) Wittenberg, N. J.; Johnson, T. W.; Oh, S.-H. *Anal. Chem.* **2012**, *84*, 8207-8213.

(4) Emerson, D.; Juliano, R. L. *J. Cell. Physiol.* **1982**, *111*, 171-176.

(5) Molin, K.; Fredman, P.; Svennerholm, L. *FEBS Lett.* **1986**, *205*, 51-55.

(6) Liener, I. E.; Sharon, N.; Goldstein, I. J.;*The Lectins: Properties, Functions, and Applications in Biology and Medicine*; Academic Press, Inc, 1986.

(7) Shi, J.; Yang, T.; Kataoka, S.; Zhang, Y.; Diaz, A. J.; Cremer, P. S. *J. Am. Chem. Soc.* **2007**, *129*, 5954-5961.

(8) Schoen, A.; Freire, E. *Biochemistry* **1989**, *28*, 5019-5024.

(9) Duverger, E.; Frison, N.; Roche, A.-C.; Monsigny, M. *Biochimie* **2003**, *85*, 167-179.

(10) Cabral-Lilly, D.; Sosinsky, G. E.; Reed, R. A.; McDermott, M. R.; Shipley, G. G. *Biophys. J.* **1994**, *66*, 935-941.

(11) Irazoqui, F. J.; Jansson, B.; Lopez, P. H. H.; Nores, G. A. *J. Biochem.* **2001**, *130*, 33-37.

(12) Makita, A.; Tsuiki, S.; Fujii, S.; Warren, L.;*Membrane Alterations in Cancer,* Japan Scientific Societies Press, 1983.

(13) Janshoff, A.; Steinem, C.; Sieber, M.; Galla, H.-H. *Eur. Biophys. J.* **1996**, *25*, 105-113.

(14) Ramakrishnan, A.; Sadana, A. *Biosens. Bioelectron.* **2000**, *15*, 651-662.

(15) Miller, C. E.; Majewski, J.; Watkins, E. B.; Kuhl, T. L. *Biophys. J.* **2008**, *95*, 629-640.

(16) Kuziemko, G. M.; Stroh, M.; Stevens, R. C. *Biochemistry* **1996**, *35*, 6375-6384.

(17) Terrettaz, S.; Stora, T.; Duschl, C.; Vogel, H. *Langmuir* **1993**, *9*, 1361-1369.

(18) Fainerman, V. B.; Lucassen-Reynders, E. H.; Miller, R. *Colloids Surf., A* **1998**, *143*, 141-165.

(19) Neurohr, K. J.; Mantsch, H. H.; Young, N. M.; Bundle, D. R. *Biochemistry* **1982**, *21*, 498-503.

(20) Swamy, M. J.; Gupta, D.; Mahanta, S. K.; Surolia, A. *Carbohydr. Res.* **1991**, *213*, 59-67.

(21) Amado, M.; Yan, Q.; Comelli, E. M.; Collins, B. E.; Paulson, J. C. *J. Biol. Chem.* **2004**, *279*, 36689-36697.

(22) Neurohr, K. J.; Young, N. M.; Smith, I. C. P.; Mantsch, H. H. *Biochemistry* **1981**, *20*, 3499-3504.

(23) Bersudsky, M.; Rosenberg, P.; Rudensky, B.; Wirguin, I. *Neuromuscular Disorders* **2000**, *10*, 182-186.

(24) Neurohr, K. J.; Young, N. M.; Mantsch, H. H. *J. Biol. Chem.* **1980**, *255*, 9205-9209.

(25) Sandrin, L.; Coche-Guerente, L.; Bernstein, A.; Basit, H.; Labbe, P.; Dumy, P.; Boturyn, D. *Org. Biomol. Chem.* **2010**, *8*, 1531-1534.

(26) Zhao, X.; Eisenthal, K. B. *J. Chem. Phys.* **1995**, *102*, 5818-5826.

(27) Zhao, X.; Goh, M. C.; Subrahmanyan, S.; Eisenthal, K. B. *J. Phys. Chem.* **1990**, *94*, 3370-3373.

(28) Gassin, P.-M.; Martin-Gassin, G.; Benichou, E.; Brevet, P.-F. *J. Phys. Chem. C* **2014**, *118*, 1135-1141.

(29) Sly, K. L.; Mok, S.-W.; Conboy, J. C. *Anal. Chem.* **2013**, *85*, 8429-8435.

(30) Nguyen, T. T.; Conboy, J. C. *Anal. Chem. (Washington, DC, U. S.)* **2011**, *83*, 5979-5988.

(31) Nguyen, T. T.; Sly, K. L.; Conboy, J. C. *Anal. Chem.* **2012**, *84*, 201-208.

(32) Wayment, J. R.; Harris, J. M. *Anal. Chem.* **2009**, *81*, 336-342.

(33) McCain, K. S.; Harris, J. M. *Anal.Chem.* **2003**, *75*, 3616-3624.

(34) Hansen, R. L.; Harris, J. M. *Anal. Chem.* **1998**, *70*, 2565-2575.

(35) Machan, R.; Jurkiewicz, P.; Olzynska, A.; Olsinova, M.; Cebecauer, M.; Marquette, A.; Bechinger, B.; Hof, M. *Langmuir* **2014**, *30*, 6171-6179.

(36) Kelly, C. V.; Wakefield, D. L.; Holowka, D. A.; Craighead, H. G.; Baird, B. A. *ACS Nano* **2014**, *8*, 7392-7404.

(37) Sanner, M. F. *Python: A Programming Language for Software Integration and Development*; J. Mol. Graphics Mod., 1999; Vol. 17.

(38) Day, C. A.; Kenworthy, A. K. *PLoS One* **2012**, *7*, e34923.

(39) Schwille, P. *Fluorescence Correlation Spectroscopy: Theory and Applications*; Springer, 2001.

(40) Widengren, J.; Rigler, R. *Cell. Mol. Biol. (Paris)* **1998**, *44*, 857-879.

(41) Palmer, A. G., 3rd; Thompson, N. L. *Biophys J* **1987**, *51*, 339-343.

(42) Stanley, P.; Carver, J. P. *Proc. Natl. Acad. Sci. U. S. A.* **1977**, *74*, 5056-5059.

(43) Sakamaki, K.; Sawada, K.; Koshimizu, U.; Nishimune, Y. *Biol. Reprod.* **1989**, *41*, 1097-1102.

(44) Nguyen Trang, T.; Rembert, K.; Conboy John, C. *J Am Chem Soc* **2009**, *131*, 1401-1403.

CHAPTER 8

CONCLUSION

In this dissertation SHG was shown to be a highly sensitive, surface specific, and label-free method capable of elegantly examining the binding dynamics of biomolecular interactions at the surface of PSLBs. First, the properties of counter-propagating SHG were detailed in Chapter 2. The SH output is only produced where the inversion symmetry is broken, such as at a surface, making SHG incredibly surface specific. Additionally, increased signal enhancement was shown to be possible by tuning the SH output wavelength to be on resonance with an electronic transition of the molecule being probed. These two properties, the surface specificity and high sensitivity, give SHG the ability to detect trace amounts of analyte without the use of a label. After establishing the various properties of SHG that make it well-suited for investigating surface biomolecular interactions, namely the surface specificity, high sensitivity, and label-free nature, the binding kinetics and energetics of four biotin bound proteins, avidin, streptavidin, neutrAvidin and anti-biotin antibody, were investigated using SHG in Chapter 3. Analysis demonstrated the presence of protein-protein interactions in avidin and its analogs, streptavidin and neutrAvidin. Streptavidin and neutrAvidin were shown to have the strongest protein-protein interactions possibly due to their neutral pH. The stronger protein-protein interactions seen in streptavidin increased the intrinsic binding affinity by

an order of magnitude and made the streptavidin-biotin interaction most energetically favorable among the three avidin protein molecules. Even more remarkably, the examination of the nonspecific binding of avidin, streptavidin and neutrAvidin to a pure DOPC bilayer indicated that neutrAvidin, a commercially made avidin analog designed to reduce nonspecific binding, had the highest degree of nonspecific adsorption with streptavidin exhibiting the lowest degree of nonspecific adsorption. Interestingly, the binding affinity of anti-biotin antibody to biotin at a surface was shown to be the same order of magnitude as the avidin molecules while exhibiting negligible nonspecific binding to a pure DOPC bilayer. Additionally, in the case of anti-biotin antibody, the surface did not need to be passivated with IgG to reduce the nonspecific binding. The detailed comparison of the binding kinetics and thermodynamics of these commonly used protein-ligand pairs in several bioanalytical applications offers important information to be carefully considered when designing biosensor or immunoassay platforms.

In Chapter 4, the plane wave nature and coherence of SSHGI was characterized using Gaussian beam propagation theory. Through comparison with the incoherent technique of fluorescence imaging, it was demonstrated that the coherent plane wave inherent to SSHGI allows imaging to be performed without the incorporation of a lens system. Although the SHG output beam followed Gaussian beam propagation theory, it did deviate from an ideal plane wave more rapidly than theoretically predicted, by a factor of 2.3. This divergence from theory was consistent for all object sizes examined and therefore indicates it is most likely due to some experimental limitation that remains the same throughout each experiment, such as not having perfect collimation of the incident beams. Despite this deviation from theory, SSHGI was able to resolve images of

objects as small as 196 μm at object-detector distances of 7 cm and objects of 397 μm at object-detector distances as far as 30 cm without using a lens. The emissive incoherent fluorescence imaging technique could not resolve images without a lens even at the closest object-detector distances. These findings indicate the unique ability of coherent plane wave processes, such as SSHGI, to image without a lens system. Eliminating the lens can simplify the detection scheme, raise collection photon efficiency, and increase the area of detection, allowing greater throughput imaging to be conducted. The coherent nature of SHG not only proved to be paramount to lens-less SSHGI, but also extremely beneficial to the implementation of SHCS.

The coherence of SHG, a statistical fluctuation technique, had a significant impact on the development of the SHCS theory and experimental parameters for data collection as shown in Chapter 5. The coherent property of SHCS makes it possible to have a large illumination/detection area with a large number of molecules, which increases the overall SH intensity and heterodyne effect, leading to increased S/N of the correlation data. SHCS was first utilized in the analysis of the binding properties of SBN intercalating into a DOPC bilayer, which was the first application of SHCS for the detection of surface biomolecular interactions. Agreement of results obtained from a traditional SHG binding isotherm and those obtained using SHCS, within the 99% confidence level, confirmed the ability of SHCS to accurately determine surface binding kinetics of biomolecular interactions. SHCS offers the advantage of obtaining both the adsorption and desorption rate for one concentration of SBN, meaning the data collection time was reduced and less analyte was required. These results firmly establish SHCS as a new label-free fluctuation correlation method with high sensitivity and surface specificity, capable of monitoring

surface biomolecular dynamics.

In addition to the simple monovalent interaction of SBN to DOPC, the binding kinetics of CTb and PnA to GM_1 were also examined using SHCS. The binding kinetics of these multivalent protein-ligand pairs were found to exhibit a dependence on the concentration of protein. The adsorption rates of both CTb-GM_1 and PnA-GM_1 decreased with increasing protein concentration while the desorption rates remained relatively the same. Ultimately, this led to an increase in binding affinity as the protein concentration was decreased, suggesting that at low protein concentrations there may exist a population of high affinity binders. The concentration dependent kinetics were not apparent in typical binding isotherms as they average over multiple concentrations and neglect the evolving binding kinetics as protein concentration is changed. Furthermore, SHCS was shown to be less sensitive to mass transport effects as these dynamics appear at different time constants as compared to the time constants of the surface binding dynamics studied here. On the other hand, the binding kinetics determined using typical binding isotherms were extremely sensitive to mass transport effects and could cause the measured binding affinity to vary by several orders of magnitude if the binding kinetics were not measured at steady-state equilibrium. It took several hrs (12-14 hrs for CTb-GM_1) to reach near steady-state equilibrium at low protein concentrations and as such SHCS was tremendously advantageous as it did not require true steady-state equilibrium to be reached and could be accomplished in a much shorter time frame. In addition to the valuable insight obtained regarding the complexity of these multivalent protein-ligand interactions using SHCS, this study further established the potential applicability of SHCS as a label-free detection method for the study of more complex surface

biomolecular interactions.

As a whole, this dissertation exhibits the remarkable sensitivity of SHG. Table 8.1 lists the limits of detection reached for the biomolecules examined throughout this dissertation. It is apparent that by simply using resonant enhancement, SHG has the ability to detect down to fg/cm^2. Additionally, combining SHG with correlation spectroscopy allowed surface biomolecular binding kinetics to be determined with great efficiency and less analyte. These properties make SHG and SHCS valuable label-free techniques capable of examining more intricate properties of surface biomolecular interactions with increased sensitivity and proficiency.

Table 8.1. Limit of detection of biomolecules investigated using SHG.

	SHG	
Molecule	femtomoles/cm^2	pg/cm^2 (*Unless otherwise noted)
SBN	0.040 ± 0.001	*0.114 ± 0.004 fg/cm^2
Streptavidin	84 ± 17	4413 ± 883
Cholera Toxin B	0.7 ± 0.1	44.6 ± 6.6
Neutravidin	133 ± 35	7971 ± 2072
Avidin	80.1 ± 0.3	5280 ± 17
Peanut Agglutinin	40.3 ± 3.7	4433 ± 407
Anti-biotin	17 ± 0.9	2384 ± 119